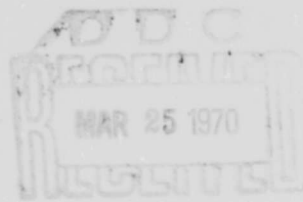


SAM-TR-70-6

AD 702421

SCINTISCANNING SYSTEM FOR STUDY OF  
REGIONAL DISTRIBUTION OF  
BLOOD FLOW

EARL H. WOOD, M.D., Ph. D., et al.



Reproduced by the  
CLEARINGHOUSE  
for Federal Scientific & Technical  
Information Springfield Va. 22151

USAF School of Aerospace Medicine  
Aerospace Medical Division (AFSC)  
Brooks Air Force Base, Texas

February 1970

This document has been approved for public release and sale;  
its distribution is unlimited.

204

UNIT SECTION <input checked="" type="checkbox"/>	
DIFF SECTION <input type="checkbox"/>	
DISCONTINUED <input type="checkbox"/>	
INFORMATIONAL AVAILABILITY INDEX	
DISC.	

Qualified requesters may obtain copies of this report from DDC. Orders will be expedited if placed through the librarian or other person designated to request documents from DDC.

When U. S. Government drawings, specifications, or other data are used for any purpose other than a definitely related Government procurement operation, the Government thereby incurs no responsibility nor any obligation whatsoever; and the fact that the Government may have formulated, furnished, or in any way supplied the said drawings, specifications, or other data is not to be regarded by implication or otherwise, as in any manner licensing the holder or any other person or corporation, or conveying any rights or permission to manufacture, use, or sell any patented invention that may in any way be related thereto.

**SCINTISCANNING SYSTEM FOR STUDY OF REGIONAL DISTRIBUTION  
OF BLOOD FLOW**

**EARL H. WOOD, M.D., Ph. D.  
CRAIG M. COULAM, Ph. D.  
WILLIAM DUNNETTE  
JAMES F. GREENLEAF, M.S., E.E.  
DAVID NATHAN, M.B., B. Ch.  
ERIK L. RITMAN, M.B., B. Sc.  
DONALD J. SASS, M.D.**

## FOREWORD

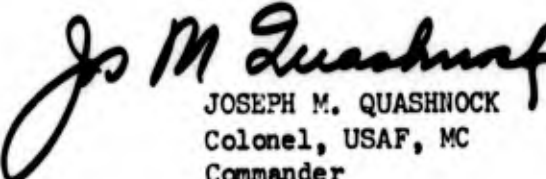
The studies on which this report is based were accomplished in the cardiovascular and human centrifuge laboratories of the Mayo Foundation, Mayo Clinic, Rochester, Minn., under the direction of Dr. Earl H. Wood. The work was performed between January 1968 and September 1969 under Air Force contract No. F41609-68-C-0022 and task No. 793003. The paper was received for publication on 19 November 1969.

Dr. H. L. Stone, Physiological Dynamics Function, Biodynamics Branch, was the contract monitor.

The animals involved in this study were maintained in accordance with the "Guide for Laboratory Animal Facilities and Care" as published by the National Academy of Sciences--National Research Council.

This study was made possible by the unstinting cooperation of many of our technical and professional colleagues in the Mayo Foundation. Miss Lucille Cronin, Ralph Sturm, Julius Zarins, Don Hegland, Don Erdman, Willis Van Norman, Mrs. Caroline Kath, and Mrs. Jean Frank deserve particular mention. The authors also thank Dr. Alan Orvis for his comments and suggestions.

This report has been reviewed and is approved.

  
JOSEPH M. QUASHNOCK  
Colonel, USAF, MC  
Commander

## ABSTRACT

The effect of changes in the direction and magnitude of the gravitational inertial force environment on the regional distribution of impacted  $35\mu$ -diameter microspheres has been measured in the lungs of six anesthetized chimpanzees. These distributions were determined by two computer-controlled scintiscans at 780 sites covering the dorsal and ventral surfaces of the thorax at 1 G subsequent to four injections of differentially isotope-tagged microspheres into the right ventricular outflow tract while at 1 and  $\pm 5.8$  Gy. Pulse-height analysis at each site allowed separation of count values for the isotopes and, after correction for collimator distortion, these values were assumed to be proportional to the respective blood flows which were present below each site at the respective time of injections. Computer-generated 3-dimensional and contour map displays of the scintiscan and related physiologic data indicate that pulmonary blood flow tended to redistribute toward the midthoracic region during acceleration exposures concomitantly with large decreases in arterial oxygen saturation presumably from pulmonary shunting via the dependent regions of the lung. The decrease in blood flow to the superior regions of the lung coupled with the finding of no change or decreases in flow to the dependent regions of the lung suggests that selective increases in resistance to blood flow to the dependent, presumably anoxic, region of the lung occurred which were responsible for the reduction in level of physiologic shunt frequently found in these animals toward the end of the exposure to 5.8 Gy.

## CONTENTS

	Page
<b>SECTION I: COMPUTER -CONTROLLED SCINTISCANNING SYSTEM AND ASSOCIATED COMPUTER PROCESSING TECHNIQUES</b>	
ABSTRACT	1
I. INTRODUCTION	2
II. METHODS AND RESULTS	3
Digital computer - controlled data acquisition and storage	3
Scintigraphic processing and display routines by digital computer	8
A method for converting pulmonary scintiscan data into fractional blood-flow values	14
Superpositioning of anatomic boundaries onto scintigraphic data	16
Radioactive microspheres in pulmonary scintiscanning	18
III. DISCUSSION	21
Digital computer - controlled data acquisition and storage	21
Scintigraphic processing and display routines by digital computer	25
A method for converting pulmonary scintiscan data into fractional blood-flow values	27
Superpositioning of anatomic boundaries onto scintigraphic data	28
Radioactive microspheres in pulmonary scintiscanning	30
REFERENCES	32
FIGURES AND LEGENDS	36

	Page
<b><u>SECTION II: SMOOTHING TECHNIQUES APPLICABLE TO SCINTISCAN DATA</u></b>	
ABSTRACT	53
I. INTRODUCTION	54
II. METHODS	54
III. RESULTS	63
IV. DISCUSSION	65
REFERENCES	69
FIGURES AND LEGENDS	71
<b><u>SECTION III: COMPUTER-GENERATED THREE-DIMENSIONAL OSCILLOSCOPIC IMAGES</u></b>	
ABSTRACT	77
FIGURES AND LEGENDS	79
<b><u>SECTION IV: APPLICATION OF TECHNIQUES TO THE STUDY OF EFFECTS OF <math>\pm G_y</math> ACCELERATION ON PULMONARY BLOOD FLOW IN CHIMPANZEES</u></b>	
ABSTRACT	89
I. INTRODUCTION	91
II. METHODS	94
Initial preparations	94
Blood-flow measurement techniques	98
Other measurements	103
Procedure	107

	Page
III. RESULTS	116
Regional distribution of pulmonary blood flow	116
Effect of body position during scanning procedure on distribution of pulmonary microsphere emboli in the thorax	119
First lateral body position studied	122
Second lateral body position studied	124
Comparison of scintiscan data obtained from the intact thorax in vivo and from scintiscans of the excised lungs of the same animal	126
Spatial distribution of microspheres (blood flow) per unit of lung volume	128
Changes in oxygen saturation of arterial and mixed venous blood	129
Intrathoracic pressure measurements	134
Pleural pressures	137
Aortic and pulmonary artery pressures	138
Left atrial pressures	139
Esophageal pressures	141
Roentgenographic results	141
IV. DISCUSSION	143
Regional distribution of pulmonary blood flow	143
Blood oxygen saturation	155
Pleural pressure relationships	156
APPENDIX	157



	<b>Page</b>
<b>REFERENCES</b>	<b>159</b>
<b>FIGURES AND LEGENDS</b>	<b>164</b>

**I. COMPUTER -CONTROLLED SCINTISCANNING SYSTEM AND  
ASSOCIATED COMPUTER PROCESSING TECHNIQUES**

**BLANK PAGE**

## ABSTRACT

Two methods whereby a digital computer may be used to regulate a scintiscanning process are discussed from the viewpoint of computer input/output software. The computer's function, in this case, is to govern the data acquisition and storage, and to display the results to the investigator in a meaningful manner, both during and subsequent to the scanning process. Several methods (such as three-dimensional maps, contour plots, and wall-reflection maps) have been developed by means of which the computer can graphically display the data on-line for real-time monitoring purposes during the scanning procedure and subsequently for detailed analysis of the data obtained. In addition, a computer-governed method for converting scintiscan data recorded over the dorsal or ventral surfaces of the thorax into fractions of pulmonary blood flow traversing the right and left lungs is presented, along with a technique for transferring anatomic reference points from thoracic roentgenograms onto scintigraphic contour maps.

Thoracic scintiscans have been carried out following injections of isotope-tagged microspheres ( $35 \pm 5\mu$  in diameter) into the right ventricle of dogs and chimpanzees for studying the effect of gravitational-inertial force environment on regional distribution of pulmonary blood flow. Comparison of data obtained from scintiscans of the intact thorax, using the techniques described in this report, with analogous data obtained by scintillation measurements of samples from the same lungs after their removal from the thorax indicates that these two methodologies yield closely similar results.

PREVIOUS PAGE BLANK

## I. INTRODUCTION

The use of digital computers in the analysis and display of scintiscan data has greatly facilitated means whereby scintigraphic data may be made qualitatively, and sometimes quantitatively, more acceptable for research and diagnostic purposes (1-20). Much of the reported work which deals with computer-processed scintiscan data can be grouped into three categories: (1) that dealing with the mathematical manipulation of scintiscan matrices, such as smoothing routines (2-6), collimator modulation transfer removal methods (6-8), and contrast-enhancement techniques (6,9-11); (2) that concerned with the display of scintiscan matrices, such as contour maps (6,12,13), three-dimensional plots (14-16), numerical listings (13,17), and probability groupings (6,16,18); and (3) that concerned with methods for quantitating scintiscan data such as perfused or nonperfused organ and tumor boundaries (18,19), the quantity of blood flow perfusing an organ (20-24), and the depth of an organ or a tumor in tissue (21). Effectively, any type of scintiscanning system whose data can be transported to and processed by one or more computer-applicable methods is potentially capable of being used as a partially, if not completely, automated research or clinical tool. It is the intent of this paper to (A) describe a scintiscan system whose sampling procedure and data-storage process are completely governed by means of a time-shared, on-line digital computer; (B) present some computer-oriented methods for processing and displaying scintigraphic data; (C) describe one potential method by which scintiscan data may be quantitated, using a computer; (D) present a technique whereby anatomic dimensions determined from roentgenograms may be transferred onto scinti-

graphic displays, independent of both x-ray and scintiscan matrix amplification; and (E) discuss some technical problems encountered in the use of radioactive microspheres in external scintiscanning of the lungs of experimental animals. In addition, a correlative study relating data obtained via external scanning of the thorax of intact dogs to the actual distribution of isotope found in the excised lungs of the same dogs, where the isotope has been detected via scintillation well counts of multiple equal-volume sections of the lung parenchyma, is presented.

## II. METHODS AND RESULTS

Digital Computer-Controlled Data Acquisition and Storage. A Control Data Corporation (CDC 3200) computer system has been programmed to control the position of the collimator-detection head assembly of a specially modified Picker Magna V scintiscanner. Two modes of computer-scintiscanner interaction have been investigated: Figure 1 presents a block diagram of what is termed "mode 1 configuration." The computer's control over the scintiscanner is designed to be as general as possible. This requires that several items of information be manually entered, in alphanumeric form, into the computer's regulatory program prior to the scintiscan procedure. The entry of these data into the computer is accomplished by means of the alphanumeric keyboard of a peripheral computer station juxtaposed to the scintiscanner assembly and located remotely (up to 500 feet) from the central computer facility. The preliminary data required prior to beginning the scan procedure consist of: (1) the respective x,y coordinates on the rectilinear scanning plane at which the operator wishes to start and end the scan; (2) the number of points at which samples are taken in

the x and the y directions on this plane; and (3) the file number under which the scintiscan data obtained at each of these points will be stored on digital magnetic tape. The mode 2 method of operation requires, in addition, that the operator specify the duration of the sampling time he wishes at each sampling point on the scanning plane. After the computer has received this information, it initiates the scanning procedure by ordering the scintiscanner, via digital-to-analog (D/A) lines, to move to the initial x,y sampling address. The scanner assembly responds by positioning the collimator-detection head at that point on the scanning plane by comparing the feedback voltages from potentiometers mechanically coupled to the x and y drive mechanisms of the scanner with the voltage levels generated on the x and y D/A command lines from the computer. When coincidence is achieved between the x and y command voltages and the respective feedback voltages from the scanner positioning assembly, the computer is enabled to initiate a start-sampling command to the radiation-detection circuitry over a third D/A line. This initiate pulse may follow immediately after the x,y address has been achieved or may follow after the occurrence of some physiologic event, such as the QRS complex in heart scanning or the detection of end-expiration in pulmonary scanning. Once the scanner head assembly has reached the designated x,y location and the initiate pulse has been received by the scintiscanner, the isotope-counting process is activated for a previously specified period, the sampling time. For the mode 1 configuration, the sampling time at each sampling point on the x-y matrix is specified by dialing the desired count interval into a

digital switch located on the control panel of a four-channel ratemeter. Pulse-height analyzers are used to permit the sampling and counting of up to four different isotope energies simultaneously. Upon termination of the count process, the four count values are transferred to four holding registers and a data-ready pulse sent to the computer. The computer responds by sampling the four analog-to-digital (A/D) lines which are connected to the data-holding registers of the ratemeter. The computer program has an option at this stage in the sequence to initiate one or more sampling periods at that particular x,y sampling point, depending on the magnitude of the accumulated count values obtained during the initial or successive sampling periods at this location on the sampling plane. The x,y coordinates of the next sampling point are then calculated by the computer and the address of this new location is sent to the scintiscanner. If the computer has taken the option to control the number of sampling periods at each sample point in the scan plane, then the count values from each channel must be corrected for any multiple isotope energy spillover falling into adjacent channels by solving a set of four equations in four unknowns stored in the computer (24). If this multiple sample option is not used, the command to move to the next sampling site is sent immediately to the scanner assembly by the computer prior to its correction of count values for spillover effects. This hierarchy of events is used whenever possible so that data computations, data storage, and predata display routines may be carried out by the computer during the periods while the scanner head is moving to successive sampling points. The data are stored



initially in computer memory during the acquisition process and then transferred to disc packs and finally to magnetic tape, as will be discussed in detail below.

The mode 2 operating procedure is similar to mode 1, except that no initiate pulse is required and digital-to-digital (D/D) data transfer is used for entering count values into the computer, thereby eliminating an inherent 1,023 maximal count value limitation imposed by the 10-bit analog-to-digital converter. This mode of operation (fig. 2) proceeds as follows: once the scanner head had reached its specified sampling address, a scanner-ready, interrupt pulse is sent to the computer. The computer, in turn, waits for the appropriate physiologic triggering event, and when it occurs, sends a start-counting command pulse to the scintiscanner. After a specified count interval (entered by the operator from the peripheral computer station prior to beginning the scan) has taken place, the computer sends a stop-counting pulse on a second D/A line. As before, after the count data have been transferred to the holding registers, a data-ready interrupt pulse is sent to the computer, and the processing of the scintiscan data takes place. This mode 2 sequence of data acquisition requires the use of the computer's internal clock for the regulation of the sampling interval. This provides a means by which the computer can vary the duration of the sampling period according to some preconceived logic, such as extending the sampling period until either a specified maximal count value has been attained, or in the case of very low counts, a maximal sampling period has elapsed (see Discussion).

Figure 3 shows a pictorial representation of the equipment presently

being used for mode 1 operation. This peripheral equipment consists of the Picker Magna V scintiscanner, the special arm-positioning and feedback control electronics, the dual-channel ratemeter, and a peripheral computer station and its alphanumeric keyboard. Mode 2 equipment is identical except the dual-channel ratemeters have been replaced by custom-made, four-channel digital ratemeters.

Use of a digital computer for controlling a scintiscanning procedure can be economically justified when a time-sharing computer monitor system is available (25). With such a time-sharing system, the computer is readily accessible to other programs during its run-time operation since only a very small fraction of the available computing time is actually used in the scanner-control and data storage process. In the event, however, that some other active program may stop the computer or possibly alter essential regions of computer memory (especially where memory protect is not available), a subsequent computer "autoload" or memory initialization may be required to make the computer monitor system operational again. In this case, to avoid complete loss of previously stored data and corresponding spatial sampling locations, redundant storage of all acquired scintiscan information is employed. This redundant storage is achieved by transferring the data to the magnetic disc assembly every 20 data values (five sample positions with count values for each of four isotope energy channels per position) along with the last x,y sample address. After 740 count values (185 sample positions) have accumulated on disc, these data are transferred to digital magnetic tape along with their initially entered digital file number for permanent storage. When

a computer autoloader does occur, program reactivation automatically reads the last previously disc-stored x,y sample location, and the scintiscan operation is reactivated from the x,y position immediately following the last entered x,y address. Thus, a nonrecovery stopping of the computer or its memory destruction requires a maximal rescanning effort of five sample positions for the procedure to be operational again.

Scintigraphic Processing and Display Routines by Digital Computer. One very attractive advantage of linking a scintiscanner on-line to a digital computer is that display of the scintiscan data is available during, or immediately after, completion of the scanning procedure. To this end, cathode-ray tube (CRT) display devices (26), printer-generated contour maps (1,5,12,13), and three-dimensional plots (14-16) have been employed. The cathode-ray storage tube, which is a component of the remote computer station, is used to continuously display and update the numerical count values from the four isotope channels as they are being obtained during the scintiscanning procedure, along with the corresponding scanner arm x,y address position (in A/D units). Figure 4 (lower panel) shows a typical picture obtained at one instant during a scintiscan sequence. At the termination of the scan, the computer utilizes its high-speed printer to generate four three-dimensional plots of the data plus the projections of these data onto the x-z and y-z planes. The data are also plotted as isocount values in a contour-map-type format.

Prior to displaying the scintigraphic matrix, however, some data preprocessing must be done. This consists of first digitally smoothing the matrix elements using a statistical, decision-making filtering

scheme, originally described by Brown (2) and subsequently verified and slightly modified by this laboratory to fit our filtering specifications (5). This smoothing scheme has the net effect of attenuating data variations which are attributable to random isotope quantum disintegrations, instrumentation noise, nonuniform biologic isotope dispersion, and so forth, and is a necessary step for the later removal of what we call "collimation distortion." Collimation distortion is the artifact which occurs when the collimated sodium iodide crystal detects isotope energy which is displaced from the focal axis of the collimator. This is demonstrated when a single isotope point source is scintiscanned. A three-dimensional display of the count values obtained from the scanning procedure results in a blunt-tipped cone. This dispersion of counts from a single point is termed the system's modulated transfer function. In many cases, this modulated transfer or point-source response can be adequately approximated by a two-dimensional gaussian curve (27). From this particular viewpoint, the collimation-distortion process is likened mathematically to the passing of an impulse of energy into a two-dimensional filtering system, which in turn produces, as an output, a gaussian distribution of that input energy. Using this "black box" approach, one is able to remove the modulating transfer-function dispersion effects from recorded scintiscan data by the deconvolution iteration method of Iinuma (7), equation 1.

$$F^n(x,y) = F^{n-1}(x,y) + 1 \mathcal{J}(x,y) - F^{n-1}(x,y)*G(x,y) \quad (1)$$

In this equation,  $F(x,y)$  is the undistorted or desired scintiscan matrix;  $n$  refers to the iteration index;  $\mathcal{J}(x,y)$  is the original or recorded scintiscan data matrix; and  $G(x,y)$  is the system's recorded point-source response

or its gaussian approximation. We prefer to use the gaussian approximation to the point-source response when solving equation 1 for  $F(x,y)$ , because the gaussian function contains essentially very little of the random data and background-count variation found on the recorded point-source response. The indices,  $x$  and  $y$ , refer to the scintiscan matrix elements, and the asterisk,  $*$ , denotes two-dimensional convolution. A slight modification of Iinuma's procedures is to make the matrix containing  $G(x,y)$  as small as possible and yet still describe the gaussian point-source response approximation. The description of  $G(x,y)$  can usually be done with less than 10 by 10 matrix elements. The net effect of using the smaller matrix is to process the two-dimensional convolution term,  $F^{n-1}(x,y)*G(x,y)$ , in substantially less time, resulting in many more iterations of equation 1 per minute of computer running time. In general, the matrices,  $F(x,y)$  and  $\phi(x,y)$ , which describe our scintiscan data, usually contain 31 by 26 matrix elements. Use of the smaller-sized matrix enables us to make 20 iterations per minute of computer time (CDC 3200 computer system).

An examination of equation 1 shows that, as the bracketed term approaches zero (that is, as the predicted output curve, based on  $F^{n-1}(x,y)$ , approaches the recorded output curve), the undistorted input  $F^n(x,y)$  is realized. Our experience indicates, however, that the bracketed quantity in equation 1 never reaches zero, but approaches some minimal error value (7). By summing the absolute values for all the  $x,y$  terms in the bracketed expression, both at the start of the iteration process and at the iteration level where this error becomes a minimum, an error reduction of 90% to 99% is found. This means that, with the occurrence of minimal error, the total

influence of all the neighboring elemental values upon their central matrix elements can be less than 10%.  $F^n(x,y)$  is essentially, therefore, the scintiscan matrix one would obtain if the collimator-detection system could detect no isotope energy which emanated from a source whose position was displaced appreciably from a line through the focal axis of the collimator.

The process of displaying these corrected scintiscan data is accomplished as follows: The projection of the data on the x-z plane (fig. 5) is generated from the scintiscan matrix by averaging all of the count values falling on each x coordinate and plotting these average count values against the respective values of the x coordinates. The reflection on the y-z plane is obtained similarly by averaging all count values obtained at each of the y coordinates and plotting these count values against the respective y coordinates.

The three-dimensional distributions are generated by first rearranging the scintiscan data into a rectangular count value (x,y) matrix configuration in computer core, designated as DATA (x,y). This matrix is scaled so that the maximal count value found in DATA equals one-half the maximal number of spaces across a computer printed page (for Control Data Corporation equipment, this is  $120/2 = 60$ ). Next, an offset value equal to y, the number of rows of data available, is added to each count value in row 1 of the matrix, and similarly an offset value of y-1 is added to the elements of row 2. This process continues for the total number of rows of data in the matrix—that is, down to the y<sup>th</sup> row, to which is added the value of 1. The adding of a decreasing offset value to each row

of count values will, when the distribution is printed out, have the effect of tilting the scintigraphic matrix toward the observer (fig. 6). The respective columns of data in the matrix are then slanted to the right or to the left depending upon whether one wishes to observe the data from the right or the left quadrants (as illustrated in the left panels of figure 7) by shifting the data of row 1 to the right or to the left  $y-1$  positions. Row 2 is shifted  $y-2$  positions, row 3,  $y-3$  positions, and so forth, down to the  $y^{\text{th}}$  row where no shift takes place. The areas in computer core in which the shifted data were formerly contained are now zeroed out, leaving a skewed right or skewed left, tilted-forward array. To remove hidden (as opposed to visible or foreground) data points, a mask array is generated which initially contains the data values of the foremost, or  $y^{\text{th}}$ , data row. The values of the  $y-1$  row are compared, columnwise, to the mask values; if they are less than the corresponding mask value, they are set to zero; otherwise, they replace the mask value. This new, or modified, mask is then used to check the  $y-2$  row. The mask update and checking procedure is continued back through row 1, and has the net effect of setting all nonvisible data points to zero while leaving the desired foreground elements with their original matrix values. At this point, a tilted, skewed, and partially erased matrix is ready to be outputted by the high-speed printer. Each row of count values is then assigned a character or alphanumeric symbol to allow for row discrimination and all are printed out, one column at a time, by the printer.

Since each count value in the matrix has been scaled down to an integer less than, or equal to, 60 plus an offset value adjusted in accord with its x and y coordinates, the sum of each specific count and its corresponding offset value can be represented by the number of printer spaces 1 to 120, from left to right of the printed page on which the matrix is plotted. A block diagram of the three-dimensional plot-generating procedure and a scintigraphic matrix orientation guide are given in figure 6.

The other form of printer display used is the conventional contour map (fig. 5, right upper panel). The construction of this type of plot consists of stratifying the scintiscan data values into isocount regions by dividing the difference between the data's maximal and minimal values into a number of strata levels. An alphanumeric or character symbol is then assigned to each of these stratification levels, and any data point which falls into one of those levels is plotted with that particular level's symbol. Our present character symbol hierarchy consists of ,-,A, ,+,B, ,:,C, ,=,D, ,/,E, ,\*F, and ,/; the alphabetic order designates the increasing isotope-concentration strata. Contour-map amplification is obtained by interpolating between x and/or y matrix elements to obtain additional element information. The secret of success in contour-map displays is to use data-point interpolation to obtain the necessary additional matrix elements to compensate for differences in the printed letter or character size and the line spacing. Ignoring the



printed letter's length and width dimensional differences will result in contour maps which are spatially distorted.

A Method for Converting Pulmonary Scintiscan Data into Fractional Blood-Flow Values. The use of the deconvolution scheme yields scintiscan data which can be considered reasonably independent of distortion due to radiation sources displaced from the focal axis of the collimator and consequently allows for advantageous use to be made of the theory that the recorded count values are proportional to the regional blood-flow distribution in organs where the radioactivity is taken up from the tagged blood during the initial transit of this blood through the organ (22-24). In pulmonary scanning, the scintiscan contour from the ventral or dorsal surface of the thorax usually results in a bimodal, three-dimensional distribution, as shown in figure 7, left frame. A technique has been developed for determination of the boundaries of perfused areas of the right and left lungs from these data. Radiation count values at background levels are eliminated by subtracting from all matrix elements a value equal to a fraction of the peak count value in the matrix. No negative count values are allowed; count values less than zero are set equal to zero. This has the effect of eliminating all border matrix elements whose count values were not significantly above background. Next, the left and right perfused interlung border approximations are found by locating the minimal data values residing on each row between the two bimodal distribution peaks. Figure 7, upper right frame, relates

the conventional contour map of the three-dimensional pulmonary scintiscan data to the computer-determined map of the sampling points over the left and right lungs at which count values were significantly above background levels. The shape and area of these computer-generated plots are presumably related to a dorsal-ventral projection of the perfused areas of the two lungs. The outlines of the lungs, determined independently from a posteroanterior roentgenogram of the chest, have been superimposed upon these plots by the technique described in a later section of this report. By summing separately the count values obtained at the sampling points contained in these computer-determined left-and right-lung regions, and taking the ratio of these sums to the total of the two sums, a value is obtained which is presumably related to the fraction of cardiac output traversing the left and right lungs. The ratio of the total number of data points within the computer-determined boundaries of each lung region within which count values were significantly above background to the total number of data points over both lungs is presumably related to the ratio of area of each lung perfused to the total area of lung perfused in a dorsal-ventral projection of the thorax. The values for the fraction of cardiac output traversing each lung, and the fraction of total perfused lung area contained in each lung, are given in the right lower panel of figure 7. The ratio of the fraction of cardiac output traversing each lung to the fractional area of perfusion for each lung is presumably related to the density of perfusion of the respective lung. Investigations

in this laboratory, based on pulmonary scintiscans of the thoraces of experimental animals (chimpanzees and dogs) following injections of microspheres and carried out during variations in the magnitude and direction of the gravitational-inertial force environment, indicate the above parameters to be of physiologic significance.

Superpositioning of Anatomic Boundaries onto Scintigraphic Data. The superpositioning of anatomic boundaries derived from roentgenograms (which contain an unknown amplification factor) onto scintiscan contour maps (which may also contain an unknown amplification factor) may be accomplished by the following procedure: As depicted in figure 8 (left frame), three lead markers (letter O's) are placed on the skin surface overlying the organ under study (for example, the lungs) prior to taking the roentgenogram. These lead markers are located in a plane parallel to the x-ray film and in a triangular configuration which spans the external boundaries of the lungs. The position of the animal is then adjusted so that the center of the x-ray beam passes through the center of this triangle. The silhouettes of these markers determine a circle on the resulting roentgenogram. The center of this circle can be found by drawing in any two of the sides of the triangle and marking the midpoints of these sides. The intersection of the perpendicular lines (c and d, fig. 8) drawn through the midpoints of these sides determines the center of the circle which will pass through each of the lead marker locations. If the center of the x-ray beam has been carefully aligned with the center

of this circle, all dimensional amplification on the resultant roentgenogram is relative to this known common point.

Next, these lead markers are removed from the subject and their anatomic surface locations carefully marked on the skin with pieces of adhesive tape. The scintiscan is then made in the usual manner. However, during the scanning process, each time the collimator's focal light beam passes one of the adhesive tape markings, the remote computer station's interrupt system is depressed, thus marking the position of each marker on the resultant scintiscan matrix. With this procedure, positions of the lead markers have been projected onto the scintiscan contour map and may be used to generate a circle similar to the one created on the roentgenogram.

The common centers of the respective circles on the roentgenogram and the contour map are used to define a point from which anatomic features may be transferred from the x-ray to the scintiscan contour map. The ratio of the scintiscan circle radius to the roentgenogram circle radius defines the overall roentgenogram-to-scintiscan amplification (or reduction) factor. To transfer any particular anatomic point from the roentgenogram to the scintiscan contour map, the distance from the circle's center to the anatomic point in question is measured on the roentgenogram. The length of this line  $f$  (fig. 8, left frame), when multiplied by the above-calculated amplification (reduction) factor, determines the length of line  $f'$  (fig. 8, right frame), which delineates the distance of the

anatomic point from the center of the reference circle on the scintiscan contour map. A common reference angle  $\theta$ , which specifies the spatial orientation of the lines  $\underline{f}$  and  $\underline{f}'$ , is determined by drawing through each of the roentgenogram and contour-map circle centers another line  $\underline{a}'$  parallel to the line  $\underline{a}$ . By repeating the anatomic relocation sequence for a number of different boundary points, an exact transfer of organ boundaries (for example, the lungs), as taken from the roentgenogram, can be made to the scintiscan contour map without a precise knowledge of the amplification (distortion) characteristics inherent in either the roentgenographic or scintigraphic systems.

Radioactive Microspheres in Pulmonary Scintiscanning. Radioactive microspheres\* are being used to study pulmonary blood-flow distributions in experimental animals. Our methodology for injecting the microspheres is to obtain the carbonized microspheres ( $35 \pm 5 \mu$  diameter; specific gravity 1.4) containing approximately 1 millicurie of activity per 10,000,000 spheres and to suspend these microspheres in 1 ml of isotonic sodium chloride solution after they have been washed in a diluted Tween 80 (polyoxyethylene (20) sorbitan mono-oleate) solution. Tween 80 is a biocompatible detergent which has been found to eliminate the aggregating tendency of the beads (23). The washing of the microspheres in the solution is done by placing 1 ml of the concentrated detergent into 10 ml of warm sodium chloride solution and shaking the microspheres in this solution until all visible aggregation disappears. Ten milliliters of

---

\*Minnesota Mining & Manufacturing Co., St. Paul, Minn.

Tween-free saline are then added to the microsphere-detergent solution and, after shaking, the spheres are allowed to sediment to the bottom of the container and as much of the supernatant fluid is removed as possible. In our experience, two washings with sodium chloride solution have been sufficient, following which 1 ml of sodium chloride solution is added to the microspheres. Preparation of the microspheres in this manner allows the detergent solution to come in contact with the surfaces of the microspheres, and thereby decreases the adherent properties of the spheres. The microsphere-sodium chloride solution is then aspirated into a plastic, 2-ml disposable syringe, equipped with a rubber-tipped plunger, and transferred into a segment of polyethylene tubing which has stopcock adapters at each end and an internal volume somewhat greater than 1 ml. This fluid-filled tubing containing the microspheres is made air-free, and then interposed between a solenoid-controlled pneumatically powered injection syringe and a cardiac catheter (size 6F Rodriguez type) whose blind-end spray tip is positioned at the desired injection site, such as the outflow tract of the right ventricle. The entire contents of the tubing are flushed into the animal at a preselected phase of the respiratory and cardiac cycles by injection of 8 to 10 ml of Ringer's solution from the electronically controlled injection syringe.

In an effort to determine the relationship between the scanned regional distribution of isotopes in the thorax measured by external scintiscans and the actual distribution of the isotopes in the lungs, radioactive

microspheres (tagged with either  $^{169}\text{Yb}$  or  $^{85}\text{Sr}$ ) were injected into the right ventricular outflow tract of three dogs under morphine-sodium pentobarbital anesthesia and supported in the supine or prone position by form-fitting half-body casts. Each animal was then killed by intravenous sodium pentobarbital and the airway pressure maintained at 30 cm of water pressure via an endotracheal tube until rigor mortis developed. The thorax of each animal was scanned, using the previously described scintiscanning system, while the animal lay in the right or left decubitus position. Following the scintiscanning, the lungs were removed intact from the animal, reinflated under airway pressure of 30 cm of water, and allowed to dry at room temperature for 3 to 4 days according to the method of Reed (24). At the end of the drying period, the lungs were embedded in urethane foam and again scanned in analogous right and left decubitus positions. Thereafter, the embedded lungs were sectioned into 1-cm-thick slices, parallel to the animal's coronal plane, and multiple 1-ml segments cut from each slice and analyzed for isotope content, using a well-type scintillation counter. The area of the lung contained in each slice was measured, using a planimeter. The total isotope count in each slice was then calculated by multiplying the average counts per second per milliliter of lung by the volume of the slice in milliliters. Dimensionally similar units were obtained with the scintiscan data by averaging the data along each row of the count matrix. Corrections for lung dimensional changes occurring with lung exteriorization were made from roentgenograms taken

of the dead, intact dog at the time the scintiscans were made, and from direct measurements of the exteriorized lung before encasement in urethane foam. The results from three different measurements of average isotope counts versus vertical lung distribution for three different dogs are plotted in figure 9.

### III. DISCUSSION

Digital Computer-Controlled Data Acquisition and Storage. The relatively high cost of operation of scintiscanning equipment by feedback regulation from a conventional digital computer can be justified only when the logic and decision-making capabilities of the computer proper, plus the rapid display and plotting capabilities of computer-controlled peripheral equipment, can be utilized. Some exceptions to this statement do exist and will be discussed. In general, however, the use of a digital computer merely as a storage medium or for facilitating transfer of scintiscan data onto storage devices such as digital tape and magnetic drums is not warranted since many types of peripheral scintiscan hardware are available which perform the task of data transfer onto computer-compatible storage mediums (26). In addition, computer processing of scintiscan data usually requires that the entire scintiscan matrix be in the computer core at the time of processing, which implies that the entire job has to be handled retrospectively as a batch process upon the termination of the scanning procedure.

One exception to the concept that it is not justifiable to use



a computer simply as a data-transfer or storage device occurs when information about scintiscan data must be known during the scanning procedure. It may be warranted to display scintigraphic data information to an investigator or scintiscanner operator when such things as patient movement (with head and pulmonary scans) or cardiac output changes (with renograms) occur, so that decisions can be made as to the validity of the data being acquired. Along somewhat similar lines, the computer itself may detect many types of external or physiologic events (for example, the phase of respiration) which may alter scintiscan data, and thus use the occurrence of such events in a feedback mode to regulate the sampling (that is, count time) intervals during which the scintiscanner may operate. In this case, the logic and decision-making capabilities of the computer are being used to control the scintiscanning process and these, rather than the data-gathering and storage capabilities of the computer, are the primary reason for its employment.

The obvious use of the computer in scintiscan methodology is for the computer to control the spatial coordinates where data samples should be taken and/or the duration of the sampling (counting) periods at each spatial position. For spatial control, the use of "hill climbing" techniques (28) for locating concentrated and sparsely populated isotope regions appears to be promising. For control of the duration of sampling periods, the magnitude of the accumulated counts at various locations necessary to achieve the required degree of statistical accuracy is a logical design criterion. Computer control of sampling periods can also

be used to optimize the scintiscan process by programming so that minimal periods are taken where only background levels are evident and prolonged sampling periods are used to map out, with optimal accuracy and efficiency, regions of particular interest, such as the borders of tagged organs as well as peaks and valleys within the organ indicated to the computer by the count values obtained from neighboring sample positions.

The computer-scintiscanner interaction scheme presented in this paper was designed to fulfill criteria which would allow for its operation in any of the previously discussed operational modes. In pulmonary scanning, where it is being primarily used, the control functions of the computer have been to modulate the dwell-time interval, allowing sampling to take place only at end-expiration periods (where respiratory rate permits), store and display the acquired scintiscan data elements, and designate the spatial sampling positions. This computer-scintiscanning operational mode has proved to be very reliable in practice, using a time-shared Control Data processing facility incorporating a CDC 3200 central processor accessible from a remotely located peripheral input-output station.

Some discussion should be given to the mode of data transfer from the scintiscanning assembly to the computer. When sampling time is more important than data accuracy, analog-to-digital (A/D) transfer is most efficient, for only one data line per data channel must be sampled.

However, with a 10-bit A/D converter, only count values up to 1,023 can be transferred accurately; values above 1,023 must be taken in two bytes, scaled down with a corresponding loss in accuracy, or the least significant bit(s) not transferred. When data accuracy is most important, digital-to-digital transfer is generally best. For a 15-bit register, serial sampling of the 15 bits from a single input data line per channel provides a counting range of from zero to more than 32,000. One parallel sampling operation requires 15 input data lines per channel, and gives a shorter data-transfer time with the same data accuracy. Experience in this laboratory indicates that, with the usual level of radioisotope injections (not exceeding 1 millicurie of  $^{131}\text{I}$ ) used in most pulmonary scanning procedures, the count values accumulated over a 1-second sampling period (2102A Picker collimator and a 3-by 3-inch sodium iodide crystal) seldom exceed 1,023.

The mode of scintiscanning operation presented in this paper is discontinuous in that the position of the collimator-detection head assembly is maintained constant at each specified spatial location where samples are taken and no counts are recorded during the period in which the scanner assembly is moving between successive sampling positions. This type of data sampling has been found to be a statistically accurate means of defining the boundaries between areas with and without significant isotope activity, such as the boundaries between embolized and nonembolized regions in the thorax. That this may be so can be visualized in two ways:

(1) long sampling times at any one spatial position result in good time averaging of the data-counting process, and (2) a more accurate application of mathematical, two-dimensional deconvolution routines makes possible better elimination of collimator-distortion effects resulting from energy detection from tagged beads, displaced to a greater or less degree off the focal axis of the collimator at each specific sampling site. One adverse effect of discontinuous sampling is that the period required for the scintiscan is three to four times longer, owing to the necessity of starting and stopping the collimator-detection head assembly at each sampling site.

Scintigraphic Processing and Display Routines by Digital Computer.

Aside from the ability of the computer to process and display scintiscan data immediately upon termination of the scintiscan procedure, the information content being displayed and, therefore, the data-output format are quite important. Contour maps act as inherent filters of scintiscan data in that all matrix elements falling into one particular stratification level are displayed with that level's alphanumeric character. Small data irregularities are consequently smoothed out in the display process, leaving only gross spatial distribution changes. The additional use of three-dimensional surface contours tends to alleviate this problem somewhat in that small data irregularities are depicted. However, to adequately visualize the many available positions in which small data irregularities may occur requires four three-dimensional surface representations. Another

method to detect small irregularities is to use a combination of contour maps where each map has a differing number of stratification levels.

In general, however, combined use of contour maps and four three-dimensional surfaces appears to display isotope spatial distribution information in the most readily comprehensible form.

Transforming the scintiscanning data into a three-dimensional picture, as detailed in the methods section, does not give a rotated distribution. What it does give, however, is a transformed picture consisting of a slightly skewed view of data slices which have been "slipped" upward and to one side, but where all parallel lines still remain parallel after the transformation (29). The degree of skewness given, although minimal, is due to the quantizing nature of the printer's line and character spacing. For larger scintiscan matrix rotations, true three-dimensional axis rotations must be performed; however, the printer line and character spacing will ultimately determine the final view displayed. The only alternative to this quantizing problem is to use analog display devices, such as cathode-ray tubes or x,y plotters. We have found, however, that the printer-produced three-dimensional plots and contour maps are very satisfactory for fast and informative hard-copy output of scintiscan data. Methods for more elaborate and possibly more accurate hard-copy computer-generated multidimensional displays of data using cathode-ray tubes, rapid incremental plotters (such as the Calcomp), and stereoscopic television techniques are under development (26,30).

A Method for Converting Pulmonary Scintiscan Data into Fractional Blood-Flow Values. After collimator-distortion effects have been removed from spatially distributed scintiscan data, the resultant matrix elements are equal to the isotope counts which would be obtained from isotopic material lying only on the focal lines of the collimator at each sampling site. Whether these count values are linearly proportional to the actual regional blood flow to the anatomic points transected by these focal lines may be questioned, in view of possible nonuniformities in tagging of the blood and radiation-absorbing factors. However, if the indicator accurately tags the blood flow and is removed completely during its first transit of the lungs, the major elements of the theory appear sound (22,23,31).

In regions where no isotope material is present, only background radiation should be detected. The boundaries of perfused regions of the lung should, therefore, be fairly easily detected by noting where the scintiscan matrix values rise significantly above background counts. Experience has shown the level of significance to be 1.5 times the value of the square root of the difference of the scintiscan matrix's maximal and minimal values. In regions where there is a reduced isotope concentration or where overlying structures have absorbed the underlying radiation energy, such as the hilar region and over the heart, regional minimal count areas are evident. We have assumed that the regional minimum between the bimodal isotopic distributions, such as seen in figure 7, represents the division line between right and left lungs. This may not be entirely

true; since the greater fraction of the heart is to the left of the mid-sagittal plane, it possibly absorbs more of the radiation emanating from the left lung than from the right. If this is the case, the computer-calculated right and left lung pulmonary blood-flow ratios would be altered in favor of the right lung. Prone scintiscans are not as subject to this cardiac-induced error. We are presently investigating this boundary definition problem; however, experimental animals having chest dimensions similar to those of humans are very difficult and expensive to obtain and sacrifice, so reported data will come primarily from phantom experiments and statistical studies made at the time of necropsy.

Superpositioning of Anatomic Boundaries onto Scintigraphic Data. The transfer of anatomic boundaries determined roentgenographically onto contour maps of isotope distribution without differences in relative distortion in the two sets of data, using the techniques presented in the methods section, are as accurate as can be obtained without the use of special techniques to obtain distortion-free roentgenographic and scintigraphic displays (32). However, some radioactivity is seen to fall outside the lung anatomic borders, as shown in figure 7. For the example presented, this apparent error is at least in part due to respiratory-induced scintiscan artifact. The average respiratory rates of the chimpanzee during the scintiscanning procedures ranged from 40 to 60 breaths per minute. These rapid respiratory rates rendered limiting of sampling periods to the end-expiratory phase of respiration practically

impossible; therefore, the scintiscanning was carried out independent of the respiratory cycle so that usually a breath occurred during each sampling period. In addition, the roentgenograms of the thorax were exposed at end-expiration and thus depict the minimal anatomic lung boundaries. Roentgenograms taken at both end-inspiration and end-expiration indicate that the outermost scintiscan boundary points lie between the end-expiratory and end-inspiratory lung borders. Therefore, the scintiscan boundary points which lie outside the end-expiration anatomic boundaries in figure 7 are an indication of respiratory-induced scintiscanning artifact.

One basic assumption inherent in this methodology is that the three lead x-ray markers were aligned so that the orientation in space of the plane defined by these markers was parallel to the roentgenographic film plate. If this is not the case, the distance from the center of the x-ray beam to the image on the roentgenogram produced by the lead marker closest to the x-ray source will be amplified to a greater extent than other markers, thus shifting the center of the circle defined on the roentgenogram and changing its radius slightly. We have used this technique, nevertheless, to transfer chimpanzee thoracic boundaries (which closely resemble human thoracic dimensions) from roentgenograms onto scintigraph contour maps, and have, in general, encountered minimal difficulties. Close attention must be paid to this problem, however, for studies requiring highly accurate boundary definitions.



It may also be pointed out that this boundary transfer technique is a convenient way for transferring the physically measured borders of radiation phantoms onto the scintiscan data obtained from such phantoms for in vitro testing of scintiscanning techniques.

Radioactive Microspheres in Pulmonary Scintiscanning. Uniformly sized microspheres appear to be suitable for studying regional distribution of blood flow since the spherical shape should cause the tagged microspheres to impact in precapillary vessels of similar internal dimension. The sphere diameter of  $35 \pm 5 \mu$  should insure practically complete removal of the spheres from the blood during their first transit through the lungs (24,33). Observations made in this laboratory and in others (23) indicate that less than 1% of injected microspheres having  $35 \mu$  diameters appear in the systemic circulation following injection in the pulmonary artery of dogs. In addition, Reed (24) has shown that the regional pulmonary distribution of the spheres is, on the average, independent of the spheres' specific gravity in the range of 0.2 to 3.0, and that distributions of replicate injections of microspheres are closely similar. Furthermore, the results, shown in figure 9, indicate that on the basis of an average count per slice, externally made pulmonary scintiscan measurements approximate very closely spatial distributions of isotope density determined by direct counts from excised lung tissue.

Clumping of microspheres prior to and during their injection must be avoided; for if the spheres do not distribute uniformly in the

blood during their injection and transport by the bloodstream, a false indication of regional flow distribution will be obtained. To this end, Tween 80 appears to be satisfactory; however, one drop of concentrated Tween injected intra-arterially in one conscious dog has been observed to lower that animal's blood pressure 100 mm Hg in 15 seconds following injection as a result of a massive vasodilatation. The same dosage injected in the same dog intravenously had no noticeable effect. The arterial injection vasodilatation ~~phenomenon~~ could not be reproduced in a second conscious dog. Pulmonary and aortic pressures have been monitored in dogs and chimpanzees during many injections of microspheres treated with Tween 80 in this laboratory and only small or no significant changes in these pressures have been observed. However, it is believed that microspheres treated with Tween 80 solution, in order to eliminate apparent aggregation, should be washed, as described in the methods section, prior to their injection.

## References

1. Nettleton, W. J., Jr. Computers, what they are and what they do. Symposium on Computers and Scanning. J Nucl Med :5 (1967).
2. Brown, D. W. Digital computer analysis and display of the radioisotope scan. J Nucl Med 5:802 (1964).
3. MacIntyre, W. J., and J. H. Christie. A comparison of data averaging or radioisotope scan data by photographic and dimensional computer techniques. Symposium on Medical Radioisotope Scintigraphy. Salzburg, Austria, August 1968 . (Proceedings of the Symposium are in press.)
4. Sprau, A. C., W. N. Tauxe, and D. W. Chaapel. A computerized radioisotope-scan-data filter based on a system response to a point source. Mayo Clin Proc 41:585 (1966).
5. Coulam, C. M., J. Greenleaf, and W. H. Dunnette. Gaussian functions for design and comparison of digital filters for scintiscan data. J Nucl Med. (In Press)
6. Pizer, S. M. Production and processing of radioisotope scans. Thesis, Harvard University, July (1967).
7. Nagai, T., and T. A. Iinuma. A comparison of differential and integral scans. J Nucl Med 9:202 (1968).
8. Iinuma, T. A., T. Nagi, and N. Fukuda. Digital data processing and display in radioisotope imaging. Symposium on Medical Radioisotope Scintigraphy, Salzburg, Austria, August 1968 . (Proceedings of the Symposium are in press.)

9. Vetter, H. G. Restoration of biological images using limited sampling. Phys Med Biol. (In press)
10. Muehllehner, G. Radioisotope imaging in three dimensions. (Abstr.) J Nucl Med 9:337 (1968).
11. Coltman, J. W., and A. E. Anderson. Noise limitations to resolving power in electronic imaging. Proc IRE May 1960 , p. 858.
12. Tauxe, W. N., D. W. Chaapel, and A. C. Sprau. Contrast enhancement of scanning procedures by high-speed digital computer. J Nucl Med 7:647 (1966).
13. Tauxe, W. N. 100-level smoothed scintiscans processed and produced by a digital computer. J Nucl Med 9:58 (1968).
14. MacIntyre, W. J., J. H. Christie, and G. S. Curtis. Three-dimensional computer read-out of radioisotope scan data. Radiology 90:22 (1968).
15. Harper, P. V., D. B. Charleston, R. N. Beck, N. Yasillo, and B. Fromes. Three-dimensional display of scanning images. (Abstr.) J Nucl Med 9:321 (1968).
16. Pizer, S. M., and H. G. Vetter. The problem of display in the visualization of radioisotope distributions. J Nucl Med 7:773 (1966).
17. Weber, D. A., P. Kenny, R. Pochaczewsky, K. R. Corey, and J. S. Laughlin. Liver scans with digital readout. J Nucl Med 6:528 (1965).

18. Spetner, L. M. Detection and location of abnormalities in radioisotope scan data. (Abstr.) J Nucl Med 9:350 (1968).
19. Harris, C. C. Quantification of scan records. Symposium on Computers and Scanning. Nucl Sci Abstr 21:3232 (1967).
20. Taplin, G. V., E. K. Dore, N. D. Poe, I. A. Swanson, D. E. Johnson, and A. Greenberg. Lung perfusion and bronchial patency evaluation by radioisotope scanning. Symposium of Computers and Medicine, 1967, p. 108.
21. Tauxe, W. N., and J. C. Hunt. Evaluation of renal function by isotope techniques. Med Clin N Amer 50:937 (1966).
22. Sapirstein, L. A. Fractionation of the cardiac output of rats with isotopic potassium. Circ Res 4:689 (1956).
23. Rudolph, A. M., and M. A. Heyman. The circulation of the fetus in utero. Circ Res 21:163 (1967).
24. Reed, J. H., Jr., and E. H. Wood. Effect of body position on regional distribution of pulmonary blood flow. J Appl Physiol (In press).
25. Warner, H. R., and A. T. Pryor. Time-sharing in biomedical research. Datamation April (1966).
26. Technology Profile: CRT Displays: Parts I, II, and III. Modern Data Systems July, p. 28; August, p. 46; September, p. 24 (1968).
27. MacIntyre, W. J., S. D. Fedoruk, C. C. Harris, D. E. Kuhl, and J. R. Mallard. Sensitivity and resolution in radioisotope scanning. Symposium on Medical Radioisotope Scintigraphy, Salzburg, Austria, August 1968. (Proceedings of Symposium are in press.)

28. Fletcher, R., and M. J. D. Powell. A rapidly convergent descent method for minimization. Computer J (Brit Computer Soc) 6:163 (1965).
29. Ahuja, D. V., and S. A. Coons. Geometry for construction and display. IBM Systems J 7(No. 3 and 4):188 (1968).
30. Schmitt, O. H. Cathode-ray presentation of three-dimensional data. J. Appl Physics 18:819 (1947).
31. Reed, J. H., Jr., and E. H. Wood. Effect of gravitational and inertial forces on regional distribution of pulmonary blood flow. (Unpublished data.)
32. Lewall, D. B., and W. N. Tauxe. A method for the elimination of magnification in roentgenograms for scintiscan superimposition. Amer J Clin Path 48:568 (1967).
33. Neutze, J. M., F. Wyler, and A. M. Rudolph. Use of radioactive microspheres to assess distribution of cardiac output in rabbits. Amer J Physiol. (In press)

**DIGITAL COMPUTER-CONTROLLED SCINTISCANNING ASSEMBLY**  
*Mode 1 Configuration*

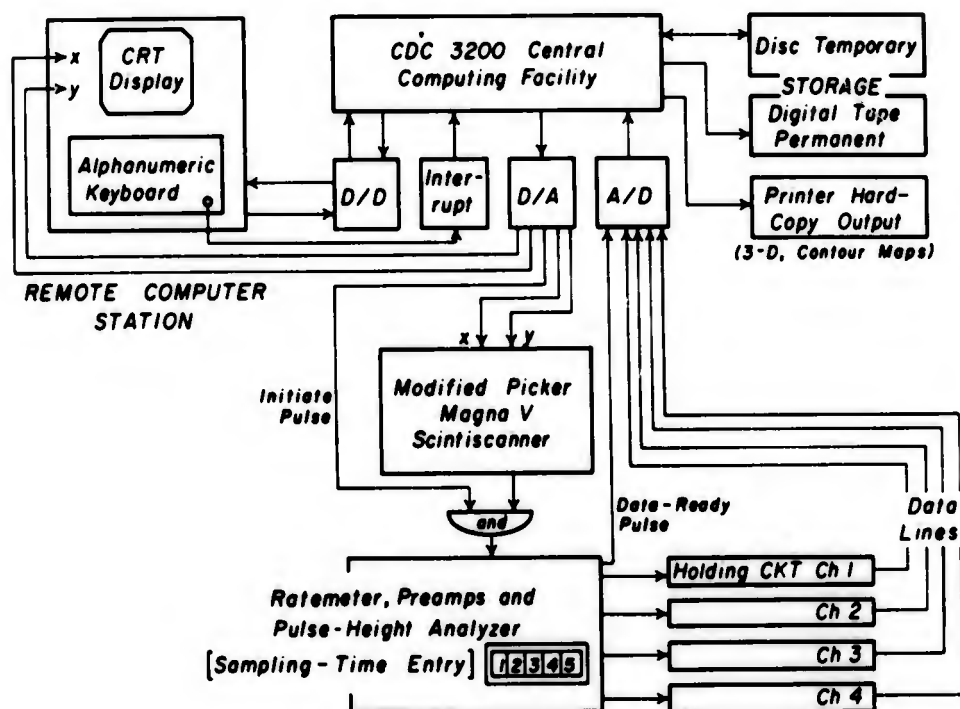


**FIGURE 1**

Block diagram of digital computer-controlled scintiscanning assembly depicting the configuration used in the mode 1 type of operation. Program initiation and alphanumeric data entry into the CDC 3200 are made via the alphanumeric keyboard of a remote computer station (fig. 3,G). The position of the scintiscanner's collimator detection head assembly (fig. 3,B) is controlled from digital-to-analog (D/A) x-position, y-position input lines, while the actual starting time of the sampling process is controlled via the D/A initiate pulse. Entry of the count values into the computer via four A/D (analog-to-digital) input lines and required sample-and-hold circuitry takes place following the computer's recognition of the A/D data-ready pulse generated by the

ratemeter assembly (fig. 3,E). The sampled data are temporarily stored, both in the computer's core memory and on disc storage packs, and the data are then transferred to digital magnetic tape for permanent storage. In this operational mode, the computer controls: (1) the x and y coordinates of the detection head's position in the scanning plane; (2) the start of the sampling (counting) period (with or without triggering logic based on physiologic events); (3) the number of samples to be taken at each x,y position; and (4) the data storage and on-line display via an oscilloscope (fig. 3,F) and, immediately following the scanning procedure, generation of three-dimensional and contour maps of the data via a high-speed printer as illustrated in figure 7. The x and y coordinate values and the count values from the four-channel ratemeter are displayed continuously in real time during the scanning procedure on the remote station storage oscilloscope (fig. 4) as the scanning procedure progresses.



**DIGITAL COMPUTER-CONTROLLED SCINTISCANNING ASSEMBLY  
Mode 2 Hardware Configuration**

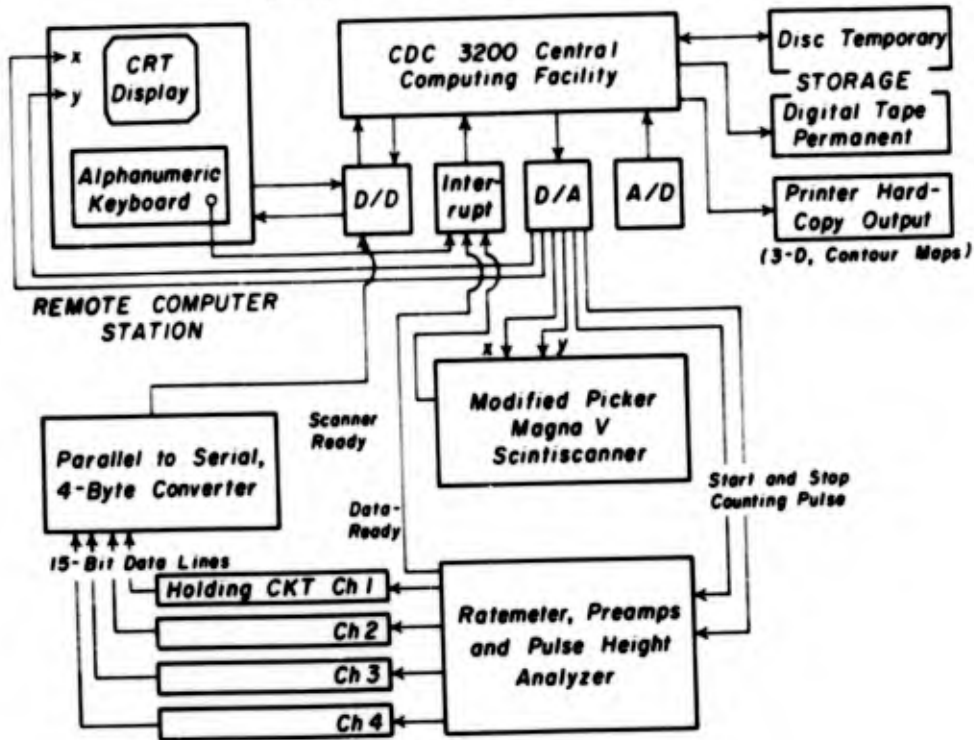


**FIGURE 2**

Block diagram of digital computer-controlled scintiscanning assembly depicting the configuration used in the mode 2 type of operation. This configuration provides more accurate data transfer into the computer via digital-to-digital (D/D) input data lines than provided by the analog-to-digital conversion system used in mode 1. Furthermore, the sampling time at each site is under the control of the computer program via the start-and-stop counting D/A pulses. Also, scanner-ready and data-ready interrupt pulses are more efficient than the mode 1 A/D input pulses. Each input data channel contains 15 D/D input lines; therefore, four data bytes are required to sample the four isotope energies available. In this mode, the computer has programmable

control over all facets of the scintiscan operation. Fifteen input binary data lines provide the capability of recording count values ranging from 0 to 32,768, compared to a range of 0 to 1,023 for the 10-bit A/D

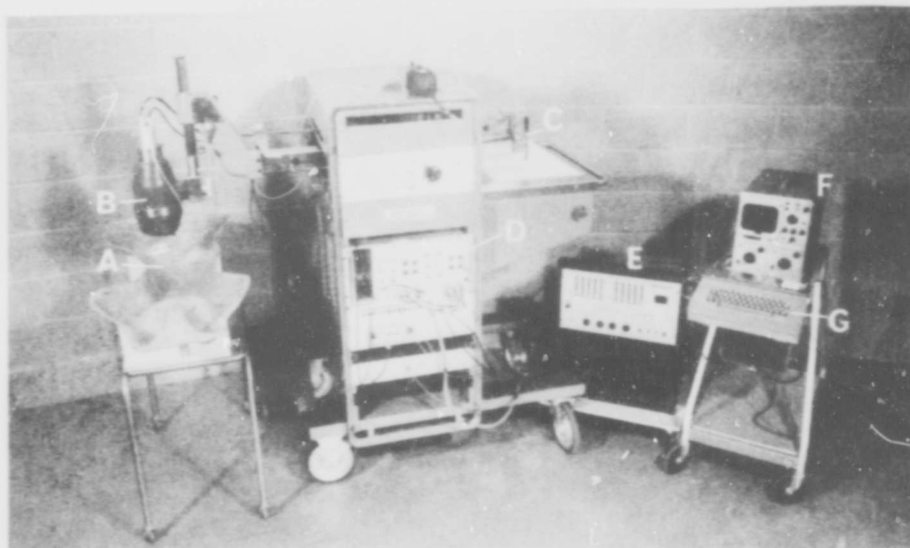


FIGURE 3

Computer-controlled Magna V scanner assembly

(Picker). A, half-body molded cast to maintain body position of chimpanzee constant during scanning procedure; B, collimated sodium iodide scintillation detector; C, writing arm; D, electronic assemblies for detection and positioning components of scintiscanner; E, two-channel counting assembly, one of two required; F, storage oscilloscope for computer output display at remote computer station (fig. 4); and G, keyboard for remote computer interrupt, program selection, and entry of auxiliary alphanumeric data prior to on-line processing of data from scanning assembly.



corner of the plane traversed by the aperture of the scanning head assembly is designated as (0,0); the upper right-hand corner is equated with (1023,1023). This type of on-line data feedback to the operator is advantageous since it allows judgments of the nature and consistency of the data being recorded and simultaneous monitoring of the subject being scanned.

### COMPUTER-PRINTED DISPLAYS OF SCINTISCAN DATA FROM THYROID PHANTOM

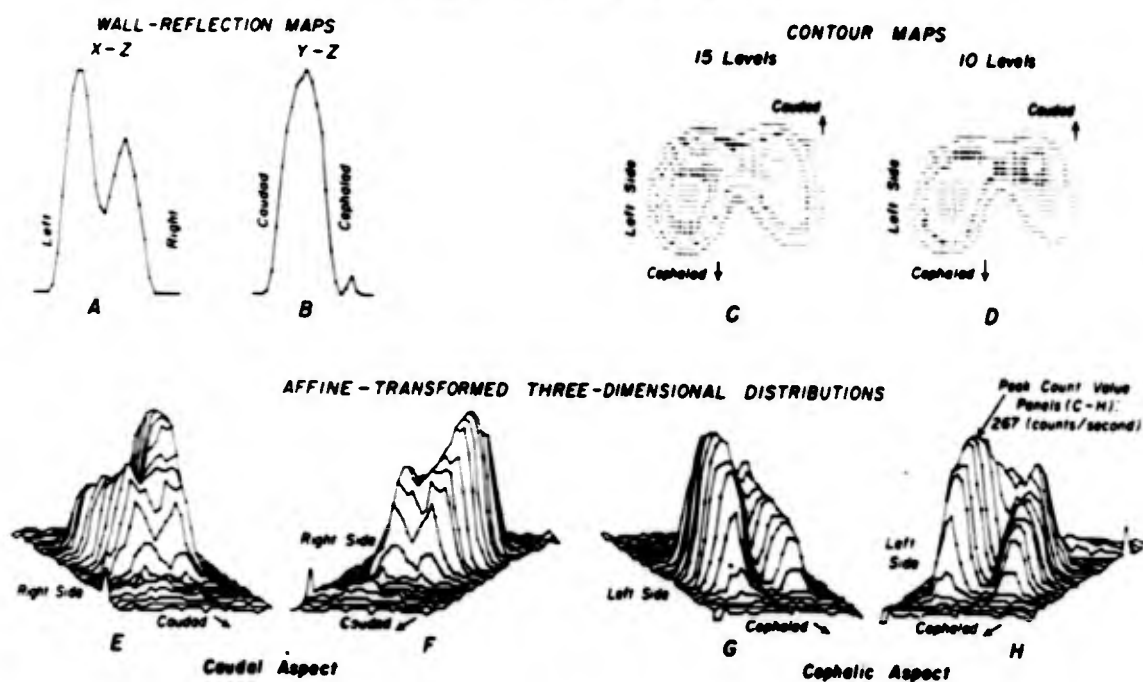


FIGURE 5

Illustration of computer-generated displays of scintiscan data obtained from a thyroid phantom. The complete display consists of x-z and y-z wall-reflection maps (A,B), four three-dimensional count distributions (E-H), and two isocount contour maps

(C,D) showing 15 and 10 data-stratification levels. The three-dimensional maps have been formed by hand-connecting all of the printed data points which constitute one row of the scintiscan matrix. Data points from an individual row are designated by a specific alphanumeric symbol. The height of each symbol above the tilted forward and skewed x-y reference plane is directly proportional to the count level measured at this point. The contour-map symbol hierarchy depicting increasing count values or isotope density is ,-,A, ,+,B, ,:,C, ,=,D, ,/,E, ,\*,F, ,#. In general, contour maps show best the regional differences in isotope density, while the three-dimensional plots provide a picture of the minute details of the spatial distribution of the isotope. The wall-reflection maps depict average isotope density changes in right-to-left or dorsal-to-ventral directions. The peak count value for panels (C-H) was 267 counts/second above background. The average background count level upon which these plots are superimposed was less than 10 counts/second. The sampling time for each data point was 2 seconds.

COMPUTER METHOD FOR GENERATING AFFINE-TRANSFORMED  
THREE-DIMENSIONAL DISTRIBUTIONS FROM SCINTISCAN DATA

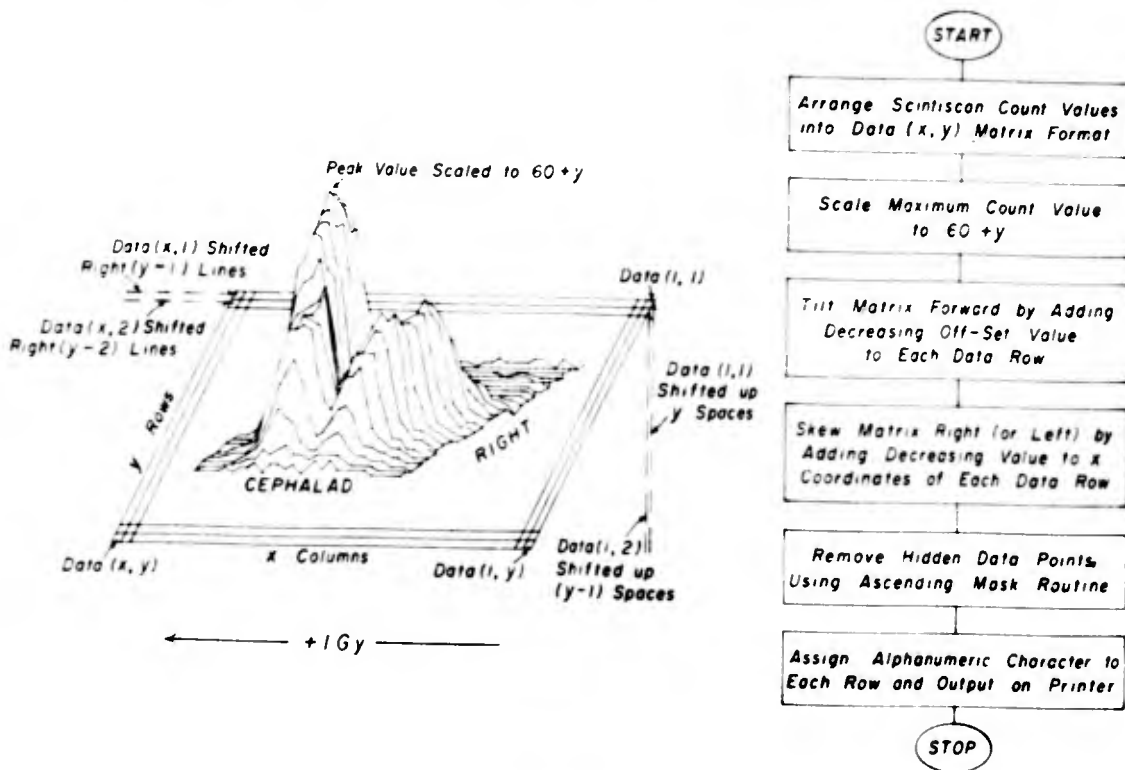


FIGURE 6

Diagram of computer method for generating a simulated three-dimensional display of scintiscan data. The count matrix was obtained by scanning the ventral surface of the thorax of a chimpanzee following injection of  $^{141}\text{C}$ -tagged microspheres into the right ventricle while in the left decubitus (+1Gy) position. "Data" is the computer-program term for count value; "y" is the number of rows of count values in the total scintiscan data (that is, the number of right-to-left traversals of the thorax by the scintiscanning collimator required to cover the total cephalocaudad dimension of the thorax); "x" is the number of samples taken during each right-to-left traversal of the thorax. The computer-generated incremental change in position of the

scanner head in the x (right-to-left) direction was 1.0 cm per step, and the increment in the y (cephalocaudad) direction was 0.86 cm per step. Peak count value, shown in this display, is 163 counts per second above background. The average background count upon which the plot is superimposed was less than 8 counts per second, and the sampling time for each data point was 3 seconds.

The display is plotted crosswise to the printer page. Therefore, the same maximal number of increments available for the z and y axes is determined by the number of spaces across the printed page, while the maximal number of increments on the x axis is determined by the maximal number of lines per single printed page. The magnitude of the shift of the upper portion of the diagrammatic matrix lines has been arbitrarily reduced for the purposes of this diagram so that the upper right corner is not hidden by the count values. The lines connecting individual count values in each row of data (identified by a specific alphanumeric character) were drawn manually. Note that the scintiscan data appear tipped forward, skewed right, and partially erased (hidden lines removed), thus producing a three-dimensional effect.

COMPUTER GENERATED DISPLAYS OF SCINTISCAN DATA  
FROM SUPINE SURFACE OF THORAX

(CHIMPANZEE, AFTER INJECTION  $S^{85}$  TAGGED MICROSPHERES  
INTO RIGHT VENTRICLE, RIGHT DECUBITUS POSITION)

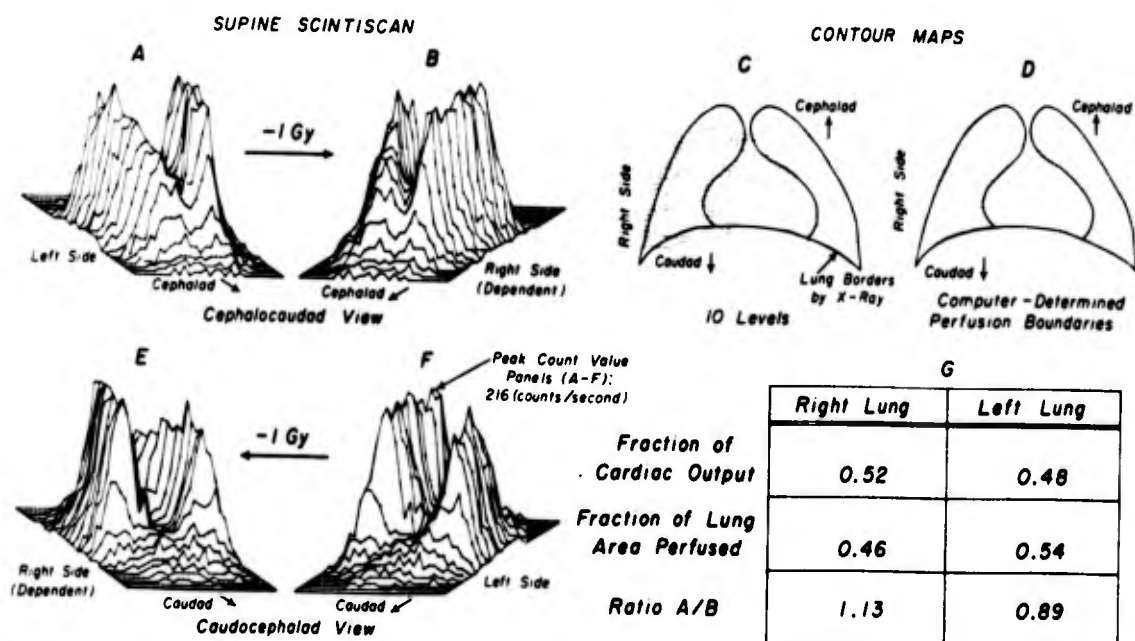


FIGURE 7

Example of computer-generated displays of data obtained by computer-controlled scintiscan of the ventral surface of the thorax of a chimpanzee. The animal was anesthetized with intramuscular phencyclidine (Sernylan) and morphine, plus intravenous sodium pentobarbital. Prior to the scintiscan, 1 millicurie of  $^{85}\text{Sr}$ -impregnated microspheres ( $35 \pm 5 \mu$ ) was injected into the pulmonary circulation via a catheter positioned in the right ventricular outflow tract while the animal was maintained in the right lateral position by a half-body cast. The scan was made with the animal supine, using a 2102A Picker collimator and a 3 by 3-inch sodium iodide crystal. The x-direction intersample spacing was 0.86 cm, and y-direction intersample spacing was 1.0 cm.



Panel C is a conventional 10-level contour map, and panel D shows all sampling sites contained within the computer-recognized perfusion boundaries of the two lungs. The anatomic boundaries of the lungs, as visualized by an anteroposterior thoracic roentgenogram, have been projected onto these maps (heavy lines) using the methodology described in the text. The lower right frame shows the fractions of total pulmonary blood flow and of the total pulmonary perfusion area for the left and right lungs, respectively, calculated by the computer. The values indicate that 52% of the chimpanzee's cardiac output traversed his right, dependent (with respect to gravity) lung, and 48% traversed the left, superior lung. The area over which perfusion was detected in the right lung was 46% of the total perfused area, as compared to an analogous value of 54% for the left lung. The calculated ratio of blood flow to perfused areas was 1.1 for the right lung, and 0.9 for the left, superior lung, thus indicating a greater blood perfusion in the dependent lung. The left frame depicts the four computer-generated three-dimensional plots of count values obtained at the respective sampling sites in the scanning plane. The peak count value for panels A-F is 216 counts per second above background. The average background count upon which these plots are superimposed was less than 10 counts per second. The sampling time for each data period was 3 seconds.

GRAPHICAL METHOD FOR TRANSFERRING X-RAY ANATOMICAL BOUNDARIES ONTO COMPUTER-PRODUCED CONTOUR MAP OF SCINTISCAN DATA

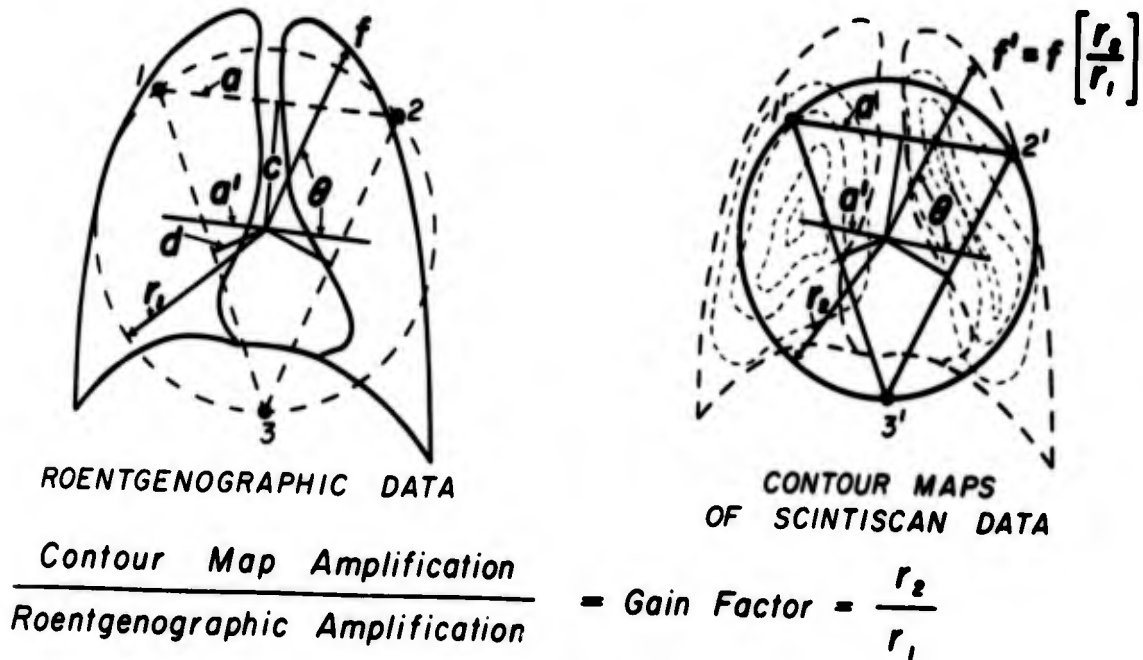


FIGURE 8

An illustrative guide by which anatomic boundaries determined from a roentgenogram of the thorax can be projected in correct spatial proportions onto computer-generated contour maps of scintiscan data. The lead markers 1, 2, and 3 on the thoracic roentgenogram and the corresponding indexed sites 1', 2', and 3' on the contour map define circles which describe the relative x-ray and contour-map amplification factors (that is, the ratio of the radii of these circles on the contour map and roentgenograms, respectively, defines the ratio of these amplification factors to each other). For this to be valid, the position of the animal for the chest roentgenogram must be carefully adjusted so that the center of the x-ray beam passes through the center of the triangle defined by

the lead markers and the plane defined by these lead markers must have been parallel to the roentgenographic film. The distance of any point  $\underline{f}$  on the border of the lung plus its orientation angle  $\theta$  designates the position of the anatomic point on the roentgenogram. An exact transfer onto the contour map can be calculated by multiplying the distance,  $\underline{f}$ , by the amplification factor ( $\underline{r}/\underline{r}'$ ) to obtain the distance  $\underline{f}'$ . This distance and the invariant angle  $\theta$  define the position of the anatomic point on the contour map.

COMPARISONS BETWEEN ROW-AVERAGED, EXTERNALLY MEASURED, LUNG SCINTISCANS; EXTERIORIZED, URETHANE-EMBEDDED, LUNG SCINTISCANS; AND WELL-TYPE SCINTILLATION-COUNTED LUNG SAMPLES

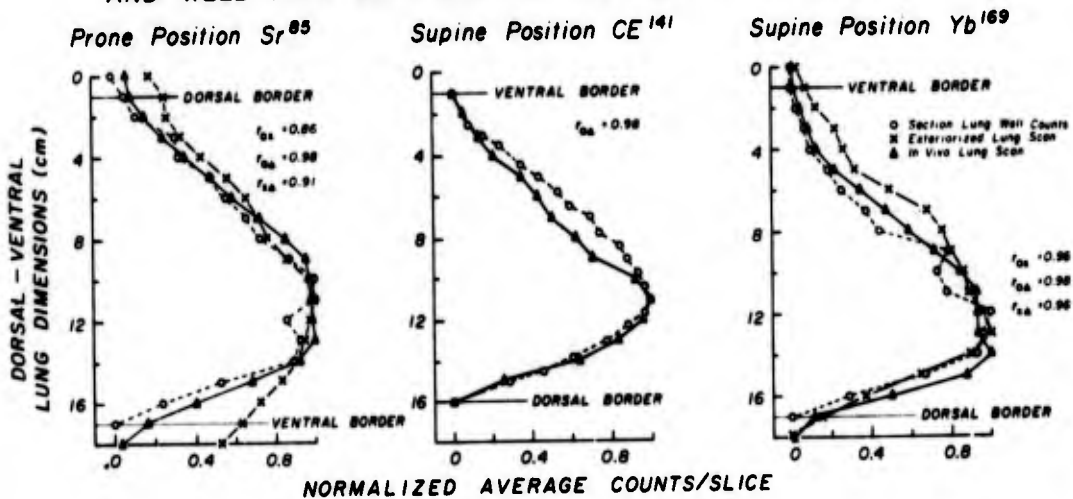


FIGURE 9

Comparative results from three dogs illustrating the similarity between average regional blood-flow distributions obtained by (1) row-averaging scintiscan data made over the surface of the dog's thorax which was intact, but with the lungs distended by an airway

pressure of 30 cm of water following a fatal intravenous dose of sodium pentobarbital; (2) row-averaging scintiscan data made from the lungs of the same dog after they had been exteriorized and embedded in urethane foam; and (3) averaging multiple scintillation-well-counted lung samples taken from 1-cm thick coronal sections of the embedded lung. All count values were corrected to counts per second per slice of lung tissue. Corrections for anatomic dimension changes were made from x-ray and actual exteriorized lung measurements. The notation  $r_{0\Delta}$  depicts the correlation coefficient relating the 0 and  $\Delta$  indicated curves, and so forth. The position of the animal at the time of injection of the microspheres and the isotopes used to label the microspheres are designated by the respective panel titles.

**II. SMOOTHING TECHNIQUES APPLICABLE TO  
SCINTISCAN DATA**

**PRECEDING PAGE BLANK**

## ABSTRACT

A method of comparing digital computer-produced smoothing algorithms for use with scintiscan data is presented along with a method for designing appropriate smoothing schemes. These methods require both a point-source response (PSR) matrix recorded from the isotope detection system used and the computation of a gaussian function which best approximates that recorded PSR. Transformation of the recorded PSR and its gaussian approximation into the spatial-frequency domain by using a Fourier series analysis indicates that the spatial-frequency components of the gaussian function provide a good criterion against which the spatial-frequency components of the PSR may be compared. In addition, by letting the gaussian spatial-frequency components constitute the output of a computing algorithm, of which the spatial-frequency components of the recorded PSR are the input, the algorithm's smoothing characteristics may be determined. A study made on thyroid phantom data indicates that optimal scintiscan data smoothing is related to the collimator-isotope detection system and the actual scintiscan conditions used.

PRECEDING PAGE BLANK

## I. INTRODUCTION

Numerous algorithms related to spatially weighted data averaging and statistical decision-making schemes have been described for smoothing scintiscan data (1-8). However, practically all methods of smoothing depend on some type of integration scheme. For example, the smoothing may be done using the integrating properties of the display process, such as occurs in level-quantizing in contour map displays (1,2) or in the process of spot-size overlap during film exposure (3,4). It may also be done digitally using digital computers, before the display process (5,6). But no matter how the smoothing is accomplished, the choice of which smoothing scheme to use in the filtering process is difficult in that no definite criteria have been established by which the smoothing properties of the various filtering schemes may be compared.

The purpose of this paper is (1) to describe a means for comparing digital computer smoothing techniques applicable to scintiscan data and (2) to introduce a method of design of digital filters which incorporates characteristics of the recording system into the design process.

## II. METHODS

To demonstrate the different filtering properties of fixed spatial averaging techniques, three types of digital smoothing algorithms were taken from the literature and programmed for execution on a Control Data Corporation 3200 digital computer. The smoothing algorithms are

(a) a five-point, weighted-data-averaging technique (3), (b) a statistical decision-making scheme (7), and (c) a modified version of (a) in which some characteristics of the collimator-recording system are used in the smoothing process (8).

Point-source responses were chosen as the test data from which comparison of the smoothing properties of these algorithms could be accomplished. Point-source responses from each of the radionuclides  $^{169}\text{Yb}$ ,  $^{141}\text{Ce}$ ,  $^{51}\text{Cr}$ ,  $^{131}\text{I}$ , and  $^{85}\text{Sr}$  were obtained by scintiscanning a 20- $\mu\text{Ci}$  sample of each isotope. Each isotopic source was spherical (1 mm in diameter); it was positioned 4 inches from the face of a Picker 2102A, 31-hole medium-focus collimator which was interposed next to a 3-by 3-inch sodium iodide (Tl) crystal, and it was spatially located at the center of a 12.7 by 12.7-cm area. The count rate matrix was obtained by counting for 2 or more seconds at each of 31 by 26 (x,y) locations, using a specially designed digital computer-controlled scintiscanning system (1). This scanning procedure resulted in a spatial matrix having 0.41 cm between the x-direction sample points and 0.51 cm between the y-direction sample points. Figure 1 illustrates a typical point-source response from  $^{131}\text{I}$ . In this display, each alphanumeric symbol of the three-dimensional surface corresponds to a discrete x,y sample position. The vertical height of the symbol above its respective x,y position corresponds to a count value above a reference plane which has been tilted upward and to the right for the purpose of this display. The generation of three-



dimensional display formats by digital computer has been described elsewhere (1).

Each of the point-source response matrices was then smoothed by each of the three filtering schemes, as described in equations 1 through 5. The first smoothing method, the five-point weighted-data smoothing technique, generates a smoothed data matrix by replacing each element of the original array with an average value found from the sum of a doubly weighted central element value and each of its four immediate neighboring element values, according to a description by MacIntyre and Christie (3).

$$D(n,m) = \frac{1}{6} \left[ C(n-1,m) + C(n,m-1) + 2C(n,m) + C(n+1,m) + C(n,m+1) \right] \quad (1)$$

$$n = 1, 2, \dots, N; \quad m = 1, 2, \dots, M$$

in which  $n, m$  indicate the  $x, y$  point to be smoothed;  $D(n, m)$  and  $C(n, m)$  are the smoothed and original data arrays, respectively; and  $N$  and  $M$  are the maximal matrix dimensions. This smoothing process is referred to in this paper as a 1:2:1 smoothing scheme.

The second method, the statistical filtering technique proposed by Brown (7), makes use of a weighting process and statistical decision-making scheme in which one calculates the mean and standard deviation of the eight data elements immediately surrounding the central element to be smoothed. If the count value of the central element is greater than, or less than, the mean value of its neighbors by one standard deviation, it is replaced with the calculated mean; otherwise, the central element value

remains unchanged. The entire count matrix is then smoothed by averaging each element with the mean of its eight neighbors. Mathematically,

$$\bar{C}(n,m) = \frac{1}{8} \left[ \sum_{i=n-1}^{n+1} \sum_{j=m-1}^{m+1} C(i,j) \right] \quad (2)$$

$$C(n,m)_{\text{std}}^2 = \frac{1}{7} \left\{ \sum_{i=n-1}^{n+1} \sum_{j=m-1}^{m+1} [C(i,j) - C(n,m)]^2 \right\} \quad (3)$$

in which  $i$  and  $j$  cannot be equal to  $n$  and  $m$  simultaneously. Finally,

$$D(n,m) = \frac{1}{2} [C(n,m) + \bar{C}(n,m)] \quad (4)$$

$$n = 1, 2, \dots, N; \quad m = 1, 2, \dots, M$$

in which  $C(n,m)$ ,  $D(n,m)$ , and  $n,m$  are as before.

The third smoothing scheme is the point-source response convolution technique, after a description by Sprau and associates (8), and is a method of smoothing whereby each of the elements surrounding some central element is weighted with values proportional to the collimator's recorded point-source response. In this scheme,

$$D(n,m) = \sum_{i=1}^n \sum_{j=1}^m C(n-i+1, m-j+1) h(i,j) \quad (5)$$

$$n = 1, 2, \dots, N; \quad m = 1, 2, \dots, M$$

in which  $N$  and  $M$  define the maximal dimensions of the  $C(n,m)$ , and  $h(i,j)$  is the normalized (to unit volume) collimator point-source response count matrix; and  $n,m,C(n,m)$ , and  $D(n,m)$  are as before. Equation 5 is a difference-equation representation of the two-dimensional convolution process.

To compare the smoothing properties of each of these smoothing schemes, we elected to compare the amount of attenuation each smoothing scheme gives to each of the spatial-frequency components of the collimator's point-source response. Representative frequency components of the smoothed and original point-source response count matrices are found from a Fourier series analysis of the data elements from the row (or column) which passes through, or nearest, the maximal value of the count matrix. These amplitude and phase characteristics are designated as  $A(i)$  and  $B(i)$ , respectively, and represent the spatial-frequency components of the scintiscan matrices. They are computed as follows.

$$a(i) = \sum_{j=1}^N f(j) \cos (2\pi ij/N) \quad i = 0,1,2,\dots,N/2 \quad (6)$$

$$b(i) = \sum_{j=1}^N f(j) \sin (2\pi ij/N) \quad i = 1,2,\dots,N/2 \quad (7)$$

and

$$A(i) = \left[ a(i)^2 + b(i)^2 \right]^{1/2} \quad (8)$$

$$B(i) = \tan^{-1} \left[ b(i)/a(i) \right] \quad (9)$$

for  $b(0) = 0$  and  $i = 0, 1, 2, \dots, N/2$ . With these equations,  $a(i)$  and  $b(i)$  are the cosine and sine amplitude coefficients and  $N$  is the number of elements used in the  $f(j)$  data row (or column).

The reconstruction of spatial count values from their original or modified Fourier series components may be obtained using equation 10.

$$f(j) = a(0)/2 + \sum_{i=1}^{N/2} \left[ a(i)\cos(2\pi ij/N) + b(i)\sin(2\pi ij/N) \right] \quad (10)$$

$$j = 1, 2, \dots, N.$$

Figure 2 (lower) shows a frequency-domain representation of an  $^{85}\text{Sr}$  point-source response which has been digitally smoothed using the smoothing algorithms described above. The spatial-frequency amplitudes,  $A(i)$ , are plotted against the spatial-frequencies,  $i$ , and show the amount of attenuation each filtering scheme gives to each spatial-frequency component of the original data.

The purpose of smoothing is to remove random fluctuations in the scintiscan data, retaining only the essential information. The essential information for point-source responses is defined in this paper as the shape of the gaussian function which fits most closely the recorded point-source response. The point-by-point count differences which exist

between the recorded point-source response and its best-fit gaussian curve are therefore taken as a measure of the randomness contained in the signal information. The description of the gaussian function which will most closely approximate a point-source response is found by first removing background counts by subtracting from the entire count matrix a value equal to 1.5 times the square root of the difference between the maximal and minimal values of the matrix and then computing the means and standard deviations,  $\bar{x}$ ,  $\bar{y}$ ,  $\sigma_x$ ,  $\sigma_y$ , by using equations 11 and 12. In these equations, only the data row and column which pass through, or nearest, the peak count data value are used.

$$\bar{x} = \frac{\sum_{j=1}^N j f(j)}{\sum_{j=1}^N f(j)} \quad (11)$$

$$j = 1, 2, \dots, N$$

$$\sigma_x^2 = \frac{\sum_{j=1}^N (j-\bar{x})^2 f(j)}{\sum_{j=1}^N f(j)} \quad (12)$$

The desired gaussian curve is generated in matrix form by:

$$g(i,j) = \frac{1}{2\pi \sigma_x \sigma_y} \exp \left[ \frac{(j-\bar{x})}{\sqrt{2} \sigma_x} \right]^2 \exp \left[ \frac{(i-\bar{y})}{\sqrt{2} \sigma_y} \right]^2 \quad (13)$$

$$i = 1, 2, \dots, N; \quad j = 1, 2, \dots, M$$

in which N and M are the number of elements found in the x-row and y-column, respectively. A one-dimensional comparison of  $g(i,j)$  and  $h(i,j)$  is shown in figure 2 (upper).

By using a procedure similar to that used on the smoothed and original point-source matrices, the row of  $g(i,j)$  which passes through or nearest to the gaussian distribution center,  $\bar{x}, \bar{y}$ , is transformed, via a Fourier series analysis, into a spatial-frequency distribution. This distribution, which also happens to be gaussian in shape, is then plotted on the same graph as the frequency distributions of the smoothed and original matrix data (fig. 2 lower). The gaussian spatial-frequency curve thus becomes the criterion against which the other spatial-frequency curves of that point source can be compared. The difference between the spatial-frequency curve and the gaussian curve of each point source is therefore a measure of the ability of each filter to transform the unfiltered frequency components into the gaussian shape. Similarly, the difference between the original spatial-frequency components and the corresponding components of the smoothed data is a measure of the ability of that particular smoothing technique to attenuate the spatial-frequency components of the point-source response.

None of the described smoothing schemes transform exactly the spatial-frequency components of the original data into the best-fit gaussian spatial-frequency components, as figure 2 (lower) illustrates. Since the best-fit gaussian point-source response is our design criteria, we require a set of attenuating terms which will exactly transform the unfiltered spatial-frequency components into the corresponding gaussian components. These attenuating terms are found by dividing the gaussian amplitude components  $A_g(i)$  by the unfiltered amplitude components  $A_f(i)$ , as shown in equation 14.

$$A_h(i) = A_g(i)/A_f(i) \quad i = 0, 1, \dots, N/2 \quad (14)$$

in which  $A_h(i)$  is the resulting spatial-frequency amplitude attenuating function and  $i$  is its frequency index (9). If the only difference between the original and the gaussian curve was the randomness in the signal, then  $A_h(i)$  will minimize those data fluctuations. The filter  $A_h(i)$  can also be used to remove the randomness found in any scintiscan data recorded under scan conditions similar to those used in obtaining the point-source response. To this end, each component of  $A_h(i)$  is used to attenuate the corresponding spatial-frequency component  $A_c(i)$  of the original or recorded scintiscan data. The smoothed spatial-frequency amplitudes,  $A_d(i)$ , for each row of the recorded scintiscan data are found as:

$$A_d(i) = A_c(i) A_h(i) \quad i = 0, 1, 2, \dots, N/2 \quad (15)$$

in which  $A_c(i)$  successively assumes values calculated for each row of the data matrix.

The recovery of the smoothed spatial contour  $D(n,m)$  from  $A_d(i)$  is achieved by finding the individual cosine and sine coefficients,  $a_d(i)$  and  $b_d(i)$  by using equations 16 and 17.

$$a_d(i) = A_d(i) \cos [B_c(i)] \quad (16)$$

$$i = 0, 1, 2, \dots, N/2$$

$$b_d(i) = A_d(i) \sin [B_c(i)] \quad (17)$$

From these modified sine and cosine coefficients, the smoothed data counts  $D(n,m)$  may be calculated from equation 10. Again, this procedure is repeated for the coefficient set  $A_d(i)$  of each row.

It is important to note that the phase correction properties of the smoothing function  $A_h(i)$  are not used in equations 16 and 17 because they pertain only to the spatial locations of the point-source responses and not to the spatial properties of the recorded count matrix  $C(n,m)$ . This means that only  $B_c(i)$  should be used in the computation of  $a_d(i)$  and  $b_d(i)$  by equations 16 and 17.

### III. RESULTS

The spatial-frequency components of the original and of the smoothed point-source responses corresponding to the various isotopes are plotted in figure 3 against their spatial-frequency indices. These plots demonstrate (1) the influence of increasing isotope energy on the scintiscan recording system and (2) the ability of the various smoothing schemes to attenuate the spatial-frequency components of the several different point-



source responses.

In the results illustrated in figure 3, the 1:2:1 weighted-data filter (equation 1) generally produced the least amount of attenuation of the original spatial-frequency components. This effect is attributable to the small number of data points used in the smoothing process. The point-source response (PSR) convolution smoothing scheme (equation 5) conferred the greatest attenuation on the unfiltered spatial-frequency components. This result is attributable both to the large number of weighting elements and to the actual numerical values of the elements. It is interesting that the use of the PSR convolution routine is mathematically equivalent to taking the results of the recorded scintiscan data and passing them through the collimator-detection system a second time. The statistical filtering process produced an attenuation effect somewhere between that found with the 1:2:1 weighted-data and the PSR convolution scheme. The characteristics of the statistical smoothing routine are attributable primarily to the 1:8:1 weighted-data averaging properties inherent in the use of equation 4 rather than to the statistical decision-making process. In particular, if only the decision-making portion of the smoothing routine is used, an undesirable amplification rather than attenuation of the spatial-frequency terms above the 10th harmonic can be demonstrated. The combination of decision-making and data-weighting makes this smoothing process quite useful, however. Finally, the gaussian point-source spatial-frequency characteristics are

located between the unfiltered frequency components and the PSR convolution smoothing components. This suggests that the best-fit gaussian function may define a desirable set of point-source response coefficients.

Figure 4 illustrates the results of using the above smoothing schemes on an unfiltered scintiscan of a thyroid phantom. The thyroid phantom was filled with 30  $\mu\text{Ci}$  of  $^{131}\text{I}$  in solution and was scanned under the identical conditions as used with the isotope point sources. The three-dimensional maps illustrate the minute count variations found before and after the various digital smoothing processes. The gaussian filter criterion used to smooth the thyroid phantom scan matrix was obtained by using the  $^{131}\text{I}$  point-source response shown in figure 1 and equations 6 through 17.

#### IV. DISCUSSION

The application of two-dimensional convolution techniques, such as given in equations 1, 4, 5, for smoothing scintiscan data will produce an attenuation of the spatial-frequency amplitude components of the scintiscan matrix, especially when positive weighting coefficients are used. This is demonstrated in figures 2 and 3 by the reduction in the amplitude values of the smoothed spatial-frequencies. This amplitude attenuation effect means that digital smoothing can never improve the contrast of the existing scintiscan data but, at best, can modify the existing information so that essential information such as "hot spots"

and "cold spots" may be detected more easily. It also means that a corresponding loss in definitions of boundaries between these spots will occur. A filtering technique which appears to yield a minimal loss of boundary definition and also moderate smoothing characteristics has been described elsewhere as a variable-spatial smoothing scheme (5).

The results in figure 2 (upper) demonstrate that one line of the recorded point-source response and its gaussian approximation superimpose quite closely, yet figure 2 (lower) indicates that their spatial-frequency components are remarkably different. This is because the spatial-frequency components of the recorded point-source response data were computed before background subtraction. Due to their random nature, background counts are not a constant bias signal addition to the spatial-frequency curve but tend to modify all the spatial frequencies to some degree. The removal of a bias background count value from the recorded point-source response is merely a trick needed for the calculation of the gaussian curve parameters. If any background variation remains in the original point-source response matrix, it is then averaged during the gaussian parameter calculations. This implies that any difference between the recorded point-source response spatial-frequency components and the gaussian spatial-frequency components can be used as a measure of the spatial-frequency effects attributable to random processes.

The use of equations 14 through 17 allows one to smooth with respect to a known gaussian function whose parameters are derived from the

recording system's own point-source response during a particular set of scintiscanning conditions. The best-fit gaussian point-source response therefore is a mathematical function which is dependent on such factors as the isotope used, the collimator-to-isotope distance, and the medium between the source and detector. Thus, the point-source recording must be made under the identical scan conditions that would be used during an actual scintiscan procedure. Since this exact duplication can never be realized completely, the point-source response matrix values and the subsequent gaussian calculations must always be considered as an approximation to some point-source response existing at the time of the data scan. Our studies on pulmonary scintiscans have shown that the best gaussian point-source response filter approximation is achieved by recording the system's point-source response with the isotope point-source located spatially at the collimator's isoresponse focal point and beneath an appropriate energy-absorbing medium such as water.

Two-dimensional Fourier series analysis indicates that row and column spatial-frequency components may be calculated independently of one another (10). Our data, as shown by figure 4, suggest that one-dimensional Fourier series analysis achieves an adequate filtering scheme, as compared to the attenuating effects found with the other smoothing techniques. If more data smoothing is deemed necessary, additional filtering can be obtained by using spatial-frequency attenuation based on column point-source response and best-fit gaussian criteria.

The use of equations 6 through 17 for scintiscan smoothing requires some prescanning preparation in the form of a prior knowledge of the point-source response characteristics and subsequent gaussian approximation of the recording system. By using the gaussian function as a reference criterion, our studies have shown that the statistical decision-making scheme of Brown (7) provides the most consistent smoothing effects for the isotope energy range 0.063 to 0.515 Mev, the Picker 2102A collimator, and the 3-by 3-inch NaI crystal. This does not mean that this scheme is the best for all possible collimator and isotope combinations, but it has been found to be adequate for the combinations we have tested.

In general, the choice of the smoothing routine to be used with scintiscan data depends heavily on the conditions under which the scan is to be made, and no one filter has been found to be ideal for all collimators and all scan conditions. A library of filters and filtering techniques, each based on a particular collimator's characteristics and scintiscan conditions, appears to be an inevitable consequence whenever optimal data smoothing is required.

## References

1. Coulam, C. M., W. Dunnette, and E. H. Wood. A computer-controlled scintiscanning system and associated computer graphic techniques for study of regional distribution of blood flow. J Nucl Med. (In Press)
2. Tauxe, W. N., D. W. Chaapel, and A. C. Sprau. Contrast enhancement of scanning procedures by high-speed digital computer. J Nucl Med 7:647 (1966).
3. MacIntyre, W. J., and J. H. Christie. A comparison of data averaging of radioisotope scan data by photographic and dimensional computer techniques. Symposium of Medical Radioisotope Scintigraphy. Salzburg, Austria, August 6 to 15, 1968.
4. Atkins, H. L., P. Hauser, P. Richards, and J. S. Robertson. Analysis of the optimum conditions for data display and image perception in photoscanning. Symposium on Medical Radioisotope Scintigraphy. Salzburg, Austria, August 6 to 15, 1968.
5. Iinuma, T. A., T. Nagai, and N. Fukuda. Digital data processing and display in radioisotope imaging. Symposium on Medical Radioisotope Scintigraphy. Salzburg, Austria, August 6 to 15, 1968.
6. Pizer, S. M. Computation and display of scans. In: Handbook of Computer Applications in Radiology, Radiotherapy, and Nuclear Medicine. (In Press )

7. Brown, D. W. Digital computer analysis and display of the radioisotope scan. J Nucl Med 5:802 (1964).
8. Sprau, A. C., W. N. Tauxe, and D. W. Chaapel. A computerized radioisotope-scan-data filter based upon a system response to a point source. Mayo Clin Proc 41:585 (1966).
9. Lee, Y. W. Statistical theory of communication. New York, John Wiley & Sons, Inc., 1961 , 328 pp.
10. Oppenheim, A. V., R. W. Schafer, and T. G. Stockham, Jr. Non-linear filtering of multiplied and convolved signals. Proc IEEE 56:1264 (1968).

### $^{131}\text{I}$ ISOTOPE POINT RESPONSE

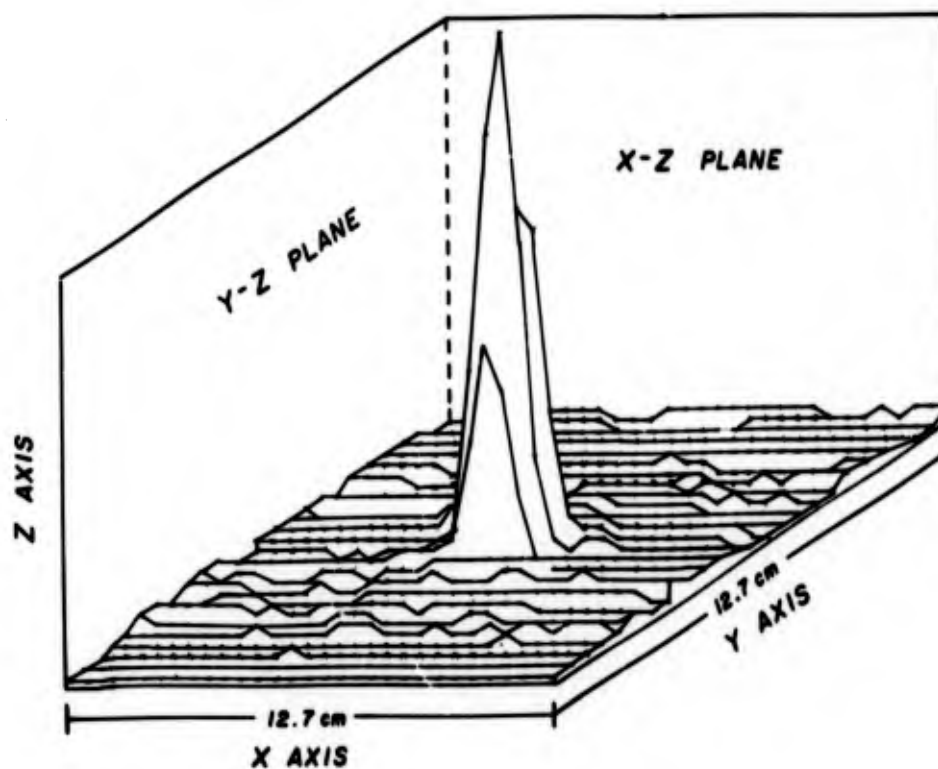


FIGURE 1

Three-dimensional representation of point-source response matrix obtained by scanning 1-mm-diameter point source containing  $20\ \mu\text{Ci}$  of  $^{131}\text{I}$ . Sampling period was 2 seconds at each of 31 by 26 (x,y) locations encompassing a 12.7-by 12.7-cm area. Matrix is displayed as x,y count surface using alphanumeric characters. Lines between consecutive data points were drawn by hand. Distance between any two x-direction points is 0.41 cm and between any two y-direction points, 0.51 cm. Isotope source was located 4 inches from the Picker 2102A collimator face. Source and NaI crystal were separated by air.



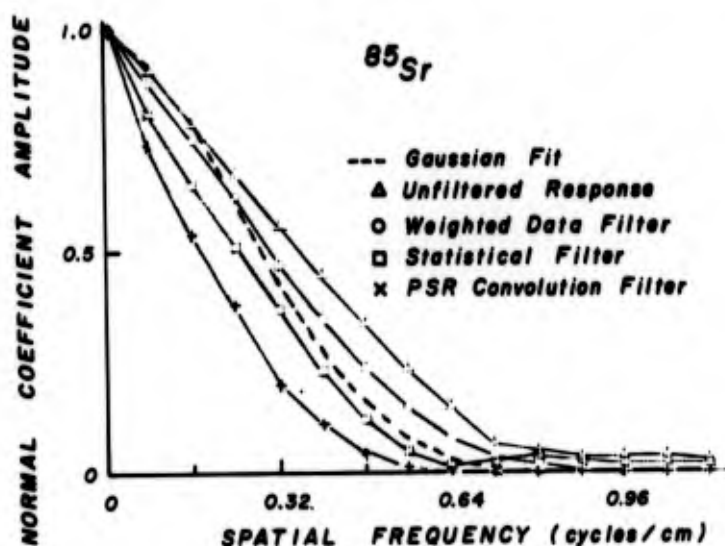
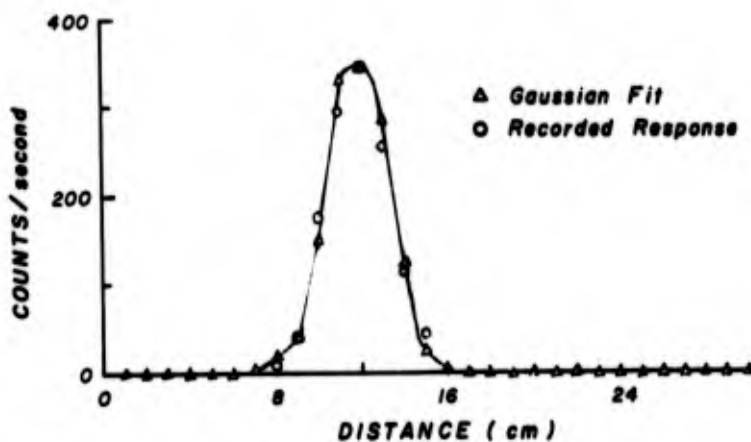


FIGURE 2

Upper,  $^{85}\text{Sr}$  point-source response compared with its best-fit gaussian curve. Lower, spatial-frequency components derived from point-source data of Upper, illustrating unfiltered frequency components, gaussian frequency components, and frequency components after original point-source data had been smoothed by three different methods. Difference between unfiltered and filtered amplitude values is a measure of frequency-attenuating effects of the smoothing scheme.

SMOOTHING EFFECTS ON SPATIAL FREQUENCY CHARACTERISTICS OF ISOTOPE POINT-SOURCE RESPONSES

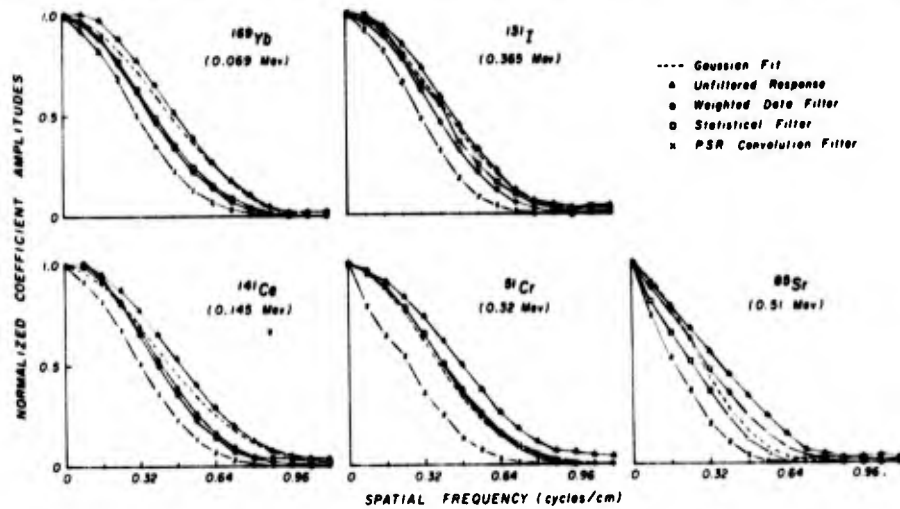


FIGURE 3

Spatial-frequency plots of unfiltered, gaussian, and smoothed point-source responses, demonstrating attenuating effects of different smoothing schemes as a function of energy spectra of different isotopes. Difference between gaussian and unfiltered curves is indication of signal randomness; difference between unfiltered and filtered curves is measure of spatial-frequency attenuating effects of smoothing function.

COMPARISON OF SMOOTHING TECHNIQS  
ON THYROID PHANTOM SCINTISCAN

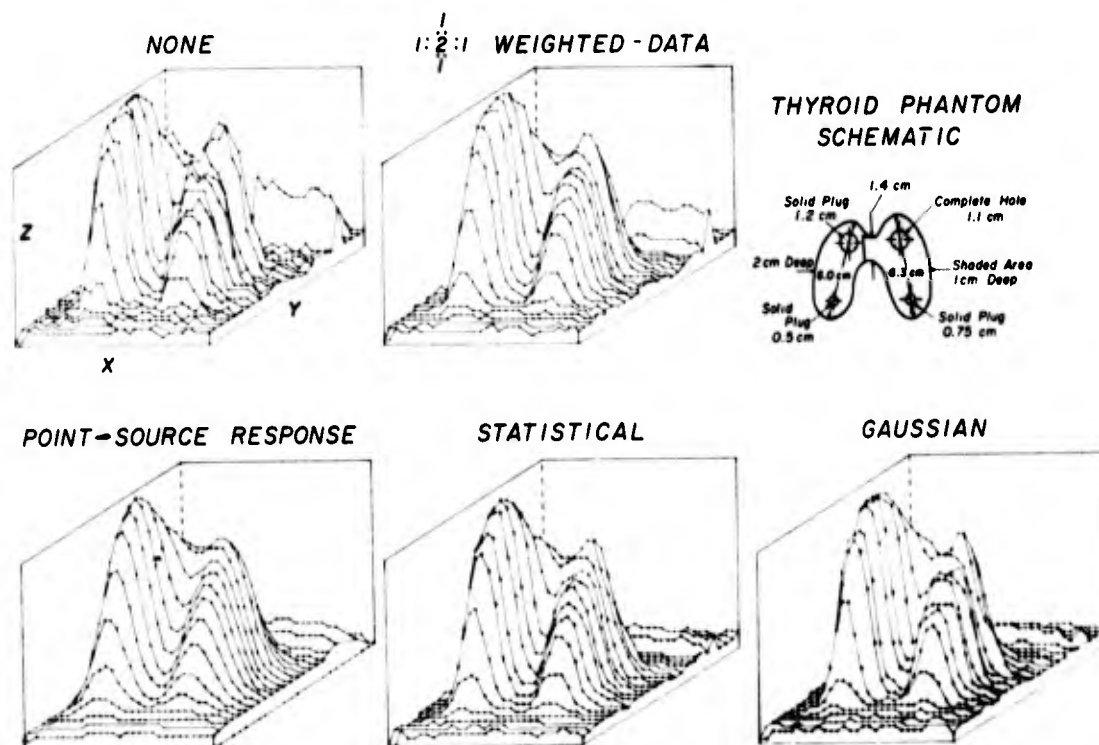


FIGURE 4

Scintiscans of thyroid phantom (diagrammed, Upper Right) which show effects of different schemes of digital computer smoothing algorithms. Upper Left, Unfiltered, originally recorded data. Upper Middle, Effects of 1:2:1 weighted-data filter. Lower Left, PSR convolution smoothing routine. Lower Middle, Statistical decision-making and 1:8:1 smoothing effects. Lower Right, digital-smoothing routine based on gaussian point-source criteria of this paper. Phantom contained 30  $\mu\text{Ci}$  of  $^{131}\text{I}$  and was scanned by taking 2-second counts at each of 31 by 26 (x,y) locations encompassing a 12.7 by 12.7-cm area containing the phantom. Distance between two x-sample positions was 0.41 cm and between two y-sample positions, 0.51 cm. Collimator was 4 inches from source, separated by air.

III. COMPUTER-GENERATED THREE-DIMENSIONAL  
OSCILLOSCOPIC IMAGES

**BLANK PAGE**

## ABSTRACT

A computer-produced oscilloscopic display utilizing three-dimensional surface maps and contour plots in conjunction with images of the shape and volume of the excised lung and its interlobar fissures has been developed for study of the spatial distribution of isotope-tagged  $^{35}\mu$  microsphere emboli in the lung from scintiscan data following their injection into the outflow tract of the right ventricle. Data indicate that the distribution of these emboli in different regions of the lung is proportional to the blood flow to these regions at the time of the injection.

Visualization of the surfaces representing count rates as a function of two spatial coordinates of various planes through the count matrix was achieved by a shading technique which creates the illusion of three dimensions on a photographic image of the display.

Isocount contour maps of transverse sections of excised lungs, obtained following fixation by air-drying while inflated to 30 cm H<sub>2</sub>O, were displayed and their spatial orientations indicated in images of the lungs and their component lobes generated from data fed into the computer by cursor tracing of the external lung borders and its interlobar fissures from each of the one-centimeter slices into which the lungs were sectioned.

**PRECEDING PAGE BLANK**

Determinations of the fractions of cardiac output traversing the two lungs and their component lobes and the rate of perfusion (blood flow per unit volume) of different regions in the lung are calculated from the scan matrix and these anatomical measurements.

If uniform microsphere tagging of the blood is achieved, the sectional contour maps, together with the anatomic data and three-dimensional count surface displays, provide the facility for display and study of complete information concerning the spatial distribution of pulmonary blood flow at the time of injection of the microspheres.

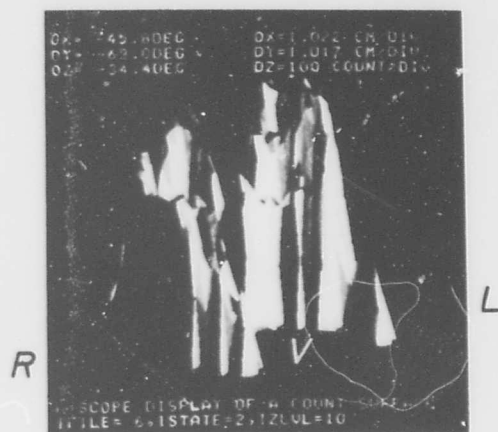


FIGURE 1

Picture of computer-generated cathode-ray tube display of the distribution of radioactivity (blood flow) in a one-centimeter-thick transverse section of the lungs of a dog. An injection of 35-micron-diameter microsphere emboli tagged with  $^{141}\text{Ce}$  was made into the right ventricular out-flow tract after the dog had been in the left lateral position under morphine-pentobarbital anesthesia for a period of 70 minutes. A lethal dose of sodium pentobarbital was given subsequent to the injection; the lungs were removed, air-dried for three days while inflated to 30 centimeters of water, and then immersed in a rectangular container containing urethane foam. After solidification, the entire urethane block containing the lungs was cut into one-centimeter-thick slices. The X and Y coordinates of successive points outlining the external borders of the lung and the interlobar fissures were recorded on magnetic tape by manual tracing with an electronic cursor of these borders and fissures on both surfaces of each member of the set of one-centimeter-thick sections comprising the entire lung. Computer-controlled



scintiscan of the surface of each lung section was then carried out by sampling for periods of 3 seconds at each of a rectangular matrix of points 1.0 cm apart and covering the surface of the section.

This particular display is from the 10th section cephalad from the most caudad margin (costophrenic angle) of the lungs. The illusion of three-dimensions is achieved by: (1) filling in the surfaces between data points, (2) shading each surface section relative to its theoretical reflection of light from a source of illumination to the left of the display, and (3) ignoring the data points which should be hidden by the foreground surfaces included in this particular display.

The computer printed legends 'OX, OY, OZ' indicate the degree of tilt of the orthogonal axes in relation to the raster of the cathode-ray tube; 'DX, DY, DZ' define the magnitude of the calibration marks on the respective X, Y, and Z axes; 'IFile' defines the individual animal from whom the data were obtained; 'I State', the isotope used; and, 'IZLVL', the number of the particular section from which the displayed data were obtained. R, L, and V indicate the right, left, and ventral borders of the lung section, respectively, the dorsal border being hidden from view in this display.

Note that the highest count values were recorded over the left portion of the lungs, which was on the dependent side of the animal when the isotope injection was made.

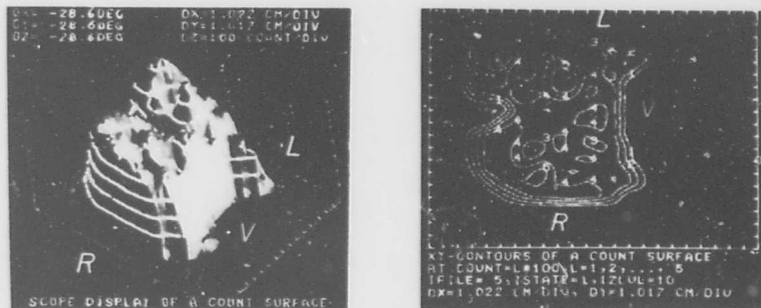


FIGURE 2

Pictures of computer-generated cathode-ray tube displays of distribution of radioactive microsphere emboli in a one-centimeter-thick cross-section of a dog lung. The microspheres (diameter:  $35\mu$ ) were injected into the right ventricular outflow tract 5 seconds after rolling the dog from the left to the right side when under morphine-pentobarbital anesthesia.

The X and Y axes in both panels are the spatial coordinates of the cephalad surface of this lung section. The count rates (radioactivity) recorded over this surface are displayed on the Z axis for the three-dimensional representation (left panel) upon which brightened lines have been superimposed to delineate increments of 100 counts per second. The numerals 1 to 5 identify the contour lines in the right panel, which are plotted at increments of 100 counts per second. Additional details are included in the legend of figure 1.

Note that relatively little change in the distribution of blood flow to the right and left lungs occurred during the 5-second period following the change from the left to the right lateral position which reverses the superior and dependent relationship of the two lungs in relation to their vertical height in the thorax.

*(Based on Input from Cursor Outlining of 1-cm Sections of  
Lungs Embedded En Bloc in Urethane Foam)*

VENTRAL SURFACES

DORSAL SURFACES

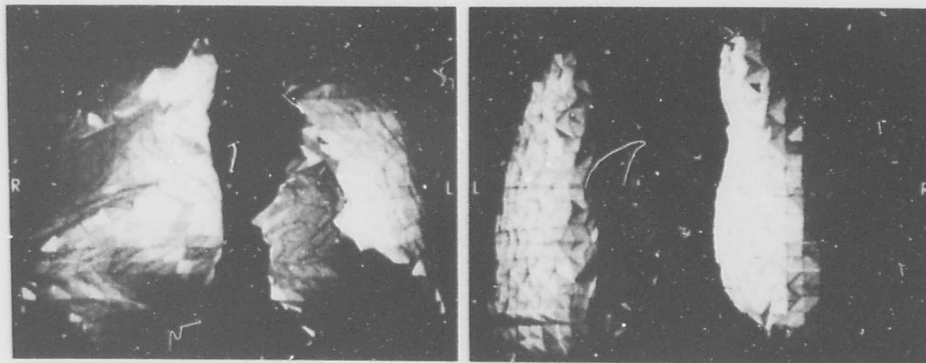


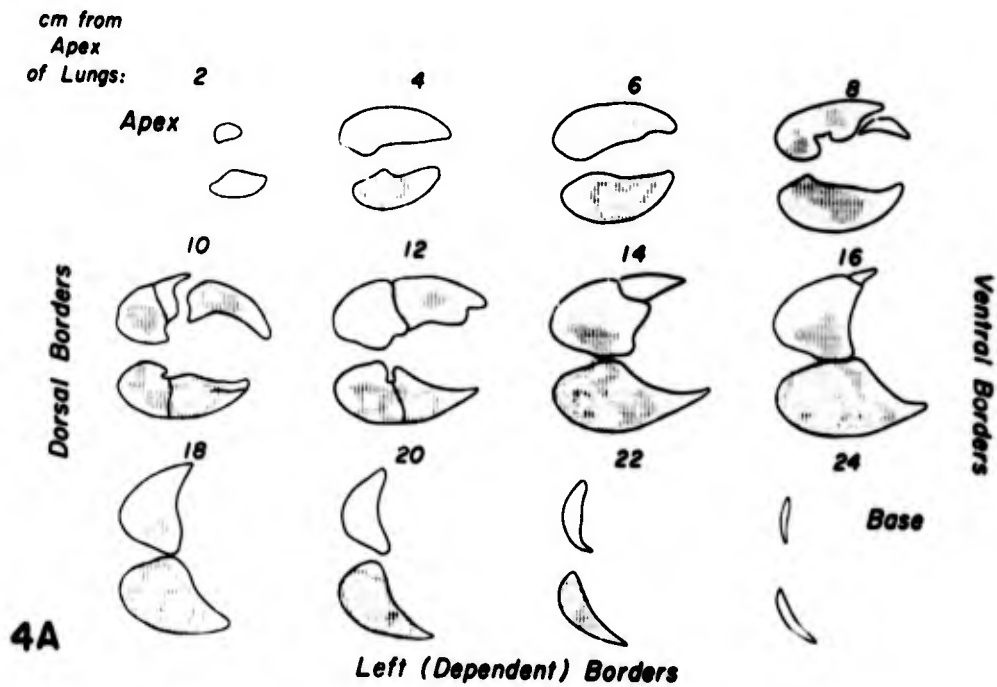
FIGURE 3

Pictures of computer-generated oscilloscopic three-dimensional simulation of the ventral and dorsal surfaces of a chimpanzee lung (Chimpanzee F, Section IV of this report).

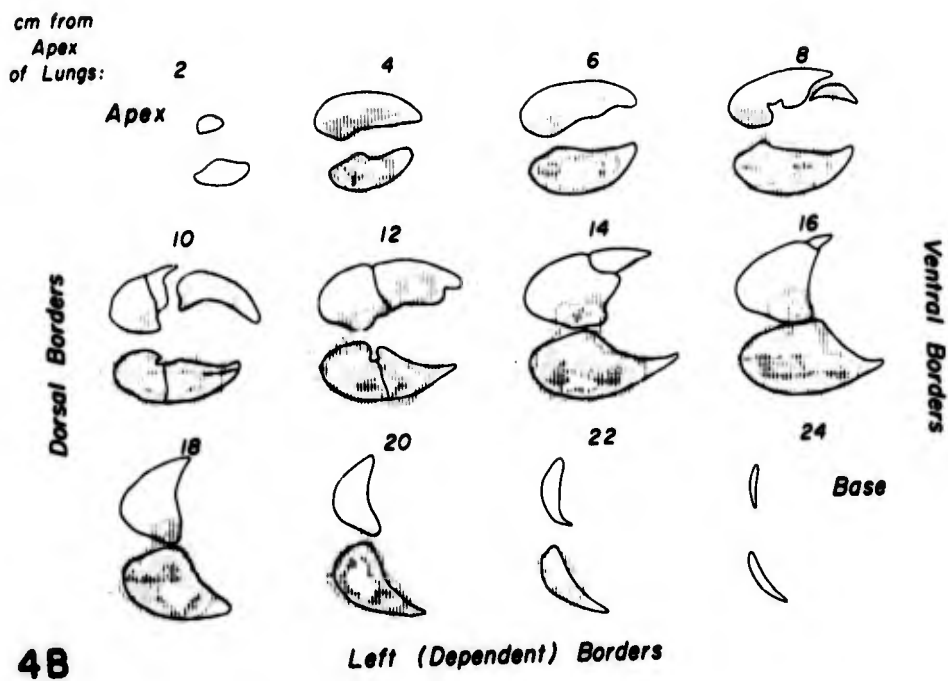
The procedure used to feed the data into the computer from which these displays were generated is outlined in the legend of figure 1.

**FIGURE 4**

Computer-generated contour plots of distribution of radioactive microspheres (blood flow) in 2-centimeter-thick transverse sections of the chimpanzee lungs shown in figure 3.



A) Distribution of microspheres tagged with  $^{141}\text{Ce}$  injected into the right ventricular outflow tract while the chimpanzee was in the left lateral position at 1Gy under Sernylan-sodium pentobarbital anesthesia.



B) Distribution of microspheres tagged with  $^{85}\text{Sr}$  injected into the right ventricle about 15 minutes later, 50 seconds after the onset of an exposure to 5.8Gy in the left lateral position. The gamma radiations originating from the two isotopes were distinguished by pulse-height analysis. Note the displacement of the microspheres toward the dependent borders of both lungs which occurred during the exposure to 5.8Gy. This effect can be seen more clearly in the closeup of the scintiscan results obtained from the cross-section located 12 centimeters from the apex of the lungs shown in figure 5.

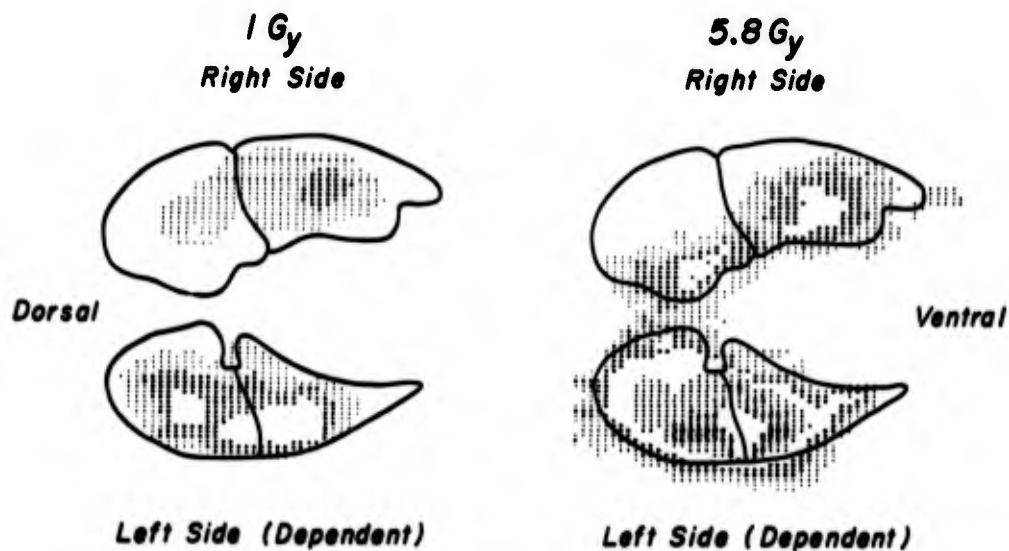


FIGURE 5

Computer-printed contour plots of distribution of microspheres (blood flow) in transverse section 12 centimeters from the apex of the chimpanzee lungs shown in figures 3 and 4.

The hierarchy of computer-printed symbols used to designate successive count levels is as follows: blank (background level), -, A, blank, +, B, blank, C, blank, etc. The symbol - designates the first increment of count level above background; A, the second increment; blank, the third increment; etc.

The increment in count levels for the  $^{141}\text{Ce}$ -tagged microspheres used at 1Gy was 6 counts per second, and for the  $^{85}\text{Sr}$  microspheres used at 5.8Gy, 4 counts per second.

Note the higher level of radiation (blood flow) in the dependent lung at 1Gy and the displacement of blood flow toward the dependent borders of both lungs during the exposure to 5.8Gy.

IV. APPLICATION OF TECHNIQUES TO THE STUDY OF  
EFFECTS OF  $\pm G_y$  ACCELERATION ON PULMONARY BLOOD FLOW  
IN CHIMPANZEES

PRECEDING PAGE BLANK

## ABSTRACT

The effect of changes in the direction and magnitude of the gravitational-inertial force environment on the regional distribution of impacted 35 $\mu$ -diameter microspheres has been measured in the lungs of six anesthetized chimpanzees. The distributions were determined by two computer-controlled scintiscans at 780 sites covering the dorsal and ventral surfaces of the thorax of animals supported in the right (-G<sub>y</sub>) and left (+G<sub>y</sub>) lateral positions by individually fitted half-body casts. The measurements were made at 1 G subsequent to four injections of differentially isotope-tagged microspheres into the right ventricular outflow tract while the animals were at 1 and 5.8 G. Pulse-height analysis at each site allowed separation of count values for the individual isotopes. Following correction for collimator distortion, these values were assumed to be proportional to the respective blood flows which were present below each site at the respective time of injections of each isotope. Supportive physiologic data included continuously recorded oxygen saturation of arterial and mixed venous blood, intrathoracic vascular and intrapleural pressures, and biplane roentgenograms of the thorax. Computer-generated 3-dimensional and contour map displays of the scintiscan and related data indicate that during exposures to accelerations of 5.8 Gy pulmonary blood flow tended to redistribute toward the midthoracic region concomitantly with large decreases in arterial oxygen saturation presumably resulting from pulmonary arterial-venous shunts via the dependent regions of the lung. The decrease in blood flow to the superior (lateral) regions of the upper lung was predictably acceleration-

**PRECEDING PAGE BLANK**



dependent. However, the finding of no change or decreases in flow to the lateral (dependent) region of the lower lung, in spite of large increases in intravascular pressures, suggests that selective increases in resistance to blood flow to the dependent, presumably anoxic, region of the lung occurred--increases which were responsible for the reduction in level of the physiologic shunt frequently observed in these animals toward the end of the 60 to 70 seconds of exposure to 5.8 Gy.

## I. INTRODUCTION

Numerous experiments over the past fifteen years have demonstrated that capillary blood flow is not uniform in all parts of the lung, and that the relative distribution of blood flow is determined primarily by gravitational and inertial forces. The influence of gravity is such that in the normal upright man, blood flow at the base of the lung is approximately ten times greater than at the apex, but in the supine man, regional variations are greatly reduced (27). Regional variations are exaggerated during exposure to an increased-force environment generated by a human centrifuge (5), and presumably only minimal variations would be found in the zero-G environment. The peculiar sensitivity of the lung to the direction and magnitude of the gravitational-inertial force environment is a result of the large differences in specific weight of blood and gases on opposite sides of the alveolar membrane, the relative low blood pressure available for maintaining blood flow to upper regions of the lungs, and the relative fragility of the pulmonary parenchyma.

Regional variations in blood flow were not demonstrated until radioactive gas techniques had been developed, although indirect evidence suggested that regional gravity-dependent variations in flow did exist. Of the several methods, the xenon-133 technique, described in 1962 by Ball et al. (2), has been used most often, and almost all information about regional variations has been derived from application of this technique. However, radioactive gas methods are frequently not suitable for acceleration studies because all of the external scintillation scanning or counting

must be performed during the acceleration exposure, and within the brief breath-holding period before the gas is exhaled.

These limitations do not apply to the radioactive embolization techniques. The best known of these is the macroaggregated serum albumin technique described by Wagner et al. (25) in 1964. Labeled albumin particles are injected into the right ventricular outflow tract, and because of their size, lodge in the pulmonary capillary bed. Their pattern of distribution is assumed to be representative of the pattern of capillary blood flow at the time of injection. The chief advantages of this technique for acceleration studies are: 1) the particles can be injected during the acceleration exposure, and the lung scanning performed afterwards in the conventional manner; 2) the distribution of emboli can be more accurately determined than the distribution of alveolar xenon 133 because scanning time is not a limiting factor; and 3) the distribution of emboli can be confirmed by direct observation in sections of the resected lung at necropsy. However, the embolization methods do present problems in data handling. Slow, point-by-point scanning is required for maximum accuracy, and a computer facility for data storage, processing, and display is necessary for optimum use of the technique.

Reed (18), in our laboratory, has further refined the embolization method for studies in animals during acceleration on the human centrifuge. Radioactive carbonized microspheres are substituted for albumin particles because microspheres of closely controlled diameters

are commercially available and can be tagged with a variety of radioactive isotopes. Using microspheres labeled with different isotopes, multiple injections can be made in a single animal and the distribution of emboli from each injection determined on the basis of differences in their spectral energies.

The purpose of the present investigation was to determine the effects of transverse ( $G_y^*$ ) acceleration on regional pulmonary blood flow in chimpanzees by use of the radioactive microsphere technique, and to relate these changes to concomitant effects on regional differences in pleural, intrapulmonary, and systemic vascular pressures; roentgenographic appearance of the lungs; oxygen saturation of mixed venous and systemic arterial blood; and the magnitude of the associated physiologic pulmonary arterial-venous shunts. Four injections of microspheres were made into the right ventricular outflow tract, each with a different isotope, during exposure to a different direction or magnitude of the force environment; viz,  $+1 G_y$ ,  $+5.8 G_y$ ,  $-1 G_y$ , and  $-5.8 G_y$ . The regional distribution of the microsphere emboli in the lungs was assumed to be proportional to the regional distribution of pulmonary blood flow at the time of their injection and was determined by external scintiscanning of the animal's thorax. The scintiscan count data were processed by digital computer, and the results displayed using computer-generated three-dimensional surface maps, contour maps, and summation-to-transverse

---

\*  $+G_y$  acceleration produces inertial displacements of viscera to the left;  
 $-G_y$  acceleration to the right.

plane plots. Arterial and venous-blood oxygen saturations, intrathoracic vascular and intrapleural pressures, cardiac output, and anterior-posterior (A-P) and lateral roentgenograms were obtained as supportive physiologic information. These supportive data were also obtained during exposure to accelerations of  $\pm 2.9$  G. Anesthetized chimpanzees were used because the dimensions and shape of their lungs and thoraces are closely similar to those of humans. It is not unlikely, therefore, that the physical effects of acceleration on the thoracic contents may be similar in these two species.

## II. METHODS

### Initial Preparations

Six adult chimpanzees, 39- to 57-kg body mass, were anesthetized with Sernylan<sup>+</sup> (1 mg/kg i.m.) and intubated with a cuffed endotracheal tube. Anesthesia was maintained using morphine sulphate (10-15 mg s.c.) and sodium pentobarbital (60-120 mg i.v.) as necessary for the duration of the experiment. An indwelling urethral catheter was placed in the bladder and allowed to drain continuously. All animals had been subjected to similar centrifuge experiments in this laboratory involving right heart, arterial and pleural catheterization, and multiple exposures to  $G_x$  accelerations ranging from -6 to +6 G (approximately one year earlier). Additional information on the animals is given in table I.

Radiopaque catheters were introduced percutaneously into the vascular system using aseptic techniques and positioned under fluoro-

---

<sup>+</sup>Phencyclidine hydrochloride, Parke, Davis and Co.

TABLE I

VITAL STATISTICS

Animal	Sex	Weight (kg)	Internal Dimensions of Thorax (cm)*		Cardiac Output (l/min)	Central Blood Volume (liters)	Hemoglobin (gm/100 ml)
			Transv.	A-P			
A	M	39	22	20.5	2.39	0.34	15.9
B	M	57	24.2	21.5	---	---	15.8
C	F	46	22	22	4.13	---	15.3
D	M	51.5	24.5	21.5	---	---	---
E	M	52	22	21	3.1	0.53	15.3
F	F	39	23.2	20.2	5.1	0.67	16.6

\*Measured at midheart level from biplane roentgenograms corrected for divergent character of x-ray beam.

scopic control. Goodale-Lubin catheters\* (size 6-F, length 80-100 cm) were introduced into the main pulmonary artery (PA) and right ventricular outflow tract (RVOT) via an accessible upper limb vein. A size 8, 100- or 120-cm Odman catheter\* with a bird's-eye tip was introduced into the left atrium (LA) by transseptal puncture from the right femoral vein. These catheters were used for pressure recordings. A 6-F 80- or 100-cm Rodriguez catheter\* was introduced into the RVOT in a similar manner for the purpose of indocyanine green dye and radioactive microsphere injections.

A short (40-cm) 7-F open-tipped catheter or short length of similar diameter polyethylene tubing was secured in an arm vein for the continuous reinfusion of blood withdrawn during oxygen-saturation and dye-dilution curve measurements.

Catheters were introduced similarly into both femoral arteries. One, a 5-F, 80- or 100-cm Goodale-Lubin catheter was positioned with its tip in the thoracic aorta at the level of the tricuspid valve for recording central arterial pressure. The tip of the second, a 6-F, 20-cm Teflon or polyethylene catheter, was positioned in the abdominal aorta near the bifurcation for sampling blood for oximetry and dye dilution curves.

Radiopaque polyethylene catheters\*\* (i.d. 0.7 mm., o.d. 1.3 mm) were inserted percutaneously into the right and left potential pleural

---

\*United States Catheter and Instrument Corp., Glens Falls, New York.

\*\*Electro-cath. Corp., Linden, New Jersey.

spaces at the level of the fourth or fifth interspace, anteriorly. This technique has been described previously (30). Care was taken to avoid the introduction of air during the procedure. The catheter tips were positioned with the aid of the fluoroscope at the extreme right and left lateral borders of the lungs. At the time of insertion of the catheters, and periodically thereafter, the catheters were aspirated to detect and remove pleural fluid or air collecting at the tip. In every animal, up to 5 ml of pink fluid could be withdrawn from the most dependent catheter on more than one occasion during the experiment. No air was detected in the pleural cavity by this technique.

A bird's-eye tip, radiopaque, size 8 Odman catheter was placed in the esophagus, with its tip at about midthoracic level, for pressure measurement and to remove secretions. In some animals it was advanced temporarily into the stomach so that excessive accumulation of air could be aspirated.

All catheters were filled with Ringer's solution, containing 10 mg of heparin per liter. Their locations are shown in the A-P roentgenogram of figure 1.

After all catheters had been positioned and secured, the animal was placed in a molded fiber-glass, half-body cast\* (prepared previously for each animal) in either the right or left lateral position. The cast was then placed in the centrifuge cockpit and its position carefully adjusted so that midlung level in both coronal and

---

\*Manufactured by Air Force personnel at Brooks AFB, Texas.



sagittal planes determined by biplane thoracic roentgenograms coincided with the axis of tilt of the cockpit. This adjustment was accomplished by matching the intersection of these planes with cross-hairs placed on lateral and A-P thoracic roentgenograms so that they marked the levels of the respective cockpit planes intersecting its axis of rotation. As the centrifuge rotated, the cockpit and animal tilted about their common axis so that the resultant of the gravitational and inertial forces was perpendicular to the floor of the cockpit and directed from side to side ( $+G_y$ ) with respect to the animal.

#### Blood-Flow Measurement Techniques

Regional pulmonary blood-flow distribution was determined by injecting radioactive carbonized microspheres ( $35 \pm 5 \mu$ ; specific gravity 1.4)\*\* into the RVOT during centrifuge runs, followed by external scanning of the thorax after all runs were completed. The microspheres were initially prepared using a Tween 80<sup>†</sup> washing technique (17,18), suspended in 1 ml of saline, and later transferred into a length of polyethylene tubing interposed between the RVOT catheter and a saline-loaded pressure injector syringe. The injection time was less than 2 seconds in all cases. The Tween 80 washing procedure was used to minimize the inherent aggregating tendency of the microspheres. Previous investigations in this laboratory with dogs suggest that the distribution of the microspheres which embolize in the lung is representative of the distribution of pulmonary blood flow at the time of the injection (17,18).

Four isotope labels were used. As the energy of each isotope

---

\*\*Manufactured by 3 M company, St. Paul, Minnesota.

†Polyoxyethylene (20) sorbitan mono-oleate.

was sufficiently different from the others, the thoracic distribution of each could be determined independent of the others present. Thus, four injections were possible in each animal, and one injection was made when the animal was being exposed to different force environments; viz, +1 Gy, +5.8 Gy, -1 Gy, -5.8 Gy.

The isotopes injected were  $^{169}\text{Yb}$ ,  $^{141}\text{Ce}$ ,  $^{51}\text{Cr}$ , and  $^{85}\text{Sr}$ . The specific activity of each varied, but the number of microspheres injected was adjusted to produce the same counting rate in each channel. The activity in each injection was approximately 0.5-0.1 mCi  $^{169}\text{Yb}$ , 2-3 mCi  $^{141}\text{Ce}$ , 8-10 mCi  $^{51}\text{Cr}$ , and 1 mCi  $^{85}\text{Sr}$ . Table II shows the window settings of the pulse-height analyzer for each isotope channel, and the fraction of energy of any one isotope appearing in each of the four channels when the individual isotopes were placed beneath the energy detection-head assembly. The transpose of this channel "spillover" matrix was then used in the solution of a set of four simultaneous equations to obtain the actual count rate for each isotope in its channel, independent of the energy contribution from the others.

The spatial distribution of each of the four isotopes was found by externally scanning the dorsal and ventral surfaces of the thorax using a specially modified, computer-controlled Picker Magna V scintiscanner, a 2102 A Picker collimator (medium focus, 100% isoresponse in air, 3 inches from the collimator face), and a 3-x 3-inch thallium-activated sodium iodide crystal. Both the ventral and dorsal surfaces

TABLE II  
ENERGY FRACTION MATRIX

		SPECTROMETER CHANNELS			
		$^{169}\text{Yb}$ 63 KeV (40-70)	$^{141}\text{Ce}$ 145 KeV (110-150)	$^{51}\text{Cr}$ 322 KeV (280-340)	$^{85}\text{Sr}$ 515 KeV (480-620)
Window Settings:		(40-70)	(110-150)	(280-340)	(480-620)
ISOTOPE	$^{169}\text{Yb}$	1.00	0.17	0.03	0.00
	$^{141}\text{Ce}$	0.11	1.00	0.00	0.00
	$^{51}\text{Cr}$	0.10	0.21	1.00	0.00
	$^{85}\text{Sr}$	0.13	0.18	0.15	1.00

of the animal's thorax were scanned while the animal was anesthetized, and supported in the supine and prone positions, respectively, by means of molded fiber-glass half-body casts. Each scintiscan consisted of a series of timed counts obtained sequentially as the scanner probe moved sequentially to 780 discrete locations. These sampling locations were the intersections of 26 rows and 30 columns on a 26-cm-square grid. Approximately two hours were required to complete each scan.

Two-to three-second counts were recorded at each location, stored on digital tape, and later processed by computer for smoothing and removal of collimation distortion effects (9). The data were then displayed as four, three-dimensional surface maps, two summation-to-transverse plane maps, and two isocount contour maps, one having ten and the other fifteen stratification levels (fig. 2). The four three-dimensional maps each depict the data as viewed from a different quadrant; the summation-to-transverse plane maps indicate the sum of count values at each transverse (Y) coordinate and sagittal (X) coordinate of the count matrix as viewed from the dorsal, ventral, and cephalocaudad directions, respectively, relative to the orientation of the count matrix in respect to the animal's thorax. The computer was programmed to detect the right and left lung boundaries by the change in count levels which occurred at roentgenographically designated border points. The ratio of total counts recorded over each lung, divided by the total counts recorded over both lungs, was computed and equated with the fraction of cardiac output perfusing each

lung. These computed fractions are referred to as "flow fractions" hereafter. Details of the digital computer techniques used for scanning, boundary definition, smoothing, and removal of collimation distortion have been described elsewhere (8,9).

The last of the six animals studied was killed the day after the scanning procedure due to development of a large retroperitoneal hematoma via a puncture hole in the posterior wall of the right femoral vein produced inadvertently during puncture of this vein with a 16-gauge needle in preparation for transseptal catheterization of the left atrium. This animal's death provided an opportunity to judge how closely the external scan data obtained during life compared with the scan of the resected lungs. The lungs of the animal were removed en bloc, inflated by constant airway pressure of 30 cm of water, and allowed to dry in room air, at room temperature. After drying for several days, the lungs were measured, photographed, and then embedded in polyurethane foam to give the lungs structural support during the subsequent sectioning procedure (17,18).

The anterior (ventral) and posterior (dorsal) surfaces of the rectangular block of polyurethane foam containing the embedded lungs were scanned, corresponding to the scans of the ventral and dorsal surfaces of the thorax of the living animal. The polyurethane block was then sectioned transversely into 24, 1-cm-thick slices. Twelve scans were obtained from the cephalad and caudad surfaces of these sections

by scintiscanning two slices at a time in order to ensure adequate count levels. Radioautographs made from the surfaces of several of these slices showed that only trace amounts of radioactivity had been dislodged during the sectioning process. The coordinates of the cross-sectional borders of each lung section and the interlobar fissures were entered into the computer and the total counts falling within these cross-sectional boundaries were computed for each section. This total count per lung section was then compared with the total count per lung section computed at corresponding anatomical levels from the in vivo scans as well as the scintiscans of the embedded lung prior to sectioning. The flow fractions per lung from the embedded lungs were computed and compared with the flow fractions per lung computed from the cross-sectional scintiscan data.

#### Other Measurements

All strain gauges were mounted in the cockpit at approximately the level of the axis of rotation. This level coincided with the animal's midlung level at 1G and was the zero pressure reference for all pressure calibrations. Intravascular, pleural, and esophageal catheters were connected to Statham P23d strain gauges. Airway pressure was recorded at the oral end of the endotracheal tube with a Statham P5-0.2 strain gauge, and airway flow with a Fleisch No. 1 pneumotachograph and Statham Pm5  $\pm 0.5$  differential strain gauge.

When subjected to an accelerative environment, the body position

of the animal, in spite of being supported by a custom-made fiber-glass half-body cast, shifts slightly relative to the zero pressure level; the positions of the catheter tips change and baselines of the manometers also shift. Methods have been described previously for correcting pressures for effects of acceleration using a saline-filled "thistle tube" system and x-ray measurements of catheter-tip locations (24,30). Both lateral and A-P roentgenograms were obtained during a number of the centrifuge runs for this purpose.

Oxygen saturation was measured continuously in blood sampled from the RVOT, LA, and abdominal aorta using cuvette oximetry (32). The blood was withdrawn and reinfused continuously by roller pumps interposed between the cuvettes and the reinfusion catheter. The cuvettes were calibrated against Van Slyke determinations of oxygen content and capacity of blood samples withdrawn from these sites via all three cuvettes connected in tandem. Real-time, on-line analysis of oxygen saturation by a CDC 3200 digital computer (fig. 3) was important for determining the duration of some centrifuge runs, as will be explained later. This computer method has been described elsewhere (24).

Cardiac output was measured using the indicator dilution technique. A three-point computer calibration curve was established using three aliquots of systemic arterial blood containing no dye, 6.25, and 12.5 mg/L of indocyanine green, respectively. These samples were drawn through a Water's X-C 100 linear densitometer by a roller pump and then reinfused. Cardiac output was computed on-line by the CDC 3200 according to the method

of Williams (29). Mean central blood volume was also computed on-line using the method of Dow (10).

In the first three animals studied, Renovist\* was injected into the RVOT by a pneumatically driven syringe in an attempt to measure regional pulmonary perfusion using roentgen videodensitometric techniques developed in this laboratory (31). However, currently unsolved technical difficulties due to precession of the video image with rotation of the centrifuge through the earth's magnetic field prevented successful use of this technique.

Pressures from all catheters; the oxygen saturations of femoral arterial, pulmonary arterial, and left atrial blood dye curves; revolutions per minute of centrifuge; acceleration at midlung level; angle of tilt of the cockpit; ECG; respirations; and position of the plungers of the injection syringes were recorded on a photokymographic assembly. This assembly consists of two cameras with paper widths of 44.5 and 30.5 cm and speeds of 0.5 and 2.5 cm/sec., respectively. Fourteen channels of these data were recorded in parallel on an Ampex FR 1200 magnetic tape recorder. Simultaneous events on the photokymographic and tape recordings were identified by binary coded decimal signals recorded simultaneously on the two assemblies (Fig. 4).

In addition to the analog recordings, the pleural, esophageal, aortic, pulmonary artery, and airway pressures plus the revolutions of the centrifuge were digitized in real-time, displayed, and also recorded

---

\*Sodium diatrizoate 35%, meglumine diatrizoate 34.3% (Squibb).



on digital tape during the experiment for on-line as well as retrospective analysis using a computer program developed by Dr. A. C. Nolan and Mr. Willis Van Norman in our laboratory. With this program, the averages of a number of pressures were computed for consecutive ten-second periods, and the results printed out with a time code for synchronization with the analog recordings. Figure 5 illustrates a computer printout from a ten-second period during one of the centrifuge runs. The pleural, aortic, and pulmonary artery pressures measured from the photokymographic tracings for the last three animals studied were verified by the computer.

A separate computer program was used to generate analog tapes with all the catheter-tip and baseline corrections applied. Figure 6 is a comparison of the original photokymograph record with one produced by playback of the computer-generated analog tape. Fourth-order Bessel filters in each playback channel reduced the magnitude of vibrational artifacts in the illustrated tracings. Unlike the original recordings, the calibrated and corrected pressures during periods of centrifuge rotation as well as at 1G can be read directly from the computer-processed tracings, thus greatly simplifying data reduction. Comparison of these computer-generated continuous photokymographic recordings of the processed data throughout each centrifuge exposure with the original continuous photokymographic recordings obtained during each exposure provided an invaluable check on the validity of the complete analog-to-

digital computer computation and digital-to-analog data processing and computing assembly.

### Procedure

The chimpanzees were placed on either their right (-G<sub>y</sub>) or left side (+G<sub>y</sub>) supported in the respective half-body cast molded from fiberglass using a plaster of paris form of each animal's body. A series of centrifuge exposures to acceleration were then carried out. All but the first animal were transferred to the opposite lateral cast for a similar series of exposures. The animals were then removed from the cockpit and the ventral surface of the thorax scanned with the animal supported in a half-body cast in the supine position. The animal was then placed in the prone position in a second half-body cast and a scintiscan of the dorsal surface of the thorax carried out.

The exposures to acceleration usually lasted 60 to 90 seconds at the plateau levels of 2.9G and 5.8G in both body positions. The temporal characteristics of the average exposure to acceleration are given in the Appendix and table XI. Control tracings with pressure calibrations were recorded at 1G before and after each run. Upon reaching the acceleration plateau, the zero shift for each gauge was recorded by connecting all gauges by means of remotely controlled hydraulically activated valves simultaneously to the thistle-tube system, the menisci of which had been adjusted to midlung level (fig. 20). Relative gauge sensitivities were checked similarly by simultaneously connecting all gauges to a known pressure. Either a lateral or A-P thoracic roentgenogram was obtained at 1G before most

runs as well as during each period of centrifuge rotation. The centrifuge was stationary during the control determinations at 1G; these procedures, however, duplicated in all other respects those used during the actual exposures to centipetal acceleration.

The observations made during the individual 60- to 90-second exposures to acceleration depended on the protocol (table III). Radioactive microspheres were injected during four separate runs in all but the first animal (in which only two injections were made) at  $-1 G_y$  and  $-5.8 G_y$ . Oxygen saturation was recorded in blood sampled from the main pulmonary artery, abdominal aorta, and when possible, from the left atrium. In some experiments this was done with the animals breathing room air, either spontaneously or on intermittent positive pressure respiration (IPPB). In other experiments, oxygen saturation was recorded at 1 and  $5.8 G_y$  with the animals breathing 99.6% oxygen for ten minutes before, and during, the centrifuge run. Cardiac output was obtained during centrifuge runs in only two animals. Renovist was injected at 1, 2.9, and  $5.8 G_y$  in the first three animals studied in attempts to perform roentgen videodensitometric evaluation of pulmonary blood flow. IPPB was used throughout these runs so that the respiration could be suspended when necessary. Table III shows the various experiments performed, the number of animals used in each, and some of the experimental conditions.

The number of centrifuge runs and the observations carried

TABLE III

SUMMARY OF EXPERIMENTAL PROCEDURES

Experiment	Animal A - 30 Oct. 1968					
	+G <sub>y</sub>			-G <sub>y</sub>		
	1	2.9	5.8	1	2.9	5.8
Blood oxygen saturations breathing air				1+ 1430*	2 AP# 1500	3 AP 1545
Blood oxygen saturations breathing 100% O <sub>2</sub>						4 Lat 1615
Microspheres alone						
Microspheres and green dye				7* Yb <sup>6</sup> 1845		8 *Ce AP 1915
Microspheres and blood oxygen saturations						
Green dye alone				5, 6* AP 1815		
Renovist alone						
Renovist and green dye				9, 10* 1930	11* 1950	12, 13* 2000
X-ray alone						

TABLE III (contd.)

Experiment	Animal B - 3 Dec. 1968					
	+G <sub>y</sub>			-G <sub>y</sub>		
	1	2.9	5.8	1	2.9	5.8
Blood oxygen saturations breathing air				1 1330	2 AP 1350	3 AP 1400
Blood oxygen saturations breathing 100% O <sub>2</sub>				4 AP 1428		
Microspheres alone	9* Sr <sup>90</sup> 2100		10 *Cr AP 2110	5* Yb 1710		6 *Ce AP 1720
Microspheres and green dye						
Microspheres and blood oxygen saturations						
Green dye alone						
Renovist alone				7, 8* 1810		
Renovist and green dye						
X-ray alone			11* Lat 2120			

TABLE III (contd.)

Experiment	Animal C - 11 Feb. 1969					
	+G <sub>y</sub>			-G <sub>y</sub>		
	1	2.9	5.8	1	2.9	5.8
Blood oxygen saturations breathing air	14 2327	15 AP 2337	16 AP 2346	1 1444	2 AP 1507	3 AP 1523
Blood oxygen saturations breathing 100% O <sub>2</sub>			17 Lat 2400	4 Lat 1542		5 Lat 1556
Microspheres alone						
Microspheres and green dye	18* Sr AP 0046		20* Cr AP 0102	7* Yb 1737		9* Ce AP 1815
Microspheres and blood oxygen saturations						
Green dye alone		19* AP 0053		6* AP 1717	8* AP 1801	
Renovist alone						
Renovist and green dye	21* 0125	22* 0132	23* 0150	10, 11* 1857	12* 1930	13* 1941
X-ray alone						

TABLE III (contd.)

Experiment	Animal D - 26 Feb. 1969					
	+G <sub>y</sub>			-G <sub>y</sub>		
	1	2.9	5.8	1	2.9	5.8
Blood oxygen saturations breathing air						
Blood oxygen saturations breathing 100% O <sub>2</sub>						
Microspheres alone	4* Yb 1217		5* Cr AP 1238	1* Sr 1017		2* Ce 1038
Microspheres and green dye						
Microspheres and blood oxygen saturations						
Green dye alone						
Renovist alone						
Renovist and green dye						
X-ray alone						3* AP 1043

TABLE III (contd.)

Experiment	Animal E - 5 Mar. 1969					
	+G <sub>y</sub>			-G <sub>y</sub>		
	1	2.9	5.8	1	2.9	5.8
Blood oxygen saturations breathing air		3 AP 1423	6* AP 1536		8 AP 1902	
Blood oxygen saturations breathing 100% O <sub>2</sub>			5 Lat 1514			
Microspheres alone						
Microspheres and green dye						
Microspheres and blood oxygen saturations	2 Ce AP 1408		4 Yb AP 1445	7 Cr AP 1840		9 Sr AP 1918
Green dye alone						
Renovist alone						
Renovist and green dye						
X-ray alone	1 AP 1349					



TABLE III (contd.)

Experiment	Animal F - 19 Mar. 1969					
	+G <sub>y</sub>			-G <sub>y</sub>		
	1	2.9	5.8	1	2.9	5.8
Blood oxygen saturations breathing air		2 AP 1310	5* Lat 1406		7 AP 1742	10* Lat 1832
Blood oxygen saturations breathing 100% O <sub>2</sub>			4 AP 1345			9 AP 1816
Microspheres alone						
Microspheres and green dye						
Microspheres and blood oxygen saturations	1 Ce AP 1256		3 Sr AP 1327	6 Cr 1706		8 Yb AP 1758
Green dye alone						
Renovist alone						
Renovist and green dye						
X-ray alone						

- + Refers to sequence in which the experiment was performed.
- \* Time of day.
- # X-ray film obtained during the experiment.
- ø Radioactive label: Yb = <sup>169</sup>Ytterbium, Ce = <sup>141</sup>Cerium, Sr = <sup>85</sup>Strontium, Cr = <sup>51</sup>Chromium.
- θ Microspheres injected into the pulmonary artery. This was inadvertent and discovered in retrospect.
- \* IPPB used.

out before and during these exposures varied with each chimpanzee both because various medical problems were encountered during the course of study in each animal and because of the nature of the results obtained in the prior animals. When medical problems were encountered during the procedure, the planned experimental protocol was modified or curtailed in the light of the problem at hand. For example, the first chimpanzee was subjected to  $-2.9$  and  $-5.8 G_y$  accelerations only, because development of a large femoral hematoma at the site of the percutaneous introduction of the abdominal aorta sampling catheter discouraged further studies. In the second animal, a complete series of observations was carried out in the  $-G_y$  position but only a few runs were performed on the second ( $+G_y$ ) side because of a similar problem. Roentgenographic evidence of pulmonary atelectasis or pulmonary congestion was present to varying degrees at some stage of the experiment in all animals. A short experiment, limited only to radioactive microsphere injections, was performed on the fourth animal to determine if the length of the experiment affected the pattern of pulmonary blood distribution or the development of pulmonary atelectasis. No time dependency was demonstrated.

The stage in the experiment when IPPB was used was changed in the last two animals because it was thought to be a possible factor in the development of atelectasis. In these animals the microsphere injections were performed during the first exposures to acceleration

simultaneously with continuous determinations of the oxygen saturation of mixed venous and arterial blood. A second oxygen saturation run was then performed with IPPB alone. No definitive differences were demonstrated in the results obtained during this as compared to the prior experimental protocols for the first four animals, in which the microsphere injections were done later in the sequence.

On the average, eight hours were required to introduce and position the vascular, pleural, and other catheters; position the animal in the cockpit; and calibrate all gauges and instruments. The period with the animal in the cockpit, during which the actual experimental observations were carried out lasted from four to eight hours, depending on the number of centrifuge exposures planned in the protocol and the condition of the animal. The scanning procedure added another six to eight hours. The total time required for the study in each animal ranged from 18 to 36 hours during which the chimpanzee was maintained under anesthesia. All animals survived and are in good condition at the time of this report, except for the last animal (studied March 21, 1969) which was killed 40 hours after the centrifuge exposures due to the presence of a very large retroperitoneal hematoma from a needle puncture site through the posterior surface of the right femoral vein.

### III. RESULTS

#### Regional Distribution of Pulmonary Blood Flow

Both the dorsal and ventral surfaces of the thoraces of all six chimpanzees were scintiscanned after completion of the centrifuge exposures

while the animal was in the supine and in the prone body positions, respectively. The count rate data from each of the energy discrimination channels was entered on line into the CDC 3200 digital computer, as described elsewhere (8). Upon completion of the scanning procedure, the count matrix for each channel was corrected for both the energy "spill-over" arising from the presence of multiple isotope energies and the collimator's modulation transfer effects. The corrected count matrix was then permanently stored on digital magnetic tape and displayed graphically to the investigators. Figure 7 exemplifies a 30 x 26 count matrix of scintiscan results printed out by the computer from its permanent storage on digital tape. From this count matrix, three types of scintigraphic display formats were generated, as are illustrated in figure 2. The isotope used for figure 2 was  $^{141}\text{Ce}$ , which was injected while the animal was in the left lateral position at 1G (i.e., during exposure to gravitational force environment of  $+1 G_y$ ). The four three-dimensional surface maps, each viewing the data from a separate quadrant; the two isocount contour maps, one indicating fifteen and the other ten equal count stratification levels; the computer-determined isotope distribution (blood perfusion) silhouette; and the computed flow fraction for each lung were computed and displayed for each scintiscan.

The scintiscans of the ventral and dorsal surfaces of the thorax reflect the distribution of microspheres located near these respective surfaces and give an attenuated indication of activity located at more

distant thoracic coordinates. Therefore, the three-dimensional appearance of the displays should not be interpreted as accurate three-dimensional representations of the isotope distributions in the lung. This is the result of both the inverse square law and absorption or deflection of radiation emanating from distant microsphere deposits by tissue of varying thickness and density interposed between the radiation source and the collimation-detection head assembly, and because the collimation effects modify the sensitivity of the sodium iodide crystal so that its response is nonuniform to isotope deposits located distant to the collimator's face. A comparison of results from scintiscans of the dorsal and ventral surfaces of the thorax is shown in figure 8. A scan of the left lateral surface of the thorax which accentuates relatively the radiation emanating from near this surface of the chimpanzee's chest is also shown. The two distinct peaks of activity present in the lateral scan show the larger deposit of isotope as being located toward the base of the lung approximately midway between the dorsal and ventral surfaces of the thorax, while the smaller deposit or activity peak is found near the apex, near the ventral surface. The lateral coordinates of the peaks of activity, viewed from the plot of the counts summed in a cephalocaudal direction (i.e., in a transverse plane and referred to as a summation-to-transverse plane map), show that the activity of the basal midlung deposit is enhanced in the dorsal scan data, while the data from the ventral scan slightly enhance the activity detected from the apically lying isotope deposit.

Since the data from scans of the ventral and dorsal surfaces of the thorax tend to emphasize different aspects of the distribution of the microspheres in the lungs, some differences in the flow fraction computations for each lung from these respective scans result. For the scan of the dorsal surface of the thorax, illustrated in figure 8, the flow fraction for the left lung is 0.50. The corresponding flow fraction obtained from the ventral scan was 0.58. Past experience with correlations between external scintiscans from dogs and data obtained from their excised lungs indicates that the dorsal scintiscan best reflects the intrathoracic distribution of microspheres for the  $G_y$  acceleration conditions. The right and left lung flow fractions are, however, believed to be best represented by the average of the flow fractions obtained from scans of both the ventral and dorsal surfaces of the thorax.

Effect of Body Position During Scanning Procedure on Distribution of Pulmonary Microsphere Emboli in the Thorax

The interpretation of data from scintiscans carried out at 1G with the body in the prone or supine positions, in relation to the distribution of the impacted microspheres in the chest when at 1G, may be significantly affected by the change in position of the heart and lungs with change in body position. To determine if the shift of the lungs and heart, which occurs with a change in body position at 1G, had a significant effect on the apparent distribution of the microspheres impacted in the lung, replicate scintiscans of the dorsal surface of the thorax of one chimpanzee

were carried out when the animal was lying prone and when in the left and the right lateral positions. For the latter two positions, the direction of the collimator was adjusted from its usual vertical to a horizontal direction. The summation-to-transverse plane maps derived from these three dorsal scintiscans are compared in figure 9, and indicate that the distribution of microspheres obtained when in the prone and right lateral positions were essentially identical. The distribution obtained when in the left lateral position, however, showed a slightly greater peak activity in the left lung relative to the other two data sets. Computer-determined flow fractions, calculated from these three scintiscans of the dorsal surface of the thorax, indicate that the flow fraction to the dependent lung for the scintiscan in the prone position is intermediate between the values based on the scintiscans obtained when in the left and right lateral positions (see table IV). The inset in figure 9 is a picture of the face of an oscilloscope displaying a three-dimensional display of the data obtained when in the prone position.

As described in the procedure section, not all animals were injected with four isotopes. The first animal investigated (A) was studied in the right lateral position only. Consequently, only  $-G_y$  data are available. Data for the  $+G_y$  state of the fourth animal could not be processed due to a technical error.

All the scintiscan data presented in this report have been

TABLE IV

COMPARISON OF FRACTIONAL DISTRIBUTION OF MICROSPHERE EMBOLI (PULMONARY BLOOD FLOW) IN RIGHT AND LEFT LUNGS OF CHIMPANZEE DETERMINED FROM: REPLICATE SCINTISCANS OF DORSAL SURFACE OF THORAX WHEN IN DIFFERENT BODY POSITIONS IN VIVO, THE DORSAL SURFACE OF LUNGS ALONE FOLLOWING EMBEDDING IN URETHANE FOAM, AND FROM SUMMATION OF SCINTISCANS OF SURFACES OF TRANSVERSE SECTIONS OF THESE LUNGS

CONDITION OF SCINTISCAN	FORCE ENVIRONMENT AND ISOTOPE LABEL USED FOR FOUR INJECTIONS OF MICROSPHERES INTO RIGHT VENTRICLE							
	+1 Gy 141Ce		+5.8 Gy 85Sr		-1 Gy 51Cr		-5.8 Gy 169Yb	
	Left <sup>D</sup> * Lung	Right Lung	Left <sup>D</sup> Lung	Right Lung	Left Lung	Right <sup>D</sup> Lung	Left Lung	Right <sup>D</sup> Lung
Left Lateral Position In Vivo	0.61	0.39	0.80	0.20	0.29	0.71	0.23	0.77
Prone Position In Vivo	0.57	0.43	0.77	0.23	0.25	0.75	0.17	0.83
Right Lateral Position In Vivo	0.55	0.45	0.73	0.27	0.24	0.76	0.13	0.87
Lungs Alone -- Embedded in Urethane	0.62	0.38	0.73	0.27	0.23	0.77	0.03	0.97
Sections of Lungs	0.63	0.37	0.78	0.22	0.18	0.82	0.10	0.90

\* Chimpanzee F (See Table I).

\* The subscript D indicates the dependent lung.



grouped into the first or the second lateral body position studied. This is because the pulmonary blood-flow distribution patterns and flow fraction values obtained during the first lateral body position studied gave more uniform results than the blood-flow distribution patterns found during the second lateral body position in the same animals. Table V summarizes the flow fraction values under these groupings.

#### First Lateral Body Position Studied

The five animals (A,B,C,E,F) for which data were obtained during the initial 1 G<sub>y</sub> study all showed the peak of radioactivity located over the diaphragmatic regions of the right and left lungs where the largest quantity of lung volume is located. The activity then decreased toward background levels with distance from this peak activity region, in both lateral and cephalocaudad directions. Occasionally, a smaller peak of activity was located in the most apical middorsal-ventral regions of the lungs, just cephalad to the cardiac silhouette. With the exception of chimpanzee A, the dependent lung contained the largest peak of radioactivity consequent to the injections carried out during the initial period at 1 G<sub>y</sub>. The flow patterns for animals E and F are given in figure 10, A and B.

Percentage flow fraction values for the initial 1 G<sub>y</sub> state showed 57%, 55%, 54%, and 58% of the total activity was over the dependent lung in animals B, C, E, and F, respectively. This value for animal A was 36%.

TABLE V

BLOOD FLOW FRACTION TO RIGHT AND LEFT LUNGS DERIVED FROM SCINTISCANS OF DORSAL AND VENTRAL SURFACES OF THE THORAX FOR RADIATION FROM MICROSPHERES INJECTED INTO

RIGHT VENTRICLE DURING + 1 Gy AND ± 5.8 Gy ACCELERATIONS

CHIMPANZEE	LATERAL POSITION STUDIED FIRST	FIRST BODY POSITION STUDIED				SECOND BODY POSITION STUDIED			
		1 Gy Flow Fractions		5.8 Gy Flow Fractions		1 Gy Flow Fractions		5.8 Gy Flow Fractions	
		D*	S	D	S	D	S	D	S
A	Right	0.36	0.64	0.53	0.47	--(3)	--	--(3)	--
B	Right	0.57	0.43	0.47	0.53	--(1)	--	--(1)	--
C	Right	0.55	0.45	0.41	0.59	0.06	0.94	0.0	1.00
D	Right	--(2)	--	0.96	0.04	0.29	0.71	0.35	0.65
E	Left	0.54	0.46	0.49	0.51	0.39	0.61	0.57	0.43
F	Left	0.58	0.42	0.84	0.16	0.64	0.36	0.69	0.31
AVERAGE		0.56	0.44	0.63	0.37	0.34	0.66	0.42	0.58

\*D and S refer to dependent and superior lungs respectively.

(1) Injection catheter in pulmonary artery.

(2) Insufficient isotope injected.

(3) Left side not studied.

With an increase in the inertial force environment to 5.8 G<sub>y</sub>, the following effects were noted: In three of the four animals which had similar distribution patterns at 1 G<sub>y</sub> (B,C, and E), the flow fractions shifted in favor of the upper lung so that the percentage of total activity detected over the dependent lung averaged 46% (range 41-49%) of the total over the thorax. In these animals, the greater change in activity was over the lower lung. These data are exemplified in figure 10A. The comparison of +1 G<sub>y</sub> and +5.8 G<sub>y</sub> data shown in the plot of the summed counts on a transverse plane of this figure best indicates the flow re-distribution associated with the exposure to +5.8 G<sub>y</sub> in this animal.

Animals A,D, and F showed an increase in flow fractions to the dependent lung to values of 53%, 96%, and 84%, respectively, during the +5.8 G<sub>y</sub> exposure. The contour map for animal F (fig. 10B) for the 1 G<sub>y</sub> and 5.8 G<sub>y</sub> exposures shows that the peak activity in the dependent (left) lung shifted toward the lateral and diaphragmatic regions. The activity found in the superior lung indicated that the blood flow pattern in this lung was displaced towards the midline along the lateral (superior) margin of the cardiac silhouette.

#### Second Lateral Body Position Studied

The flow patterns observed in the five animals (B,C,D,E,F) studied in the second body position were more variable. One of these five (B) showed almost all of the isotope to be present in the dependent

(left) lung, for both the +1 G<sub>y</sub> and 5.8 G<sub>y</sub> conditions. In retrospect, it was discovered that the position of the injecting catheter had shifted while changing the animal from the right to left lateral cast so that the tip had advanced into the left pulmonary artery. Flow fractions computed for this animal in the second body position are, therefore, not included in the overall analysis.

The data from three of the remaining four animals (C,D,E) indicated that at 1 G<sub>y</sub>, the larger fraction of blood flow (average 63%, range 61% to 94%) was traversing the superior lung. This finding was the opposite of the distribution pattern found during the injection made at 1G during the initial body position studied in animals C and E (fig. 10A). Comparison of the contour maps of the isotope distributions, shown in this figure, indicates the peak of activity in the superior lung was shifted to a more apical location.

The last animal studied (F) showed the greater fraction of flow (64%) at 1 G<sub>y</sub> was to the dependent (right) lung, as was the case for the left lung of this animal when this lung was dependent, during the first injection in the lateral (+1 G<sub>y</sub>) body position. It is apparent from the contour map for this -1 G<sub>y</sub> condition, shown in figure 10B, that the lateral (superior) region of the upper (left) lung contained minimal activity. When this animal was exposed to the -5.8 G<sub>y</sub> force environment, the flow fraction to the dependent (right) lung increased slightly from 64% to 69%.

Upon exposure to the  $-5.8 G_y$  environment, animals D and E also showed increases in the calculated flow fractions to the dependent lung from 39% to 57% to the right lung in chimpanzee E, and from 29% to 35% to the left lung in chimpanzee D. In both animals, lack of radioactivity over the lateral, uppermost border of the superior lung was notable, as was the shift of the peak activity in both lungs toward the midline. This midline-directed redistribution pattern is similar to that noted in animals B, C, and E at  $1 G_y$  when in the first lateral body position during the exposure to  $5.8 G_y$ .

The distribution of isotope in the second (left lateral) position, studied in animal C, was clearly unlike that of the other animals, with over 90% of the activity appearing in the superior (right) lung at  $+1 G_y$  and during the exposure to  $+5.8 G_y$ . Roentgenograms taken during this  $+5.8 G_y$  exposure and at  $+1 G_y$  after the exposure showed extensive collapse and congestion of the dependent (left) lung. The etiology of this pathological finding in the dependent lung is unknown, but the prior multiple exposures to  $+5.8 G_y$  during IPPB and blood oxygen saturation studies may have been contributing factors.

Comparison of Scintiscan Data Obtained from the Intact Thorax In Vivo and from Scintiscans of the Excised Lungs of the Same Animal

Flow fractions were computed from scintiscan data from the excised lungs of animal F, for comparison with values based on the scintiscans carried out in vivo. Flow fractions were computed from scintiscans

made of the dorsal aspect of the embedded lungs before the sectioning process and from the surfaces of twelve cross sections of these same lungs. Comparison of these values with the results from scintiscans carried out in vivo are shown in table IV. The differences in calculated fractional blood flows to the two lungs for all four conditions studied (i.e.,  $\pm 1 G_y$  and  $\pm 5.8 G_y$  force environments), based on these different types of scintiscans, ranged from 1% to 5% (table IV). These differences in flow fraction values are believed to be within the experimental error of the methods used.

The distribution of microspheres injected when animal F was in the left lateral ( $+1 G_y$ ) body position (the first body position investigated) showed all lobes of the dependent (left) lung contained radioactivity, as did the superior lung, but to a lesser degree. The extreme apical and diaphragmatic lung sections contained only minimal deposits of microspheres. The distribution of microspheres injected during the exposure to  $+5.8 G_y$  was little changed in the dependent lung; however, radioactivity in the superior (right) lung was displaced in the dependent direction; i.e., toward the midline of the thorax.

The distributions of microspheres injected when in the right lateral ( $-1 G_y$ ) body position indicated that essentially all of the microspheres impacted in the upper and lower lobes of the dependent (right) lung. The left lung and the middle lobe of the dependent (right) lung contained minimal radioactivity. The distribution of the micro-

spheres injected during the exposure to  $-5.8 G_y$  showed displacement toward the midline of the radioactivity patterns of the right upper and lower lobes and very little radioactivity in the middle lobe and in the superior (left) lung. Chest roentgenogram obtained before and after these last two injections of microspheres showed increased radiopacity in the region of the middle lobe. Examination of the lung at postmortem showed a hemorrhagic congested right middle lobe. Other regions of the lungs were normal. The cause of the pathophysiology in the right middle lobe was not apparent.

#### Spatial Distribution of Microspheres (Blood Flow) Per Unit of Lung Volume

Data concerning the spatial distribution of microspheres per unit of volume were obtained from the cross-sectional scintiscan data by dividing the count values of each lung slice by the measured volume of lung tissue over which the count value was recorded. These count values are presumed to be proportional to the blood flow per equal volume of lung parenchyma at each respective spatial position in the thorax. These values were averaged along transverse, sagittal, and coronal planes to generate summation-to-transverse plane maps. As illustrated in figure 11, the effect of an increase in the magnitude of the  $G_y$  force environment on the spatial distribution of pulmonary perfusion is to increase blood flow to lung parenchyma in the medial regions of the lung while, simultaneously, the relative pulmonary flow, both to superior and dependent lateral regions of the thorax, is decreased.

Comparison of figure 11 with the regional summation-to-transverse plane maps of figures 10A and 10B show that the changes in blood-flow values expressed per unit volume of lung are similar to the changes in regional distribution of pulmonary blood flow in the thorax uncorrected for differences in lung volume at these sites.

#### Changes in Oxygen Saturation of Arterial and Mixed Venous Blood

Blood oxygen saturation studies were carried out in 4 of the 6 animals included in this study. The temporal relationships of changes in the oxygen saturation of blood being withdrawn continuously from the aorta during exposures to  $G_y$  acceleration are similar to those previously observed in this laboratory in human beings and dogs during exposures to transverse ( $G_x$  and  $G_y$ ) accelerations (15,33,24). These relationships are illustrated in figures 12 and 13, and were obtained from chimpanzee F, before, during, and after 60- to 80-sec exposures to force environments of  $\pm 2.9$  and  $\pm 5.8 G_y$ , respectively. The maximum decreases in arterial oxygen saturation during the exposures to  $+ 2.9 G$  and  $-2.9 G$  averaged 10.7% and 5.8%, respectively.

Typically, there is a rapid decrease in the systemic arterial blood oxygen saturation beginning within a few seconds after the onset of acceleration. The arterial oxygen saturation decreased to a minimum or near minimum value during the first 30 seconds of the plateau phase of the acceleration profile and then either remained constant or increased slightly toward the end of the plateau level of acceleration which



averaged 67 seconds in duration. The arterial oxygen saturation at the end of the exposure to the plateau level of acceleration averaged 85% (range 81% to 92%) for the 2.9 G<sub>y</sub> runs in three animals, and 72% (range 72% to 73%) for four animals exposed to 5.8 G<sub>y</sub> (table VI). A significant systematic difference between the degree of arterial desaturation produced by plus and minus G<sub>y</sub> acceleration was not observed (table VII).

The oxygen saturation of mixed venous blood sampled from the main pulmonary artery showed little change during the onset of acceleration and did not begin to decrease until approximately 25 seconds after the acceleration plateau was reached. Unlike the arterial oxygen saturation which decreased to a low value early in the exposure and then remained fairly constant, the saturation of the mixed venous blood continued to decrease throughout the run. Values as low as 36% were recorded at the end of a 70-second exposure to 5.8 G<sub>y</sub>.

The arterial oxygen saturation began to increase rapidly shortly after the onset of the deceleration phase of the exposure but usually did not recover to the preacceleration control value until several minutes after the return to 1G. The pulmonary artery oxygen saturation usually continued to decrease for as long as 25 seconds after the centrifuge had stopped, before gradually returning to the control value. The time required for the arterial and venous oxygen saturation values to recover to their preacceleration control values was proportional

TABLE VI  
PERCENT OXYGEN SATURATION OF ARTERIAL AND MIXED VENOUS  
BLOOD OF 4 CHIMPANZEES UNDER SERNYLAN-PENTOBARBITAL ANESTHESIA BEFORE,  
DURING, AND AFTER EXPOSURE TO G<sub>y</sub> ACCELERATION

G	CONDITIONS	CHIMP.	PREACCELERATION <sup>2</sup>		PEAK G <sup>3</sup>		END PEAK G <sup>4</sup>		POST ACCELERATION <sup>5</sup>		TIME TO MIN. <sup>6</sup>	
			ART. 7	VEN. 8	ART.	VEN.	ART.	VEN.	ART.	VEN.	ART.	VEN.
+3G <sub>y</sub>	Room Air	C, E, F	88(2) <sup>1</sup>	62(2)	78(2)	62(2)	81(1)	60(3)	86(2)	59(3)	55(20)	80(20)
-3G <sub>y</sub>	Room Air	B, C, F	97(1)	65(8)	92(1)	65(8)	92(1)	63(8)	97(1)	64(9)	48(15)	65(14)
+5.8G <sub>y</sub>	Room Air	C, E, F	90(1)	63(2)	78(5)	61(3)	72(5)	57(6)	87(2)	56(2)	73(17)	100(11)
-5.8G <sub>y</sub>	Room Air	B, C, E, F	91(4)	58(7)	79(4)	54(9)	73(3)	50(8)	89(4)	55(9)	55(9)	64(19)
+5.8G <sub>y</sub>	99.6% Oxygen	C, E, F	100(0)	81(3)	100(0)	82(4)	91(6)	70(1)	98(1)	68(4)	116(18)	135(25)
-5.8G <sub>y</sub>	99.6% Oxygen	C, F	100(0)	72(4)	99(0)	72(4)	92(2)	63(6)	94(0)	64(7)	70(22)	102(1)

1) The number enclosed within parentheses is the standard error of the mean values.

2) Oxygen saturation values just prior to onset of centrifuge rotation.

3) Values within 5 seconds of plateau level of acceleration onset.

4) Oxygen saturation determined immediately before deceleration to 1G<sub>y</sub>.

5) Oxygen saturation at 1G 40 seconds after the centrifuge had stopped.

6) Number of seconds after onset plateau level of acceleration that minimum saturation occurred.

7) Mixed arterial sample obtained from thoracic aorta.

8) Mixed venous sample taken from pulmonary artery.

The average duration of the plateau level of acceleration when breathing air was 66 seconds at 2.8 G and 73 seconds at 5.8 G (range 62-92 seconds). When breathing 99.6% oxygen, the average duration of the exposures to 5.8 G was 86 (range, 60-135) seconds.

TABLE VII

COMPARISON OF DECREASES OF ARTERIAL OXYGEN SATURATIONS DURING EXPOSURES  
TO PLUS AND MINUS G<sub>y</sub> ACCELERATION WHEN BREATHING AIR

ANIMAL	+2.9G <sub>y</sub>	-2.9G <sub>y</sub>	+5.8G <sub>y</sub>	-5.8G <sub>y</sub>	First Side Down
C	20%(92)	7%(96)	30%(89)#	15%(95)	-G <sub>y</sub>
E	7%(85)	4%(74)	11%(89)	11%(77)	+G <sub>y</sub>
F	5%(87)	3%(96)	17%(91)	23%(96)	+G <sub>y</sub>

The brackets enclose blood oxygen saturation values in percent when at 1G<sub>y</sub> just prior to centrifugation.

# Chest roentgenogram indicated collapse of the dependent lung during this exposure.

to the magnitude of the acceleration.

The temporal relationships between changes in oxygen saturation and the acceleration profile were modified when the animal breathed 99.6% oxygen, or when respiration was assisted by intermittent positive-pressure breathing (IPPB). Figure 13 illustrates the changes in blood oxygen saturation in an animal breathing 99.6% oxygen during the 5.8  $G_y$  acceleration runs. Prior equilibration was accomplished by breathing 99.6% oxygen for ten minutes before the run. This response was typical for the other animals under similar conditions. In contrast to the changes seen when breathing room air spontaneously, the decrease in arterial oxygen saturation did not begin with the onset of acceleration, but was delayed for approximately 30 to 60 seconds after reaching the plateau level of acceleration. Furthermore, the decrease was not as great when the animal breathed 99.6% oxygen as when room air was breathed. The changes in arterial oxygen saturation induced by  $G_y$  acceleration during IPPB with air were similar to those observed when breathing air spontaneously.

Figures 12 and 13 also illustrate changes in tidal volume and respiratory rate typically observed during the centrifuge runs. The rate increased approximately 15 respirations per minute after the onset of acceleration and was maintained. The rate usually returned to the preacceleration control value shortly after the centrifuge was stopped. Tidal volume decreased transiently to approximately 50% of the control tidal volume during the onset of acceleration, but returned to control

levels during the centrifuge run.

The blood oxygen saturation values and computed physiologic pulmonary arteriovenous shunts when breathing room air, and anatomic shunts when breathing 99.6% oxygen during the exposures 2.9 and 5.8 G<sub>y</sub> accelerations are shown in table VIII. The method used to compute the shunt is described by Comroe et al.(7). Systematic changes in the shunt values were not demonstrated when the animals were turned to the opposite side, and there was no systematic difference between the maximum levels of shunts observed during exposure to -5.8 G<sub>y</sub> and +5.8 G<sub>y</sub> respectively (table IX).

#### Intrathoracic Pressure Measurements

Intravascular and pleural pressures were measured from the photokymograph recordings in all cases as follows: In the control period, the pressures are end-expiration values, averaged for the last three respiratory cycles before the centrifuge started. During the acceleration plateau, end-expiration pressures were measured at the time of a microsphere injection or cardiac output measurement. If neither procedure had been performed, the pressures were measured approximately at the midpoint of the plateau period of the acceleration profile.

The aortic, pulmonary artery, and pleural pressures for the last three animals studied (D, E, and F) were entered into the computer on-line from the animal throughout each centrifuge run. The computer

TABLE VIII

PHYSIOLOGICAL SHUNTS: COMPARING FIRST SIDE DOWN WITH SECOND SIDE DOWN

	2.9G <sub>y</sub> Room Air		5.8G <sub>y</sub> Room Air		5.8G <sub>y</sub> 100% Oxygen	
	CONTROL*	MAXIMUM†	CONTROL	MAXIMUM	CONTROL	MAXIMUM
FIRST SIDE DOWN	0.21 (0.11)#	0.45 (0.07)	0.16 (0.08)	0.63 (0.02)	—	0.35 (0.04)
SECOND SIDE DOWN	0.11 (0.07)	0.38 (0.35)	0.19 (0.07)	0.57 (0.09)	—	0.53 (0.25)

All shunts expressed as fractions of one.

# Standard error of the mean for the figure above it.

\* Control period immediately before the centrifuge starts.

† Maximum is the maximum shunt observed during the plateau or deceleration phase of the centrifuge run.

TABLE IX

PHYSIOLOGICAL SHUNT BEFORE AND DURING EXPOSURE TO Gy STRESS

G	CONDITION	CHIMP. B			CHIMP. C		CHIMP. E		CHIMP. F		AVERAGE <sup>4</sup>	
		CONT. 2	MAX. 3		CONT.	MAX.	CONT.	MAX.	CONT.	MAX.	CONT.	MAX.
+3Gy	Room Air	—	—	0.16	0.66	0.45*	0.63*	0.28*	0.45*	0.24	0.58	
-3Gy	Room Air	0.0*	0.34*	0.10*	0.38*	—	—	0.05	0.09	0.05	0.27	
+5.8Gy	Room Air	—	—	0.23	0.71	0.33*	0.58*	0.18*	0.63*	0.25	0.54	
-5.8Gy	Room Air	0.0*	0.67*	0.14*	0.64*	0.31	0.53	0.04	0.46	0.16	0.57	
+5.8Gy	99.6% Oxygen	**	**	—	0.70	—	0.36*	—	0.32*	—	0.46	
-5.8Gy	99.6% Oxygen	**	**	—	0.37*	**	**	—	0.36	—	0.37	

All the shunts values are expressed as decimal fractions.

2) Control 1Gy value before centrifuge started.

3) Maximum shunt value during entire centrifuge run.

4) Average shunt value for all chimpanzees.

\* ) Denotes which side was dependent during the first series of centrifuge runs.

\*\* ) Arterial oxygen saturation was 100%; therefore, shunts of less than about 20% cannot be detected due to unknown amounts of physically dissolved oxygen.

averaged these end-expiratory pressures over consecutive ten-second intervals, and corrected the circulatory pressures to midlung level and pleural pressures to the level of the respective catheter tips on the basis of the recorded thistle-tube zeros and measurements of the midlung and catheter-tip positions made from thoracic roentgenograms. In all cases, the computer measurements were in satisfactory agreement with values measured manually from the photokymographic recordings.

#### Pleural Pressures

In the five animals in which pressures were obtained, the pressures recorded from the lateral (uppermost) margin of the superior lung were uniformly more negative than those recorded from the lateral (dependent) margin of the lower lung. In some animals, a positive pressure was recorded from the dependent (lateral) margin of the pleural cavity even at 1 G<sub>y</sub>. These differences in pleural pressure at superior and dependent regions in the thorax increased uniformly during exposures to acceleration.

Figure 14 illustrates these points in one of the animals; figure 15, the averages of all the animals. In general, the results are similar to the results of previous centrifuge studies performed on dogs in this laboratory (21). With increasing acceleration, a progressive divergence of the pressures occurred, with that recorded from the dependent region in the thorax becoming more positive and that from the superior site more negative.



The mean end-expiratory pleural pressure recorded at the lateral margin of the superior lung in the five chimpanzees at  $1 G_y$  was minus 10.1 cm water (range -3 to -17), while the mean end-expiratory pressure at the dependent site was plus 1.9 cm water (range -1 to 10). The mean vertical distance separating the catheter tips during the control periods at  $1 G_y$  was 17.4 cm. The calculated pressure gradient per cm of vertical distance averaged 0.75 (range 0.45 to 1.91) cm of water when in the right lateral ( $-G_y$ ) position and 0.63 (range 0.50 to 0.89) cm of water in the left lateral ( $+G_y$ ) position. The apparently erroneously high gradient of 1.91 at  $-1 G_y$  in animal A is unexplained. The average gradient for the other four animals in this position was 0.52 (range 0.45 to 0.65).

The changes in pleural pressure during the exposure to acceleration were in direct proportion to the level of acceleration, as indicated by the changes in the slopes of the lines shown in figure 16. The gradients (cm water/(cm distance x G)) however, remained the same, suggesting that the regional differences in intrapleural pressures are related to the weight of the thoracic contents. Assuming this to be true, the average specific weight of the thoracic contents for the five chimpanzees is 0.72, which is the gradient in cm water/cm vertical distance x acceleration averaged from all experiments.

#### Aortic and Pulmonary Artery Pressures

The pressure changes in the thoracic aorta and pulmonary artery during  $G_y$  acceleration were highly variable, not only between

animals but between experiments in the same animal. To best summarize the results, the percent changes in aortic and pulmonary artery pressures from the prerun 1G control values were computed for each centrifuge experiment. The computed values from similar experiments at the same acceleration were then averaged for all animals and the results plotted as illustrated in figures 17 and 18. Systolic and diastolic pressure changes are plotted separately, and the number of experiments of each type performed is shown above each plot. Table X summarizes the percent changes in pressure in the 2.9 and 5.8  $G_y$  conditions averaged from all the experiments performed in all the animals.

In general, aortic and pulmonary artery pressures were greater at 2.9  $G_y$  and 5.8  $G_y$  than during the control period. Pulmonary artery pressures at 2.9  $G_y$  were similar to the values at 5.8  $G_y$ . The changes observed could not all be related to acceleration alone, and various experimental conditions were possibly equally important. However, the small number of observations for each experiment and the considerable variation in the responses preclude any definite conclusions concerning their relative importance.

No systematic differences were demonstrated between the changes in aortic and pulmonary artery pressures recorded during exposures to plus and to minus  $G_y$  acceleration.

#### Left Atrial Pressures

Left atrial pressure was measured in three animals. The left atrial catheter in these cases was also used for blood sampling during

TABLE X  
PERCENT CHANGE IN VASCULAR PRESSURE DURING Gy ACCELERATION

Acceler- ation	PULMONARY ARTERY									
	SYSTOLIC PRESSURE					DIASTOLIC PRESSURE				
	MEAN*	RANGE	S.E. of Mean	P Value	MEAN	RANGE	S.E. of Mean	P Value		
-3G <sub>y</sub>	5 (5,7)	-18 to +22	4.9	N	8	-15 to +32	6.8	N		
-6G <sub>y</sub>	33 (6,14)	-20 to +200	14.7	0.01 to 0.025	105	-68 to +600	47.6	0.01 to 0.025		
+3G <sub>y</sub>	6 (3,3)	-10 to +25	0.58	N	18	-3 to +53	17.9	N		
+6G	45 (5,11)	0 to +22	10.3	0.005	72	-27 to +225	20.5	0.005		

Acceler- ation	AORTA									
	SYSTOLIC PRESSURE					DIASTOLIC PRESSURE				
	MEAN*	RANGE	S.E. of Mean	P Value	MEAN	RANGE	S.E. of Mean	P Value		
-3G <sub>y</sub>	10 (4,7)	+3 to +17	2.3	0.005	15	+5 to +28	3.8	0.005		
-6G <sub>y</sub>	10 (6,16)	-8 to +20	2.0	0.005	15	-1 to +25	1.8	0.005		
+3G <sub>y</sub>	8 (3,4)	+1 to +14	3.0	0.025 to 0.05	10	+1 to +16	3.5	0.025 to 0.05		
+6G <sub>y</sub>	3 (5,12)	-17 to +27	4.0	N	8	-14 to +30	4.6	N		

\* The numbers in parentheses indicate the number of animals and the number of exposures to increased gravitational - inertial force environment, on which the mean is based.

N = > 0.05

oxygen saturation experiments, and therefore, the left atrial pressure was not recorded in all centrifuge runs in these three animals.

Mean left atrial pressures in the control periods were fairly uniform and the changes during acceleration, although varying to about the same extent as pressure changes in the thoracic aorta, generally increased with acceleration.

Mean left atrial pressure, averaged for the four animals during seven exposures to 5.8Gy, showed an increase from 5 cm H<sub>2</sub>O (range -4 to 18) in the control period, to 13 cm H<sub>2</sub>O (range -6 to 32) during the exposure. There were too few measurements to demonstrate possible systematic relationships between changes in left atrial pressure and the level and direction of Gy acceleration to which the animal was exposed.

#### Esophageal Pressures

The position of esophageal catheter tip frequently changed from one experiment to the next, either because of manipulation to remove gastric air or esophageal secretions, or due to the effect of the acceleration. For this reason, esophageal catheter pressures, although recorded during all of the experiments, are not reported in this paper.

#### Roentgenographic Results

An anterior-posterior (A-P) or a lateral thoracic roentgenogram was obtained during every exposure to Gy acceleration. Similar films were obtained at 1Gy prior to and at the end of each series of exposures in each body position.

The films were necessary to verify the correct position of the right ventricular outflow tract catheter used during the micro-sphere injections, and for measurements of the positions of the levels of the menisci in the bilateral thistle-tube system and the catheter-tip positions in relation to midlung level required for correcting pleural pressures to catheter-tip levels and circulatory pressures to midlung level. Radiological changes were observed in the lung fields in all animals, and are presumed to be of importance in the interpretation of the significance of changes in the regional distribution of pulmonary blood flow and blood oxygen saturation values observed concomitantly in these animals.

Two types of radiological changes were distinguished, and these are as follows: 1) Transient changes related to the lateral position, which quickly resolved when the animal was removed from the centrifuge and positioned supine. The roentgenograms reproduced in figures 19 and 20 are typical of these changes. Figures 19 and 20 illustrate mediastinal displacement to the dependent side typical for the left side down (+1 G<sub>y</sub>) and the right side down (-1 G<sub>y</sub>), respectively. Inertial displacement of the mediastinum is pronounced as the 5.8 G<sub>y</sub> films of figures 19 and 20 illustrate. These films also show a reduction of transverse diameter of the thorax with narrowing of the intercostal spaces on the dependent side and uniform fine mottling of the dependent lung field. However, none of these transient changes is apparent in a supine film of the same animal obtained after the experiments were completed.

2) Persistent pathological changes which appeared during the experiment and which were not quickly reversible following repositioning the animal or brief inflation of the lung to 30 cm of water pressure. The roentgenographs reproduced in figure 21 illustrate these changes in the third chimpanzee (C). Figure 21b indicates extensive atelectasis of the dependent lung which persisted when the animal was removed from the lateral half-body cast and placed supine (fig. 21c). A roentgenogram obtained two hours later showed persistent atelectasis.

The pathological changes observed in the roentgenograms of the first, third, and last animals (A, C, and F) probably influenced the distribution of pulmonary blood flow, as was indicated by the lack of radioactivity in the middle lobe of the dependent lung of animal F at necropsy. In the first animal, the roentgenogram obtained prior to the initial centrifuge exposure indicated extensive collapse of the dependent (right) lung which was attributed to obstruction of the right main bronchus by an improperly placed endotracheal tube. The scintiscan of microspheres injected during this condition showed minimal activity (i.e., minimal blood flow) in the apical region of this lung.

#### IV. DISCUSSION

##### Regional Distribution of Pulmonary Blood Flow

Flow fraction computations, and three-dimensional, contour, and summation-to-transverse plane scintigraphic maps, depicting the regional distribution of radioactive microsphere emboli in the lungs following

injections during exposures to different gravitational-inertial force environments, have been used to describe the effect of these environments on the regional distribution of pulmonary blood flow. The physiological significance of these scintiscan data is based on three assumptions: 1) that the microspheres, following their injection as a bolus into the right ventricular outflow tract, distribute into right and left pulmonary arteries in direct proportion to the blood flow in these vessels; 2) that the microspheres are uniformly distributed in the blood flowing in the right and left pulmonary arteries so that the regional distribution of pulmonary blood flow in capillary beds in different regions of the lungs is described by the regional deposition patterns of the impacted microspheres in those beds; and 3) the presumed proportionality relationship between the distribution of microsphere emboli and blood flow is not altered during exposures to acceleration.

Support for the first assumption relates to Rudolph (20), who has shown that 50- $\mu$ -diameter microspheres, when injected into the umbilical cord of living fetal sheep, distribute to each organ of the fetus in direct proportion to the blood flow occurring to that organ. His data, in addition, show that the ratio of blood flow in two umbilical veins, when measured by electromagnetic flowmeters, is essentially equal to the ratio of nuclide counts recorded from impacted microspheres found in the placental regions drained by each vein.

Support for the second assumption is based upon the work

of Tow (23), who has shown that a correlation of 0.97 exists between regional distributions of radiiodinated serum albumen (RISA 131) and simultaneously injected chromium-51-labeled red blood cells. RISA and microsphere emboli differ in that microspheres are 1.4 times heavier than the macroaggregate albumen. Reed (18) has studied effects of differences in gravity on the distribution of microspheres, and has presented evidence which shows that no appreciable variation exists in the patterns of distribution in the lungs when microspheres with specific gravities ranging from 0.2 to 3.0 were injected into the right ventricular outflow tract of dogs.

The third assumption that inertial force environments do not produce significant alterations in the microsphere emboli and blood-flow proportionality relationship is also based on the closely similar deposition patterns of microspheres with specific gravities ranging from 0.2 to 3.0 demonstrated by Reed.

An important concept inherent in the scintiscan matrix computations of this report is that detected isotope deposition patterns reflect regional blood-flow distribution patterns in a directly proportional manner only when the scintiscan recording system's modulated transfer (i.e., collimation distortion) and background radiation count effects have been removed. This is evident when considering that, during the scanning process, radiation emanating from isotope particles displaced from the focal axis of the collimated NaI crystal de-



tecting head is detected to some extent. The recorded count values at any specific sampling location are, therefore, a function of both the magnitude of isotope deposits along the actual focal axis of the head and, to a lesser degree, the magnitude of isotope deposits which surround this axis. Since no collimator can yield perfect collimation, the modulated transfer effects have to be mathematically removed from the scintiscan data using a prior knowledge of the modulating transfer process. Iinuma (13) has studied this problem and has presented a satisfactory method for removing the modulated transfer effects inherent in scintiscanning methodology. The displays of scintiscan data from the dorsal surface of the thorax, exemplified by figures 9 and 10, show that the distribution of microspheres was bimodal in form in relation to the right and left lungs. The gravitational-inertial force environment existing at the same time of the microsphere injection affected the relative peak and total count values over each lung as well as the spatial distribution of these counts. The three-dimensional surface maps have been found useful for delineating small variations in the patterns of blood-flow distribution. Contour maps were found to best indicate the gross changes in the dispersion patterns. The summation-to-transverse plane maps, obtained by averaging the recorded count matrix along transverse or cephalocaudal lines, have proved useful for comparison of results from different  $G_y$  accelerations or different body positions.

The assumption of a linear relationship between the recorded count matrix and the regional distribution of pulmonary blood flow provides a basis for calculating from external thoracic scintiscan data the fraction of cardiac output perfusing each lung. The pattern-recognition criterion needed by the computer programs for delineating the boundaries of the lung areas which were being perfused with blood tagged with microspheres was based upon superposition of the lung borders determined roentgenographically onto the contour maps of the count values. The fraction of cardiac output perfusing each lung was then assumed equal to the fraction of the total counts recorded over each lung within the defined borders, divided by the total counts recorded over both lungs. These computer-determined flow fractions provided the basis for estimations of the fraction of the total blood flow traversing each lung during different  $G_y$  experimental conditions. The validity of these flow fraction measurements is not completely known, but our measurements on excised dog lungs, plus the correlative work of Rudolph (20), indicate that values obtained are representative of the distribution of cardiac output to each lung during the conditions studied.

The observed redistribution of pulmonary blood flow toward midline thoracic regions during the measurements in the initial body position studied suggests that the spatial distribution of blood flow in

the dependent lung is affected by factors different from those affecting the superior lung. Figure 10 indicates that during exposures to  $5.8 G_y$ , blood flow in the superior lung redistributes toward the midline (i.e., the inferior regions). The blood flow in the dependent lung, however, also redistributes toward the midline in a direction which is opposite to the direction of the increased gravitational-inertial force environment. Possible explanations for this superiorly directed redistribution are: 1) capillaries in the inferior regions of the dependent lung enlarge during acceleration, allowing some microspheres to shunt into the systemic circulation and thereby produce an apparent increase in blood flow to the superior lung; 2) a dependently directed shift in the lung tissue during accelerative conditions which allows microspheres traveling toward inferior lung regions to impact the dependently displaced superior lung sections which subsequently return to their normal superior lung coordinates upon the tissue's return to its preacceleration position; and 3) an increase in the vascular resistance to blood flow to inferior regions of the dependent lung which forces the blood to redistribute in an upward direction toward the medial regions of this lung.

If dependent capillary enlargement allowed significant numbers of microspheres to pass through these regions of the lung, A-V shunts of  $35\text{-}\mu$  diameter or greater must have occurred, and the microspheres which passed into the systemic circulation would have impacted in regions of the body in proportion to the blood flow to these regions. Evidence obtained in live, open-chested dogs (19) following injections of glass

microspheres has suggested capillary vessels having diameters as large as 390  $\mu$  do exist. Data from table V indicate that, on the average, 14% of the dependent lung's microsphere activity would have to pass through A-V shunts of 35  $\mu$  or greater during accelerative 5.8 G<sub>y</sub> environments in order to achieve a 7% relative increase in superior lung blood flow. We have looked for peripheral deposits of microspheres in systemic regions of high blood flow such as the kidneys, liver, and brain, and could find no significant radiation, suggesting that if such A-V shunts do exist, the numbers of microspheres which may have traversed the pulmonary vasculature were small and so dispersed, they could not be detected using external scintillation detectors.

A dependently directed shift in lung parenchyma, resulting from an increase in the weight of the lung parenchyma and blood during acceleration, does occur. Because of the lung's enclosure in a semi-rigid thorax, the surrounding negative intrapleural pressure, and the visco-elastic nature of the lung tissue, any downward shift in the lung parenchyma during 1 or 5.8 G<sub>y</sub> environments should result in compression of the dependent lung and expansion of the superior lung tissue, respectively. A measure of the changes in isotope distribution in the thorax produced by the compressive and expansive effect on different regions of the lungs caused by changes in body position at 1G can be seen on scintigraphs based on replicate determinations of the thoracic distribution of microspheres from replicate scintiscans of the dorsal surface of the thorax carried out when the animal was maintained in the

right and left lateral and prone body positions (figure 9 ). The compressive effects on the dependent lung would narrow that region's spatial distribution of isotope in the vertical direction as well as three-dimensional regional distribution contour along the vertical axis and peak count values, probably with relatively little shift in the isotope deposition pattern in the horizontal direction. The expansive effect on the upper lung would produce the opposite results over this lung region-- that is, broaden the three-dimensional distribution contour along the vertical axis and attenuate the peak count value over this lung. Figure 9 demonstrates that the changes in distribution of microspheres in the thorax produced by relative changes in volume and shape of the right and left lungs associated with the right and left lateral, and prone body positions at 1G are small and probably within the range of error of the scintigraphic techniques.

The A-P roentgenograms obtained during exposures to acceleration indicate, as would be expected, that the relative changes in volume and shape of the two lungs and position of the heart and diaphragm associated with the right and left lateral positions at 1 G<sub>y</sub> are considerably increased during exposures to acceleration in these positions. Since all scintiscans were carried out at 1G following the series of centrifuge exposures, the actual vertical height of the sites of impaction of microspheres in the lungs at the actual time of their injection and embolization in the lungs during exposures to plus or

minus 5.8 G<sub>y</sub> is not known.

The data do, however, show effects of 5.8 G<sub>y</sub> accelerations on the distribution of microspheres in the lungs after their return to their presumably normal shape, volume, and position as they exist in the normal 1G environment in the prone or supine positions. Our interpretation of this evidence, however, indicates that the amount of lung parenchyma shift is not sufficient to effect a 14% relative increase in the flow fraction to the superior lung during accelerative forces, although it may have contributed somewhat to the observed effect.

The hypothesis of an increased vascular resistance in dependent lung vessels appears to be the most tenable explanation for the observed decrease in blood flow to the dependent, lateral regions of the lower lung. Three arguments tend to support this concept: 1) localized low oxygen and/or high carbon dioxide alveolar, pulmonary capillary and venous blood gas tensions in the dependent lateral regions of the lower lung may produce an increase in pulmonary vascular resistance at these sites; 2) perivascular and interstitial edema are known to occur in dependent lung regions, and therefore, may alter interstitial pressures in such a way as to cause a mechanical constriction of the blood vessels (28); and 3) dependent vascular vessels may collapse due to the occurrence of critical closing pressures during low transpulmonary pressure conditions.

Low oxygen and/or high carbon dioxide gas tension during

single lung ventilation, together with normal air ventilation to the opposite lung, has been shown by Arborelius (1) to redistribute blood flow preferentially to the normally respired lung. The intrapleural pressure measurements from this report and elsewhere (14) suggest that a gradient in alveolar size with vertical height in the thorax must be present. Alveoli in superior regions of the thorax are believed to be over-expanded while dependent alveoli are decreased in size and presumably collapse during increased inertial force environments. Glazier (11) has verified such a vertical gradient in alveolar size in rapidly frozen dogs. Milic-Emili (14) and Bryan (6) have also concluded that a vertical gradient in alveolar size is present in the 1G environment and have suggested that dependent lung alveoli ventilate late in the respiratory cycle, with only a minimal amount of air exchange taking place during low tidal volume respirations. Gas analyses from individual lung segments have shown low oxygen and high carbon dioxide gas tensions do exist in dependent lung regions (12,34) and pulmonary venous blood withdrawn from such segments during exposures to 5.8 G have demonstrated that little or no oxygenation of this blood has occurred. The above evidence suggests that an increase in dependent lung vascular resistance may occur because of the low oxygen and high carbon dioxide gas tensions which may be present in these regions of the lungs.

Perivascular edema in inferior lung regions has been suggested by West (28) as a means to explain decreased blood flow to dependent regions of excised lungs. Wayne (26) has shown that perivascular and peribroncheolar edema formation can occur in lung tissue during experimental 8% oxygen ventilation while Staub (22) has shown interstitial edema affects primarily extra-alveolar vessels during its initial formation. Banchemo (3) has reported that an increase in the blood hematocrit is found in blood samples taken from the dependent lung regions during increased inertial force environments, and has suggested a vascular fluid loss in those regions. Wood (30) has reported increases in intrapleural and vascular pressures, during accelerative conditions, sufficient to alter normal hydrostatic-osmotic pressure relationships and cause abnormal intrapleural and vascular fluid movements in the dependent lung regions. Our roentgenographic data during 1 and 5.8  $G_y$  conditions also show decreased x-ray penetration in dependent lung regions which is consistent with interstitial or pulmonary edema. Increased vascular resistance in dependent lung regions as the result of perivascular and interstitial edema is, therefore, also considered plausible.

Critical vascular closing during low transpulmonary pressure conditions has been suggested by Permutt (16) as a mechanism for explaining decreases in dependent lung blood flow in excised canine lungs. His hypothesis indicates that as interstitial pressure approaches zero,



transvessel pressures (i.e., capillary minus interstitial pressure) decreases, allowing the vessel wall to become critically unstable and collapse. During acceleration, dependent lung interstitial pressure most likely becomes less negative, relative to normal gravity conditions, due to the increase in pleural pressure at dependent sites in the thorax associated with the increased weight of the thoracic contents plus the accumulation of edema fluid in the dependent interstitial spaces.

A redistribution of blood flow in the upper lung during  $G_y$  acceleration toward the medial (dependent) regions of this lung, as was generally observed in these animals, would be expected on the basis of hydrostatic effects of the increased weight of the blood on pulmonary intravascular pressures. The effects of the hydrostatic effects on pulmonary vascular transmural pressures are, however, probably minimized to some degree by the concomitant changes in the same direction of pleural pressure and probably interstitial pulmonary pressure in these regions of the lung. Since pulmonary artery pressures are usually somewhat increased at midlung level during  $G_y$  acceleration and left atrial pressure usually unchanged, it would be expected on a hydrostatic basis that blood flow to all regions of the lower lung would be increased. The expected increase to the medial (upper) regions of this lung generally did occur concomitantly with the decrease in flow to the dependent region of this lung observed in most animals. The resulting upward displacement of blood-flow distribution toward the midline was apparently the

result of a selective increased resistance to blood flow limited to the dependent regions of this lung and of a magnitude great enough to overcome the dependent increase in perfusion pressure produced by the acceleration.

#### Blood Oxygen Saturation

The blood oxygen saturation changes observed in these chimpanzees during exposure to  $G_y$  accelerations of 5.8 G are similar to changes observed in dogs (24) and humans (33). A biphasic change in arterial oxygen saturation was usually observed during exposure to plus or minus  $G_y$  acceleration. A rapid decrease occurred shortly after the onset of acceleration due to a sudden increase in the magnitude of the physiological shunt. The magnitude of this calculated shunt usually decreased during the last 10-20 seconds of the 60-70 second exposures so that no further decrease or some recovery of the arterial oxygen saturation occurred. These changes in arterial oxygen saturation are believed to result from the dependent pulmonary arterial-venous shunt caused by collapse of the alveolar ducts and/or alveoli at the onset of the exposure. A marked increase in pulmonary vascular resistance in these regions of the lungs apparently then occurs which tends to shift blood flow upward in the thorax away from the nonaerated dependent lung regions toward the essentially normally ventilated regions of the lung in the midregion of the thorax so that some recovery of arterial oxygen saturation may occur.

A rapid recovery of arterial oxygen saturation toward normal levels occurred after cessation of centrifugation followed by a slower, prolonged return to its preacceleration baseline. These biphasic responses are consistent with the data reported by Vandenberg (24) and Barr (4).

#### Pleural Pressure Relationships

Pleural pressures measured at right and left lateral sites varied with body position and acceleration in the same manner as reported previously by this laboratory for dog experiments (21). Both chimpanzee and canine studies support the concept that regional variations in pleural pressures are related to the weight of thoracic contents.

## APPENDIX

The average temporal profile of exposures to acceleration during these studies is given in table XI. The centrifuge was accelerated from 0 to 15 revolutions per minute (1.5G) in about 5-6 seconds; the acceleration then built up at about 1G per second until the plateau level of acceleration was attained. The plateau level was maintained within  $\pm 0.1G$  for periods somewhat longer than one minute (range: 67-85 seconds). The exposure to 5.8G, when breathing 99.6% oxygen, was prolonged until a clear-cut decrease in arterial oxygen saturation, being calculated and displayed on-line via the computer, was observed. The maximum duration of an exposure to 5.8G under this circumstance was 130 seconds.

TABLE XI

AVERAGE TEMPORAL PROFILE OF EXPOSURES TO ACCELERATION DURING  
WHICH CHANGES IN BLOOD OXYGEN SATURATION WERE DETERMINED

Plateau Level Of Acceleration	Onset Time (seconds)	Time at Plateau (seconds)	Decay Time (seconds)
2.9 G	7.3 (5-8)	66 (62-71)	7.3 (7-8)
5.8 G	10 (9-11)	73 (62-92)	9.5 (8-11)

## References

1. Arborelius, Mans, Jr. Influence of unilateral hypoventilation on distribution of pulmonary blood flow in man. J Appl Physiol 26:101-103 (1969).
2. Ball, W. C., Jr., et al. Regional pulmonary function studied with xenon. J Clin Invest 41(3):519-531 (1962).
3. Banchemo, N., et al. Effect of transverse acceleration on blood oxygen saturation. J Appl Physiol 22:731-739 (1967).
4. Barr, P. O. Hypoxemia in man induced by prolonged acceleration. Acta Physiol Scand 54:128-137 (1962).
5. Bryan, A. C., et al. Effect of acceleration on the distribution of pulmonary blood flow. J Appl Physiol 20(6):1129-1132 (1965).
6. Bryan, A. C., J. Milic-Emili, and D. Pengelly. Effect of gravity on the distribution of pulmonary ventilation. J Appl Physiol 21:778-784 (1966).
7. Comroe, J. H., Jr., et al. The lung; clinical, physiological, and pulmonary function tests, pp. 343-345. Second edition, Chicago Year Book, 1962.
8. Coulam, C. M., W. Dunnette, and E. H. Wood. A computer-controlled scintiscanning system and associated computer processing techniques for study of regional distributions of blood flow. J Nucl Med. (In press)

9. Coulam, C. M., J. Greenleaf, and W. Dunnette. Gaussian functions for design and comparison of digital filters from scintiscan data for display and study of the spatial distribution. J Nucl Med. (In press)
10. Dow, P. Estimations of cardiac output and central blood volume by dye dilution. Physiol Rev 36:77 (1956).
11. Glazier, J. B., et al. Vertical gradient of alveolar size in lungs of dogs frozen intact. J Appl Physiol 23(5):694-705 (1967).
12. Hugh-Jones, P., and J. B. West. Detection of bronchial and arterial obstructions by continuous gas analysis from individual lobes and segments of the lung. Thorax 15:15-64 (1960).
13. Iinuma, T. A., T. Nagi, and N. Fukuda. Digital data processing and display in radioisotope imaging. Symposium on Medical Radioisotope Scintigraphy, Salzburg, Austria, August 1968.
14. Milic-Emili, J., et al. Regional distribution of inspired gas in the lung. J Appl Physiol 21(2):749-759 (1966).
15. Nolan, A. C., et al. Decreases in arterial oxygen saturation and associated changes in pressures and roentgenographic appearances of the thorax during forward (+G<sub>x</sub>) acceleration. Aerospace Med 34:797-813 (1963).
16. Permutt, S. Respiration. In Physiology in the Space Environment, Vol. II, pp. 38-56. Washington, D. C.: Natl Acad Sci Natl Res Council, 1967.

17. Reed, J. H., Jr., and E. H. Wood. Effect of body position on regional distribution of pulmonary blood flow. J Appl Physiol. (In press)
18. Reed, J. H., Jr., and E. H. Wood. Effect of gravitational and inertial forces on regional distribution of pulmonary blood flow. J Appl Physiol. (Submitted)
19. Ring, G. C., et al. Size of microspheres passing through pulmonary circuit in the dog. Amer J Physiol 200(6):1191-1196 (1961).
20. Rudolph, A. M., and M. A. Heyman. The circulation of the fetus in utero. Circ Res 21:163 (1967).
21. Rutishauser, W. J., et al. Effect of gravitational and inertial forces on pleural and esophageal pressures. J Appl Physiol 22:1041-1052 (1967).
22. Staub, N. C., H. Nagano, and M. L. Pierce. Pulmonary edema in dogs, especially the sequence of fluid accumulation in lungs. J Appl Physiol 22(2):227-240 (1967).
23. Tow, D. E., et al. Validity of measuring regional pulmonary arterial blood flow with macroaggregates of human serum albumin. Amer J Roentgen 96:664-676 (1966).
24. Vandenberg, R. A., et al. Regional pulmonary arterial-venous shunting caused by gravitational and inertial forces. J Appl Physiol 25(5):516-527 (1968).



25. Wagner, H. R., Jr., et al. Regional pulmonary blood flow in man by radioisotope scanning. JAMA 187:601-603 (1964).
26. Wayne, T. F., Jr., and J. W. Severinghaus. Experimental hypoxic pulmonary edema in the rat. J Appl Physiol 25(6):729-732 (1968).
27. West, J. B. In Ventilation/Blood Flow and Gas Exchange. Oxford: Blackwell Scientific Publications, 1965.
28. West, J. B., C. T. Dollery, and B. E. Heard. Increased pulmonary vascular resistance in the dependent zone of the isolated dog lung caused by peri-vascular edema. Circ Res 17(3):191-206 (1965).
29. Williams, J. C. P., T. P. B. O'Donovan, and E. H. Wood. A method for the calculation of areas under indicator-dilution curves. J Appl Physiol 21:695-699 (1966).
30. Wood, E. H., et al. Technics for measurement of intrapleural and pericardial pressures in dogs studied without thoracotomy and methods for their application to study of intrathoracic pressure relationships during exposure to forward acceleration (+G<sub>x</sub>). AMRL-TDR-63-107, 1963.
31. Wood, E. H., R. E. Sturm, and J. J. Sanders. Data processing in cardiovascular physiology with particular reference to roentgen videodensitometry. Mayo Clin Proc 39:849-865 (1964).
32. Wood, E. H., W. F. Sutterer, and L. Cronin. Oximetry. In Glasser, O. (ed.) Medical Physics, Vol 3, pp. 416-445. Chicago Year Book, 1960.

33. Wood, E. H., et al. Effect of headward and forward accelerations on the cardiovascular system. WADD Technical Report 60-634, (Jan) 1961.
34. Zardini, P., and J. D. West. Topographical distribution of ventilation in isolated lung. J Appl Physiol 21(3):794-802 (1966).

(♀ Chimpanzee 39 kg, Sernylan-Pentobarbital Anesthesia)

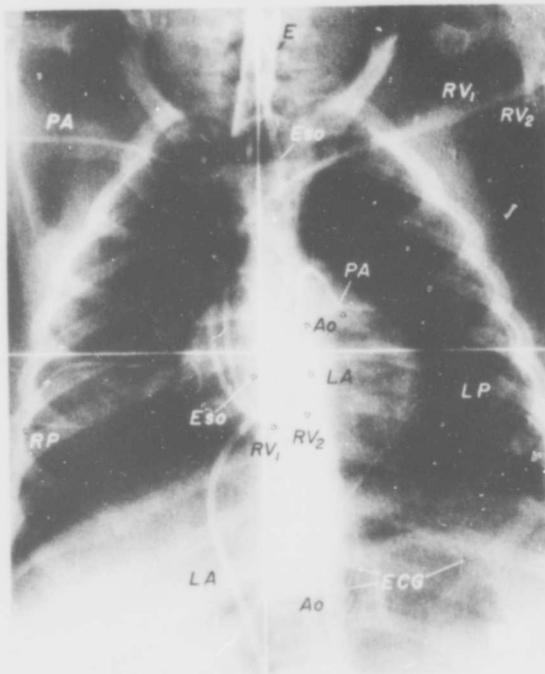


FIGURE 1

Anterior-posterior (A-P) roentgenogram of the thorax of female chimpanzee F, showing location of catheters for recording pleural and intrathoracic circulatory pressures during exposures to  $G_y$  acceleration on a centrifuge. Definition of symbols follows:  $RV_1$  and  $RV_2$  - cardiac catheters with tips positioned in the right ventricular outflow tract and used for injections of indocyanine green dye and isotope-tagged microspheres for determination of the cardiac output and distribution of pulmonary blood flow, respectively; PA -

cardiac catheter with tip positioned in pulmonary artery for pressure recordings; Eso -esophageal catheter; RP and LP - pleural catheters with tips positioned at the right and left lateral margins of the lungs, respectively, for pressure recordings; LA -catheter introduced transseptally into left atrium from right femoral vein; Ao -aortic catheter. Wires at bottom margin of thorax are external electrocardiographic leads.

This roentgenogram was taken between the series of exposures to  $+G_y$  acceleration during the process of changing the animal from left lateral to the right lateral half-body casts used to support and maintain the body position of the chimpanzee constant in the centrifuge cockpit. The animal had been anesthetized for 11 hours at the time of the roentgenogram.

( ♀ CHIMPANZEE 39 kg. SERNYLAN - PENTOBARBITAL ANESTHESIA )

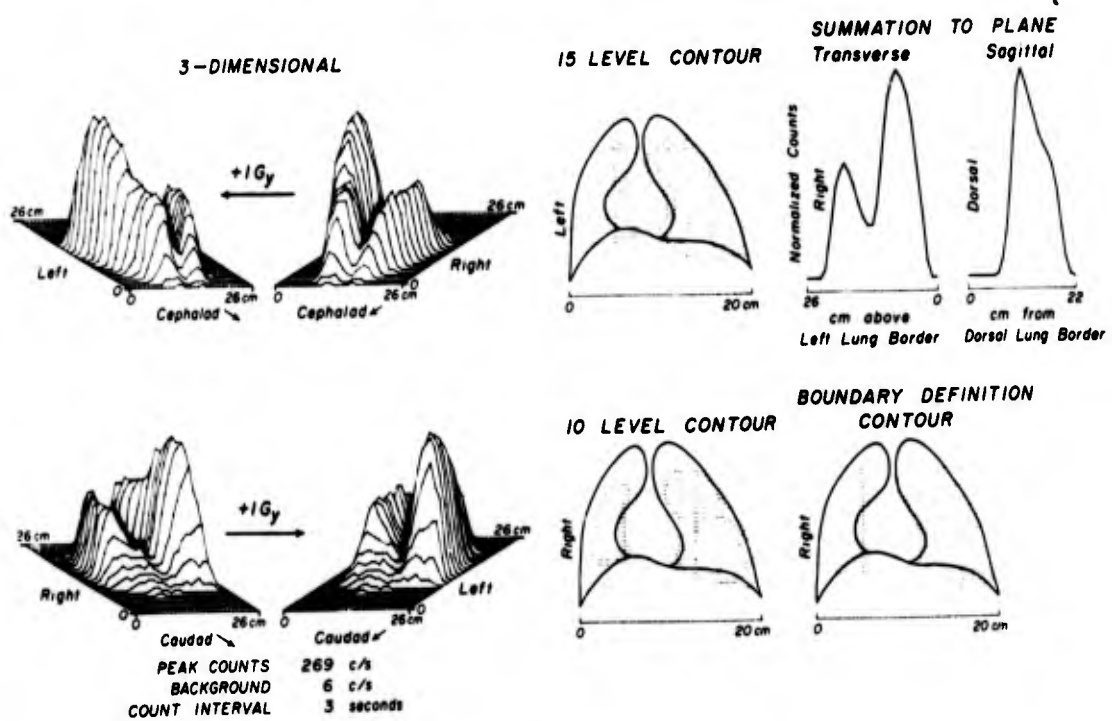


FIGURE 2

Computer-generated displays of radiation levels recorded during scintiscan of the ventral surface of the thorax of female chimpanzee F following injection of tagged microspheres into the right ventricle when in the left lateral position.

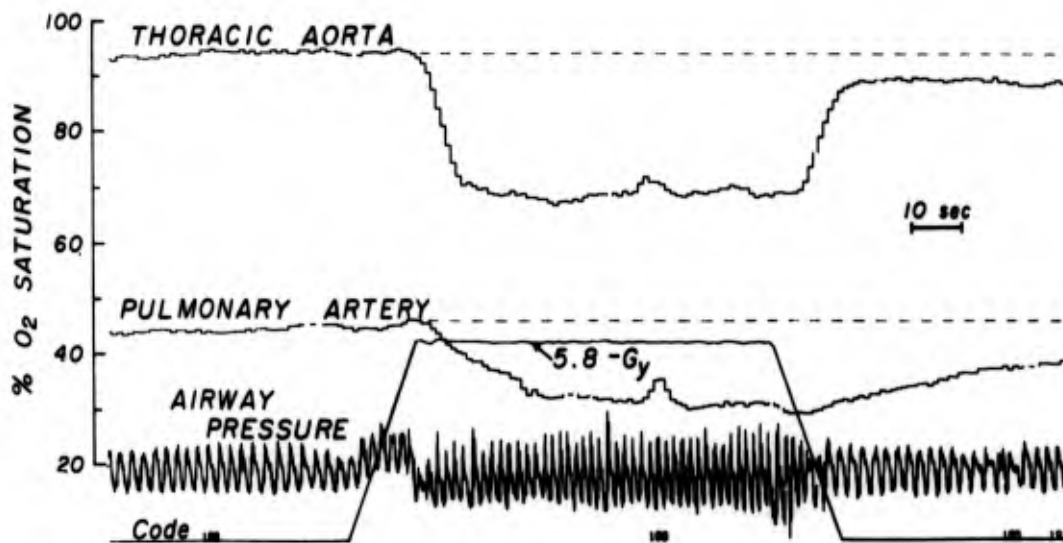


FIGURE 3

Computer-generated plot of changes in oxygen saturation of systemic arterial and mixed venous (pulmonary artery) blood plus respiratory rate and tidal volume in chimpanzee F during a 69-second exposure to an acceleration of  $-5.8Gy$ . The original photokymographic recordings of changes in red and infrared transmission of the blood, from which this plot was derived, are shown in figure 4. The time lag in the changes in oxygen saturation recorded by the cuvette oximeters has been approximately corrected for on the basis of the volume of the dead space of the respective catheter-oximeter sampling systems and the flow rate through these systems. Note that the minimum values of arterial oxygen saturation occurred approximately 20 seconds after the onset of the plateau level of acceleration in spite of the fact the saturation of the mixed venous blood continued to decrease.

Therefore, the calculated magnitude of the physiologic pulmonary arterial-venous shunt was decreasing during the last approximately 40-50 seconds of the exposure possibly due, at least in part, to redistribution of pulmonary blood flow away from the lateral (most dependent) region of the lower lung where evidence from dogs indicates no oxygenation (i.e., 100% shunting) of pulmonary arterial blood occurs during exposure to these levels of Gy acceleration. The transient increases in saturation at code 189 are artifactual and result from the injection of microspheres followed by 8 milliliters of saline for determination of the distribution of pulmonary blood flow marked by code 189 and S<sub>2</sub> in figures 4 and 5.

(♀ CHIMPANZEE, 39kg, SERNYLAN-PENTOBARBITAL ANESTHESIA)

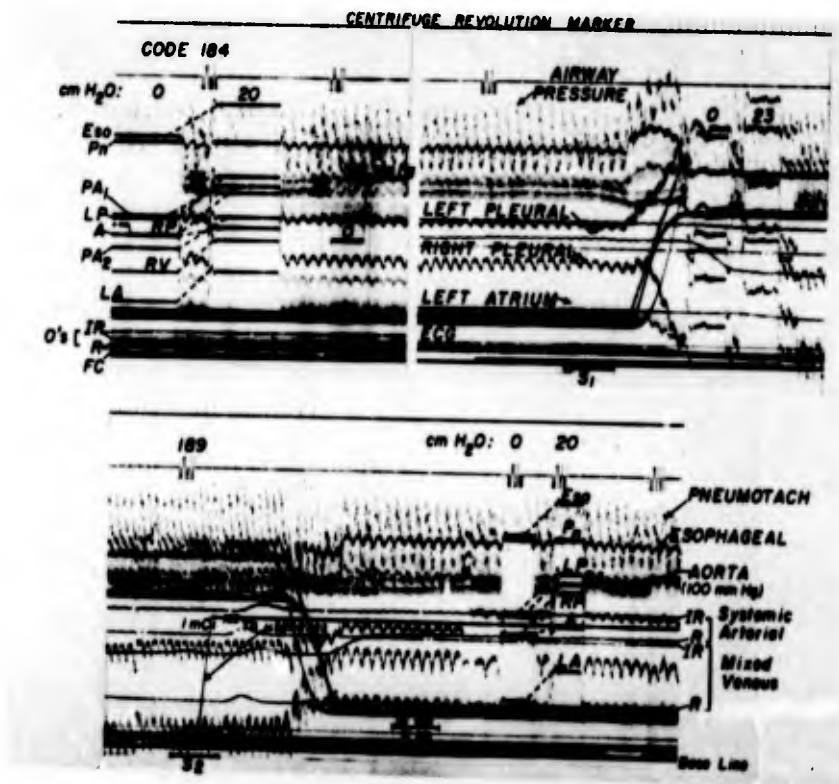


FIGURE 4

Original photokymographic recording of multiple physiologic variables before and during an exposure of chimpanzee F to acceleration of  $-5.8 G_y$  for 69 seconds.

The recording of the binary decimal codes 184 and 185 during the calibration of the manometer systems at 0 and 20 cm of water and the aortic system (A) at 100 mm of mercury (left upper panel), and codes 188 through 192 during the continuous recording encompassing the exposure shown in the right upper panel and continued on the lower panel, serve to identify different events on the recording and to synchronize



these events in the parallel recordings on magnetic tape and on the fast camera. The periods when fast camera records (paper speed 25 mm/second) were obtained are indicated by the black line labelled FC just above the baseline. The abbreviations identifying the various tracings are as follows: Eso -esophageal pressure; Pn - pneumotachygram; PA<sub>1</sub> -pulmonary artery pressure 1; LP -left pleural pressure; RP -right pleural pressure; A -aortic pressure; PA<sub>2</sub> -pulmonary artery pressure via the second pulmonary artery catheter (this catheter was for sampling of mixed venous blood prior to, during, and after the period of centrifuge rotation); RV -right ventricular pressure (via catheter used for injection of microspheres); LA -left atrial pressure; IR and R in the left upper panel indicate the mechanical zero; i.e., zero transmission level of the red and infrared cells of the cuvette oximeters used to continuously record the transmission of red and infrared light of systemic arterial and mixed venous blood from which blood oxygen saturation values were calculated (see figure 3). The numerals 0 and 23 in the right upper panel indicate the periods when the zero-reference levels (thistle-tube zeroes) of the manometers were recorded (and their relative sensitivities to a pressure of 23 cm of water were checked) when the centrifuge was rotating at an average speed of 34 RPM and the centrifuge cockpit was tilted outward to 76° so that the resultant 5.8 G vector

of the gravitational-centripetal force was perpendicular to the floor of the cockpit.

The injection of microspheres tagged with 1 milli-curie of  $^{169}\text{Yb}$ , at S2 in the lower panel, is indicated by the record of the travel of the piston of the remotely activated syringe used to displace the suspended bolus of microspheres into the right ventricle by a trailing high-speed injection of 8 ml of Ringer's solution. Note the increased transmission of red and infrared light recorded in the mixed venous and arterial blood due to the transient dilution caused by this injection. The zero baselines of the manometer systems and their sensitivities were rechecked, as indicated by the numbers approximately 30 seconds after the period of centrifuge rotation.

Sections of the original fast camera recordings taken during the periods indicated by S1, just before the onset of centrifuge rotation, and S2 at 5.8 G during the injection of the microspheres are shown in left upper and lower panels of figure 6, respectively.

This type of photokymographic recording is useful for monitoring the overall function of the recording systems and associated physiologic events. However, detailed measurements generally cannot be made from this recording because of the slow paper speed coupled with overlap and crossover of the multiple tracings.

HEART RATE = 195  
RESP RATE = 40  
GR = 5.0000

SET NO: 6  
-6.42 SECONDS FROM CODE MEAN

	MEAN	NO OF SAMPLES	LOW	HIGH	STANDARD DEVIATION	STANDARD ERROR OF MEAN
AORTA SYST EXP	102	0	100	105	1.7320	.7071
AORTA MEAN EXP	84	0	83	86	1.0000	.4002
AORTA DIAS EXP	76	0	75	77	1.0000	.4002
PA SYST EXP	33	0	32	37	2.0000	.6309
PA MEAN EXP	20	0	19	22	1.0000	.4002
PA DIAS EXP	14	0	13	15	1.0000	.4002
PLEURAL 1 EXP	-59	0	-50	-59	.0000	.0000
PLEURAL 2 EXP	-26	0	-27	-27	1.0000	.4002
PLEURAL 3 EXP	-38	0	-41	-37	1.7320	.7071
RA MEAN EXP	3	0	3	3	.0000	.0000
ESOPHAGEAL EXP	20	0	20	20	.0000	.0000

ZERO AD: 182 PA: 302 PL1: 486 PL2: 449 PL3: 458 RA: 911 ESO: 911 G: 9.86  
 PLEVEL AD: 337 PA: 915 PL1: 953 PL2: 939 PL3: 929 RA: 911 ESO: 911  
 CON PL1: 0 PL2: -9 PL3: 0 ESO: -0 AD: 0 PA: 0 RA: 0  
 QCON PL1: 47 PL2: -99 PL3: -1 ESO: -20 AD: -2 PA: -3 RA: -3

PL1 GPL1 PL2 GPL2 PL3 GPL3 ESO GESO  
 SP -0 -12 -4 -19 0 0 0 0  
 YP 115 100 -114 -121 0 0 -6 -41  
 Y 89 84 -89 -93 0 0 -9 -32  
 TT: 3 HL: 3 GPL: -4 P: 1000 PP: 1000 S: 220 SP: 220

	MEAN	NO OF SAMPLES	LOW	HIGH	STANDARD DEVIATION	STANDARD ERROR OF MEAN
AORTA SYST EXP	100	0	98	103	1.7320	.7071
AORTA MEAN EXP	82	0	81	84	1.0000	.4002
AORTA DIAS EXP	74	0	73	75	1.0000	.4002
PA SYST EXP	30	0	29	34	2.0000	.6309
PA MEAN EXP	17	0	16	19	1.0000	.4002
PA DIAS EXP	11	0	10	12	1.0000	.4002
PLEURAL 1 EXP	-12	0	-12	-12	.0000	.0000
PLEURAL 2 EXP	-29	0	-30	-28	1.0000	.4002
PLEURAL 3 EXP	-39	0	-42	-38	1.7320	.7071

FIGURE 5

Portions of computer-printed data to show the results of on-line analysis of physiologic data obtained during the exposure of chimpanzee F to an acceleration of -5.8 Gy. Photokymographic recordings of the variables obtained during this same centrifuge run are shown in figures 4 and 6. The three types of data sets obtained by computer analysis of pressures recorded continuously during a centrifuge exposure are illustrated by the portions of three computer-printed pages included in this composite photograph.

The data set in the upper third of the figure show the level of acceleration, average values of heart rate and respira-

tion, and average values of end-expiration aortic, pulmonary artery, pleural, esophageal, and right atrial pressures. End-inspiration pressures are normally computed also and printed in the same format on the same page, but were not included in the figure. These averages are computed from consecutive ten-second periods of a digital tape recording obtained by real-time analog-to-digital conversion of 22 channels of analog data at a sampling rate of 100 per second for each channel. The physiologic data include vascular, pleural, and esophageal pressures throughout the centrifuge run, including the control periods immediately before and after the acceleration plateau. The pressure data in this figure pertain to one such ten-second interval indicated by S<sub>2</sub> in figure 4, during the period in the acceleration plateau when the injection of microspheres was carried out.

The pressure data tabulated in the upper third of this figure have been corrected by the computer as follows: pleural and esophageal pressures were adjusted to catheter tip level by subtracting the hydrostatic pressure head between each catheter tip and the midlung zero reference level measured from the roentgenogram of the thorax obtained during this exposure and shown in figure 20. Vascular pressures were referred to midlung level by subtracting the hydrostatic pressure head between the midlung and the height of the menisci of the zero-reference thistle tubes determined from the lateral roentgeno-

gram (fig. 20) and an anterior-posterior roentgenogram obtained in a subsequent exposure to the same level of acceleration.

The similar data set in the lower third of this figure are average end-expiration pressures computed during the same ten-second period, but corrected only for the shift in the baseline of each manometer with acceleration; i.e., the individual baselines during the acceleration period were adjusted by the computer to the baselines recorded when the manometers were connected to the thistle-tube system at the start of the acceleration plateau, as shown in figure 4.

The center third of this figure shows all of the factors used in referring the vascular pressures to the midlung level, and to correct the pleural and esophageal pressures to their respective catheter-tip positions, during the control and acceleration periods. The coordinates of each catheter tip ( $X_p$ ,  $Y_p$ ), the vertical distance between the midlung and reference axis during the control (ML) and acceleration plateau (GML), and the height of the fluid level in the thistle-tube system above or below the reference axis (TT), all determined from roentgenograms, are tabulated. X-ray magnification factors are computed from the source to plate (P, PP) and midlung to plate (S, SP) distances for A-P and lateral roentgenograms, respectively. The distance between catheter tip and reference axis, corrected for x-ray magnification, for the pleural and

esophageal catheters are shown in the row labeled Y. The rows labeled COR and GCOR are pressure corrections (computed from the values for TT, ML, GML, and GR) which are subtracted algebraically from the uncorrected pressures to produce the corrected pressure data such as illustrated in the upper part of this figure. For example, the pressure recorded from the pleural 1 catheter (left, in this example) is corrected to the catheter-tip level and corrected for the effects of acceleration by subtracting 47 cm water (GCOR, PL1) from 12 cm water, the value for pleural 1 shown in the lower data group, resulting in 59 cm water as shown in the upper data group. If the analysis had pertained to control (1G) measurements instead, the correction factors shown in the row labeled COR would have been used.

The rows labeled ZERO and P LEVEL are A-D converter values corresponding to zero and 100-mm Hg calibration pressures for the aortic, and zero and 20 cm of water calibration pressures, respectively, for all other manometers. In this particular experiment, only two pleural catheters were placed (Pleural 1, in the left pleural space, and Pleural 2, in the right), and the right atrial and esophageal pressures were not digitized. This is indicated by the A-D level value of 511, corresponding to zero pressure, printed in the ZERO and P LEVEL rows. Values shown for these pressures elsewhere in this figure should, therefore, be ignored.

Each of the three data sets shown in this figure are normally printed on successive 11-inch x 15-inch pages of standard computer printer paper. The page containing the calibration and correction factors is printed once at the start of each analysis, followed by approximately 30 pages of pressure data (depending upon the duration of the centrifuge run), corresponding to the approximately 20, ten-second analysis periods which encompass the control period, the period of centrifuge rotation, and the recovery period associated with a 60-second exposure to a plateau acceleration level of 5.8G. Each page of pressure data is identified by a set number, the time relative to the nearest record identification code, the date of the study, and the time of day that the recording associated with this particular centrifuge was begun.

Two computer analyses are normally performed for each centrifuge exposure. One analysis is performed in the five- to ten-minute period between centrifuge runs. The x-ray measurements necessary for the pressure corrections are unknown at that time so that zeros are entered into the computer for values of ML, BML, and TT, and for the Xp, Yp coordinates and each catheter tip. The data sets which are printed between centrifuge runs correspond, therefore, to the data set illustrated in the lower third of this figure. After the x-ray measurements are determined, usually several days after the study is completed, the values are entered and the analysis is repeated

using the original digital tape. Corrected pressures are obtained, such as illustrated in the upper data set of this figure. However, since vascular pressure corrections are usually small, the vascular pressure data in the immediate printout is similar to the corrected pressures. Some results from each experiment are, therefore, available soon after each experiment is completed, and on the basis of these results, succeeding experiments can be modified as necessary.

The set of data shown in this figure is based on the computer-processed photokymographic recordings shown in figure 6. The uncorrected pressures in this figure are, thus, the computer averaged pressures for the ten-second traces shown in the lower center panel of figure 6; and similarly, the corrected pressures in this figure correspond to the ten-second traces shown in the lower right panel of figure 6.



( 9 CHIMPANZEE 39kg SERNYLAN-PENTOBARBITAL ANESTHESIA)

COMPUTER OUTPUT

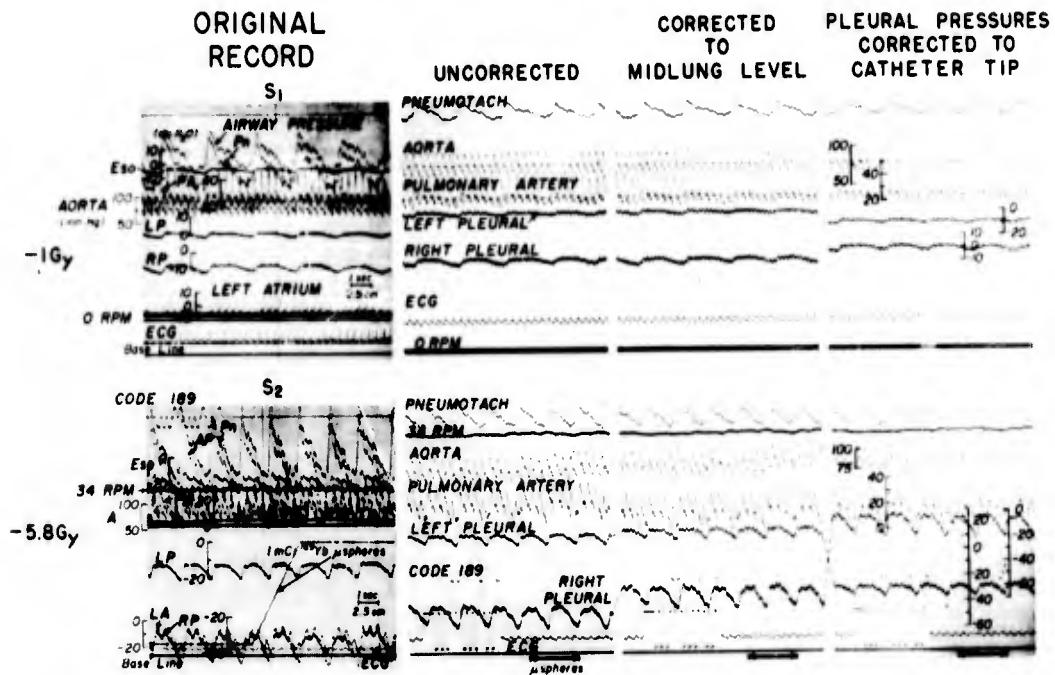


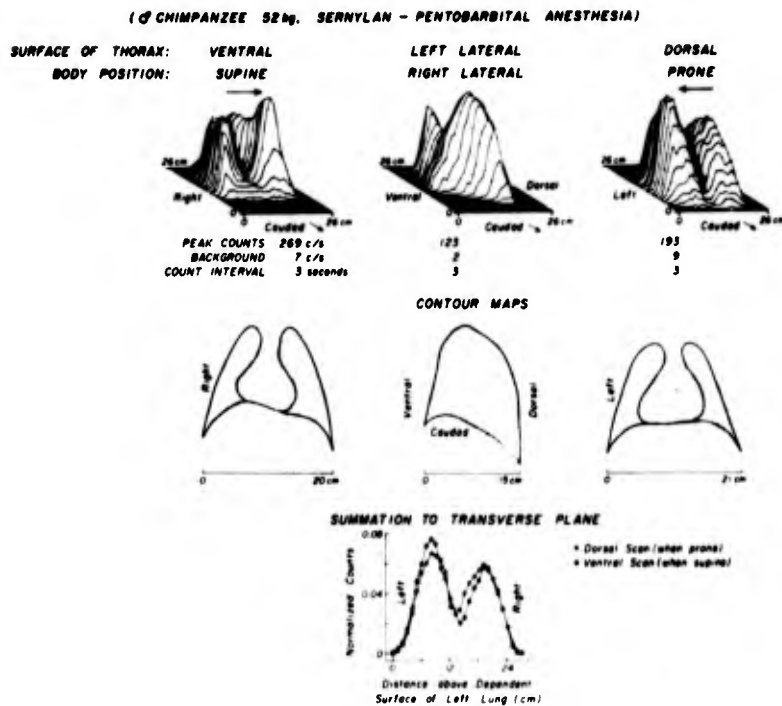
FIGURE 6

Illustration of computer processing of on-line recordings of multiple physiologic variables during exposure of chimpanzee to an acceleration of  $-5.8 G_y$ . The sections of 25 mm/second photokymographic recordings of multiple physiologic variables are from periods before and during the same exposure to  $-5.8 G_y$  during which the 5 mm/second recording shown in figure 4 was obtained.

The periods at  $-1 G_y$  and during the exposure to  $-5.8 G_y$  when the original recordings, shown in the left upper and lower panels respectively, were obtained are indicated by the durations of the lines labelled S1 and S2 in figure 4.

The subsequent panels are computer-generated replays from parallel recordings of the same data made on digital tape after conversion from analog to digital form and inputted on-line to the computer. During subsequent detailed analysis the digitized data were converted back to analog form and the photokymographic recording made. The panels labeled "uncorrected" are used to check the validity of the multichannel A-to-D and D-to-A conversion assemblies. The recordings in the panel labeled "corrected to the midlung level" (third panels) have been corrected by the computer to the midlung zero-reference level based on the thistle-tube zero recordings at -1 and -5.8 Gy shown in figure 4 plus manual measurements from thoracic roentgenograms (figure 20). Additional correction of pleural pressures to the vertical level of the catheter tips in the thorax measured from roentgenograms obtained in the two conditions are included in the right panels. The simultaneously recorded code numbers (e.g., 189 in the lower panels) were time-shared in the ECG for input into the computer in order to conserve data channels.





**FIGURE 8**

Comparison of distribution of pulmonary microsphere emboli determined by scintiscans of ventral, left lateral, and dorsal surfaces of the thorax of male chimpanzee E following right ventricular injection of microspheres when in the left lateral (+1G<sub>y</sub>) position. Note that the results obtained by scans of the ventral and dorsal surfaces of the thorax were closely similar.

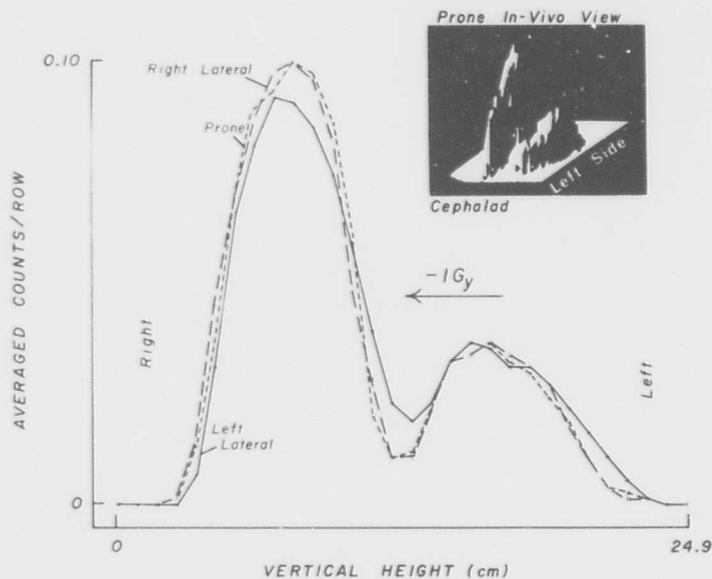
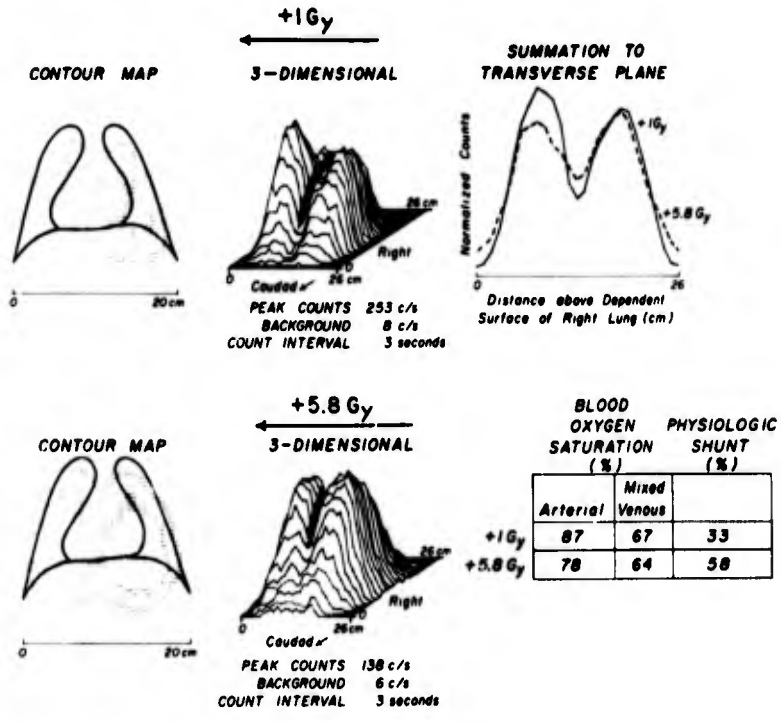


FIGURE 9

Comparison of determinations of the distribution of pulmonary microsphere emboli in the thorax of female chimpanzee F. The microspheres, which were tagged with strontium-85, were injected into the right ventricle when the chimpanzee was in the right lateral position at 1G. These plots of their vertical distribution in the chest are based on successive scintiscans of the dorsal surface of the thorax when the chimpanzee was maintained in the right lateral, the left lateral, and prone body positions. The insert is a photograph of a computer-generated three-dimensional oscilloscopic display of the set of data from the scintiscan carried out in the prone position. Note that the body position in which the scintiscans were made had relatively little effect on the pattern of distribution of the emboli in the thorax.

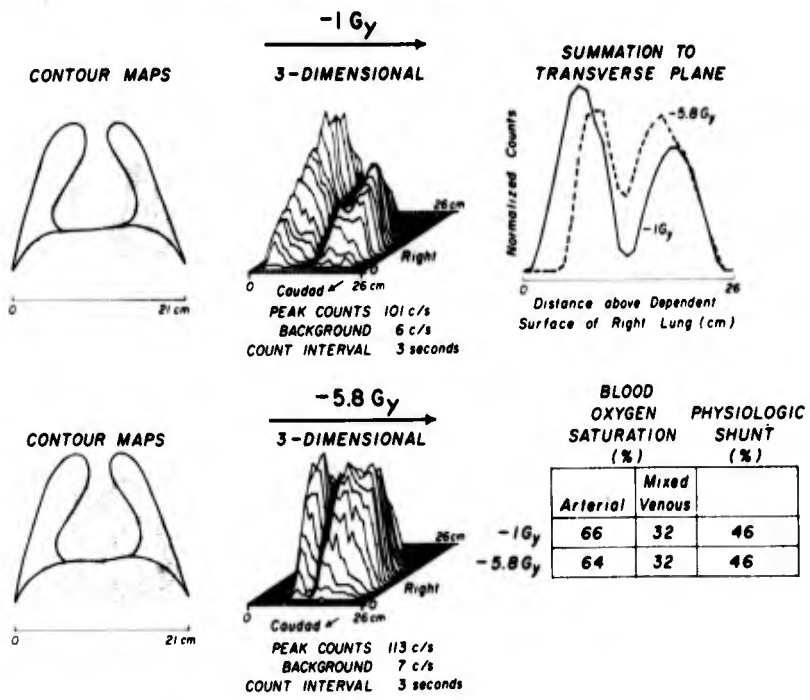
(♂ CHIMPANZEE 52 kg, SERNYLAN-PENTOBARBITAL ANESTHESIA)

**A<sub>1</sub> LEFT LATERAL POSITION**



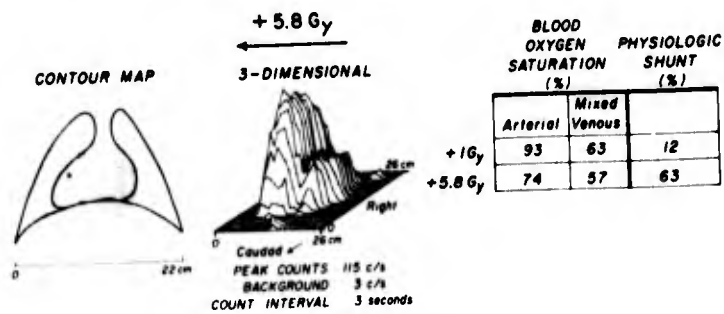
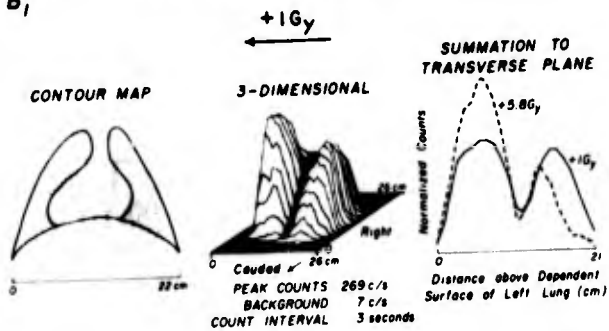
(♂ CHIMPANZEE 52 kg, SERNYLAN-PENTOBARBITAL ANESTHESIA)

**A<sub>2</sub> RIGHT LATERAL POSITION**



( ♀ CHIMPANZEE 39kg. SERNYLAN - PENTOBARBITAL ANESTHESIA )

**B<sub>1</sub>** LEFT LATERAL POSITION



( ♀ CHIMPANZEE 39kg. SERNYLAN - PENTOBARBITAL ANESTHESIA )

**B<sub>2</sub>** RIGHT LATERAL POSITION

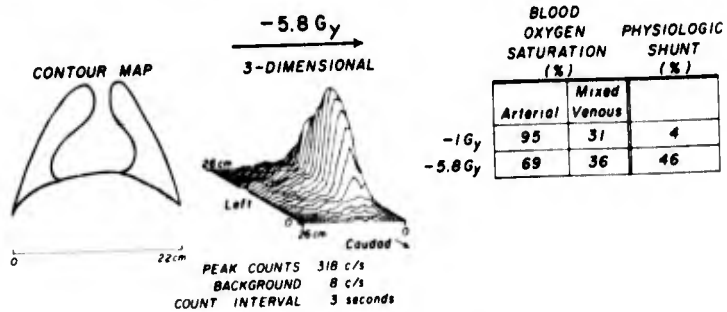
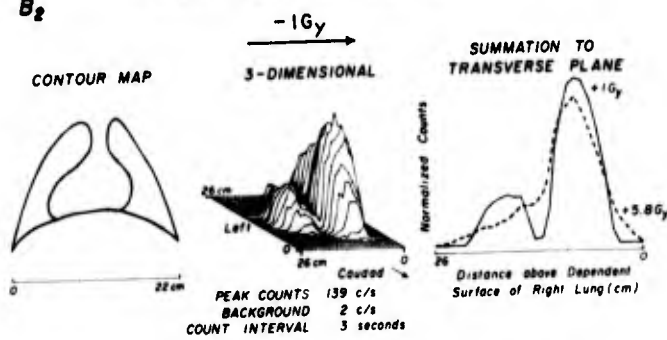


### FIGURE 10

Distribution of microsphere emboli in the thorax of male chimpanzee E at +1Gy and +5.8Gy in the left lateral position (A<sub>1</sub>), and -1Gy and -5.8Gy in the right lateral position (A<sub>2</sub>). Distribution of microsphere emboli in the thorax of female chimpanzee F under the same conditions is shown in B<sub>1</sub> and B<sub>2</sub>. The tabular inserts in each figure give the oxygen saturation of systemic arterial and mixed venous (pulmonary arterial) blood and the calculated physiologic pulmonary arterial venous shunts which were present at the times of each microsphere injection when at 1Gy and during the last 15-20 seconds of 60-second exposures to 5.8Gy.

Note that the fraction of blood flow to the superior lung of chimpanzee E, when at 1Gy, was relatively large and that relatively little displacement of blood flow to the dependent lung was demonstrated during the exposures to 5.8Gy (Panels A<sub>1</sub> and A<sub>2</sub>). This was associated with the presence of relatively large pulmonary arterial-venous shunts at 1Gy in this animal and possibly a selective increase in resistance to blood flow in the anoxic regions of the dependent lung via which such shunts have been demonstrated to occur.

In contrast, the physiologic pulmonary arterial-venous shunts at 1G in chimpanzee F were small, the blood flow to the dependent, presumably nonanoxic, lung relatively large, and considerable displacement of blood flow to the dependent lung occurred during the exposures to 5.8Gy (Panels B<sub>1</sub> and B<sub>2</sub>).



( ♀ Chimpanzee 39 kg, Sernylan - Pentobarbital Anesthesia )

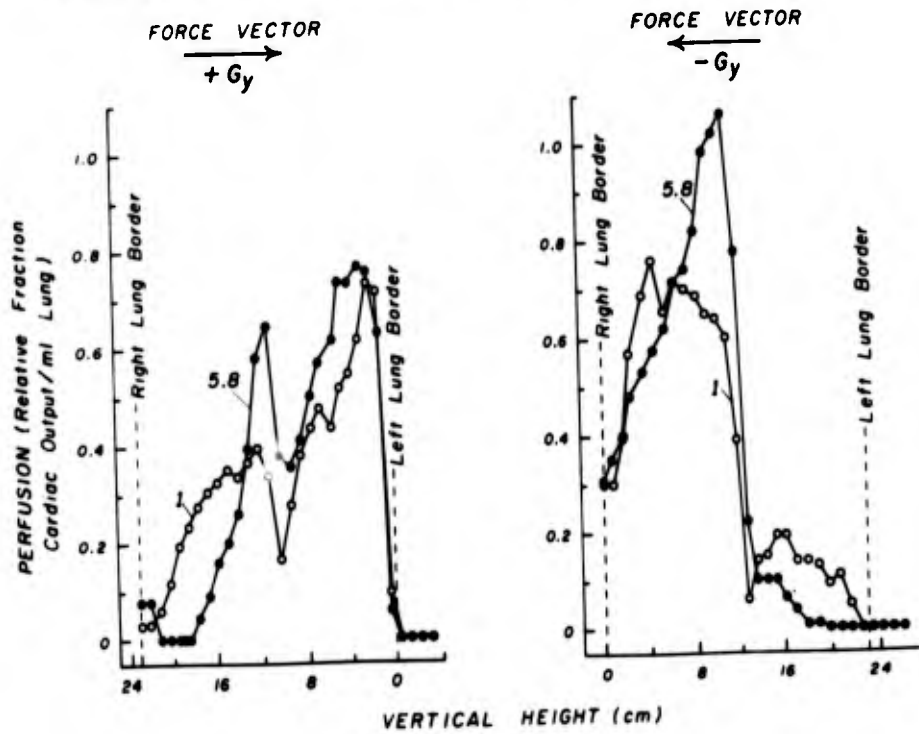


FIGURE 11

Variation in the relative blood flow per milliliter of lung tissue with the vertical height in the thorax of female chimpanzee F during exposure to Gy acceleration. These plots are based on scintiscans of 2-cm-thick cross sections covering the complete lungs of this chimpanzee. The lungs were dried in air while inflated to 40 cm of water and then embedded en bloc in urethane foam prior to the section process, as described in Section III of this report.

Note the similarity in distributions of blood flow determined in this animal by the scintiscans of the thorax carried out in vivo (figure 10 B<sub>1</sub>, B<sub>2</sub>), and the scintiscans of equal volumes of the cross sections of the lungs shown in this figure.

(♀ CHIMPANZEE 39kg, SERNYLAN-PENTOBARBITAL ANESTHESIA)

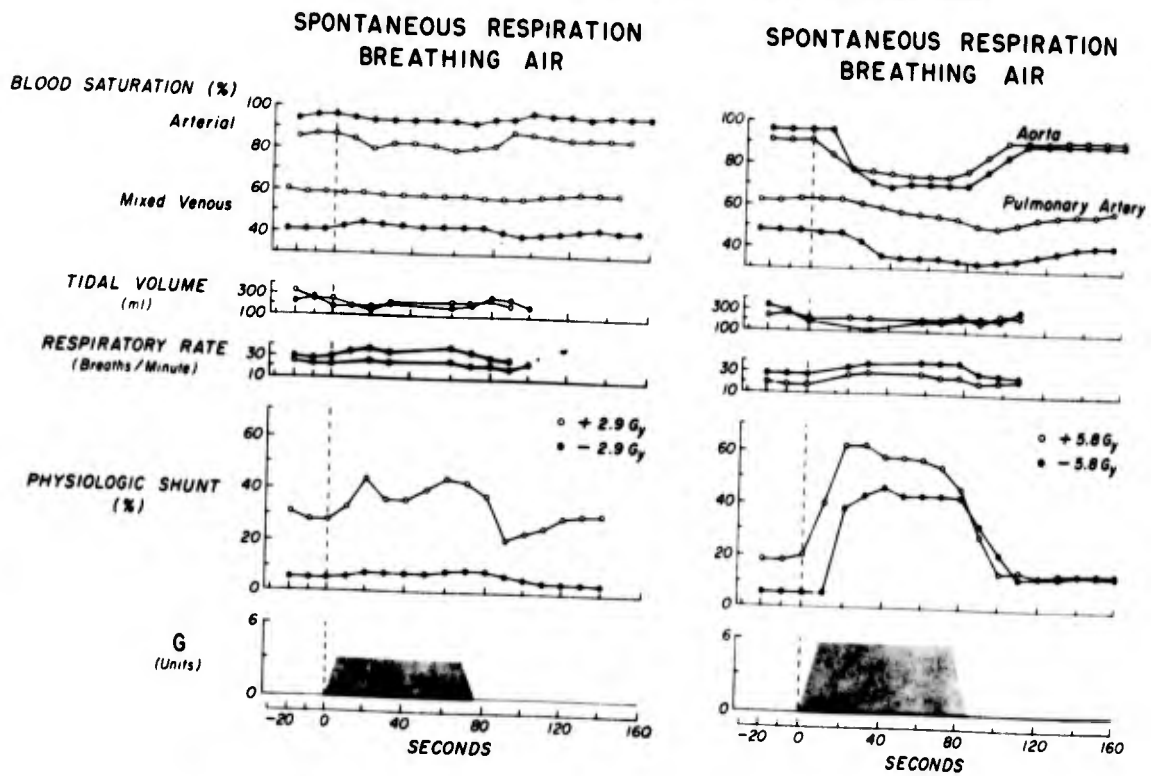
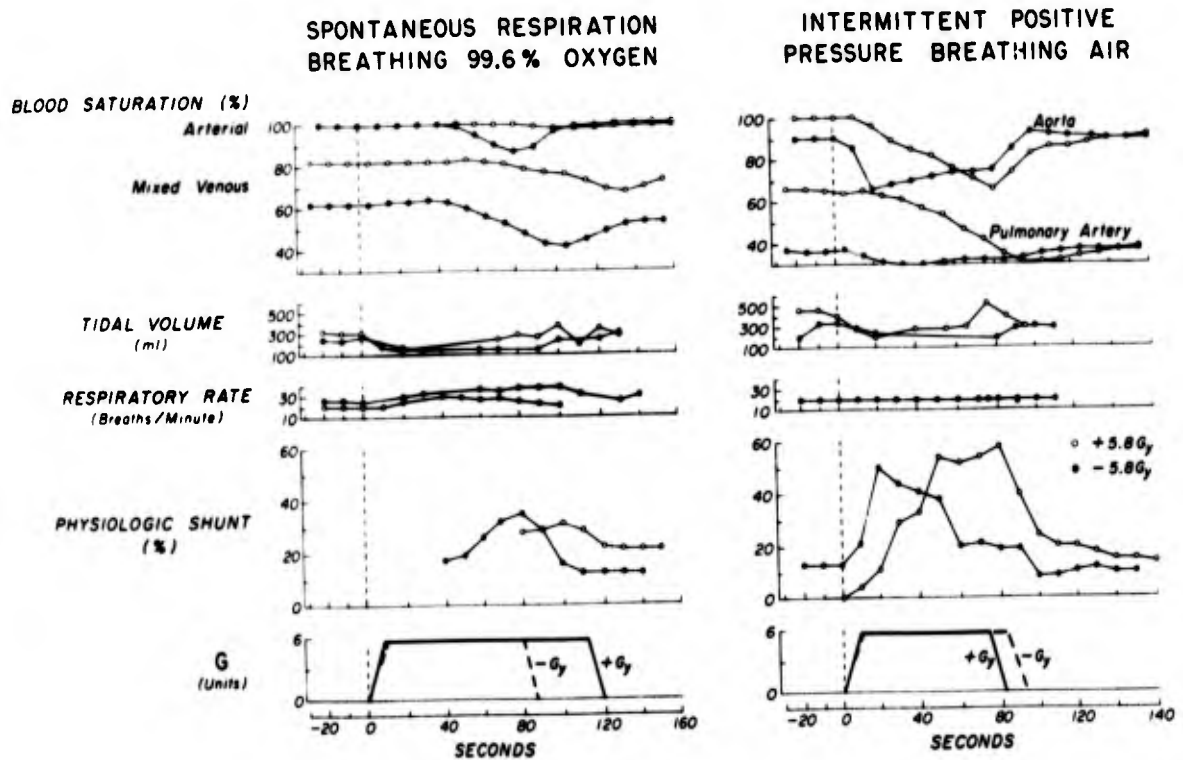


FIGURE 12

Effect of lateral acceleration on the pulmonary arterial-venous shunting in female chimpanzee F while breathing air during exposure to 2.9 and 5.8Gy.



**FIGURE 13**

Effect of lateral acceleration on the pulmonary arterial-venous shunting in female chimpanzee F while breathing oxygen and while intermittent positive-pressure breathing air during -5.8 and +5.8Gy.

(♀ Chimpanzee 39 kg, Sernylan - Pentobarbital)

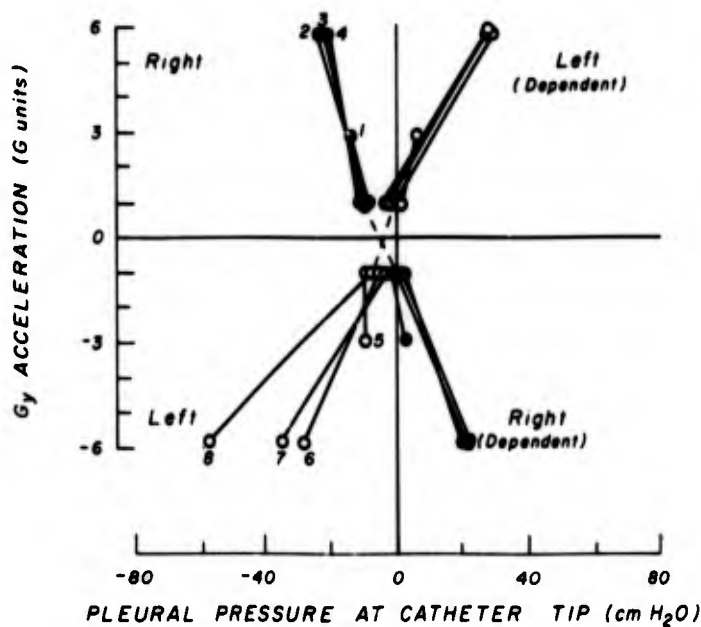


FIGURE 14

Influence of right (+G<sub>y</sub>) and left (-G<sub>y</sub>) lateral acceleration on end-expiratory intrapleural pressure at lateral borders of the lungs in female chimpanzee F.

The values for the right and left lungs were determined simultaneously. The numerals indicate the temporal sequence of the successive exposures to accelerations of 2.9 and 5.8G<sub>y</sub>.

(Average Values of 5 Chimpanzees)

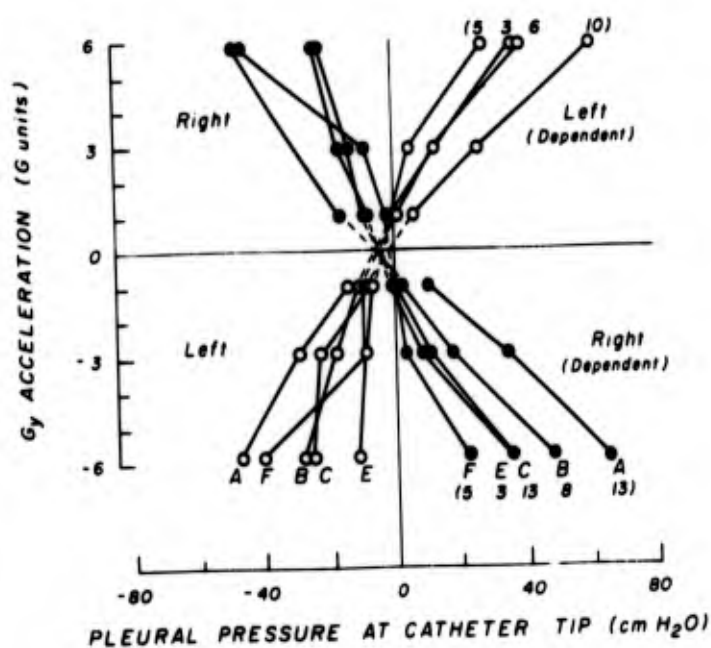


FIGURE 15

Influence of right (+G<sub>y</sub>) and left (-G<sub>y</sub>) lateral acceleration on end-expiratory intrapleural pressure at lateral borders of the lungs of five chimpanzees. The letters identify individual chimpanzees (see table I). The numerals enclosed by parentheses indicate the number of exposures to acceleration in the right and left lateral positions from which the average values were determined.

(5 Chimpanzees, Sernylan-Pentobarbital Anesthesia)

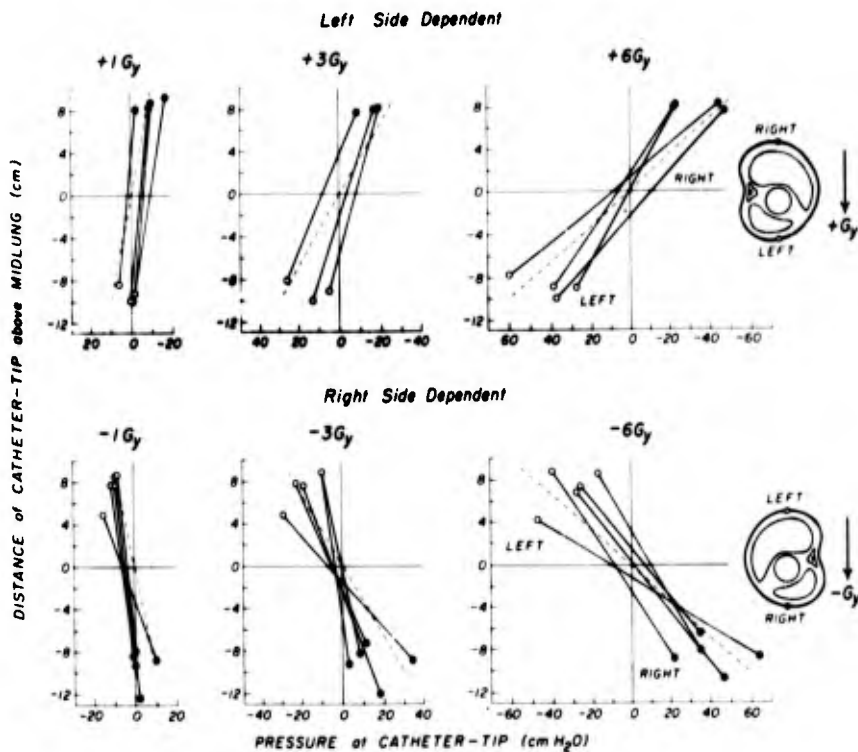
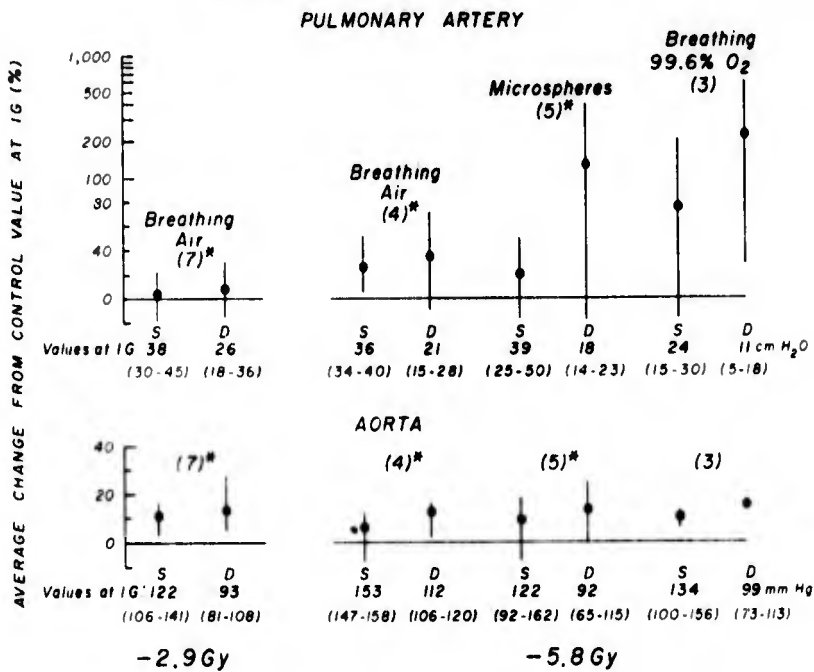


FIGURE 16

Effect of lateral acceleration on the difference between end-expiratory pleural pressures at superior and dependent surfaces of the lungs of five chimpanzees. The schematized cross sections of a chimpanzee's thorax to the right of the upper and lower panels indicate the orientation of the animal's body in relation to the resultant vector of the gravitational-inertial force environment and the position of the recording pleural catheter tips at the lateral margins of the right lung (solid circles) and left lung (open circles), respectively. In one animal (lower panel) the tip of the left pleural

catheter was apparently positioned in an interlobar fissure in the midregion of the left chest rather than at the left lateral border. The large difference in pressure between this site and the lateral border of the right lung of  $1.9 \text{ cm H}_2\text{O/G} \times \text{cm}$  is not explainable on the basis of the weight (specific gravity) of the thoracic contents. The dashed line indicates the gradient in pressure between superior and dependent sites in the pleural space which would be expected if the thoracic contents behaved like a fluid system with a specific gravity of 1.0.

(Chimpanzees, Sernylan-Pentobarbital Anesthesia)  
Average and Range of Values



**FIGURE 17**

Changes in systolic and diastolic systemic and pulmonary arterial pressures during acceleration of chimpanzees in the right lateral position. The numbers in parentheses within each plot denote the number of chimpanzees studied under each condition, as shown. The asterisk refers to intermittent positive-pressure breathing used in some of the experiments. The average and the range of values determined at 1G just prior to the exposures to acceleration are given below each plot.



(Chimpanzees, Sernylan - Pentobarbital Anesthesia)  
Average and Range of Values

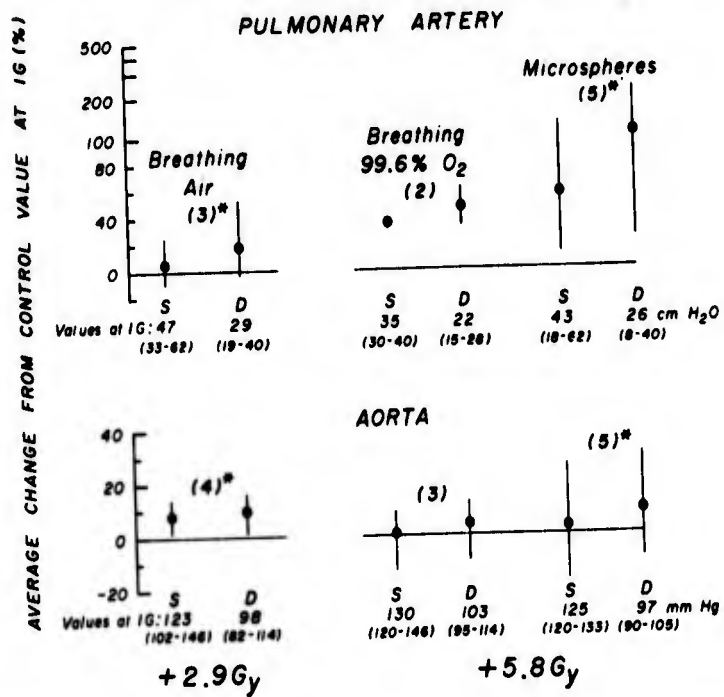


FIGURE 18

Changes in systolic and diastolic systemic and pulmonary arterial pressures during acceleration of chimpanzees in the left lateral position. See legend for figure 17 for details.

(♀ Chimpanzee 39 kg, Sernylan-Pentobarbital Anesthesia)

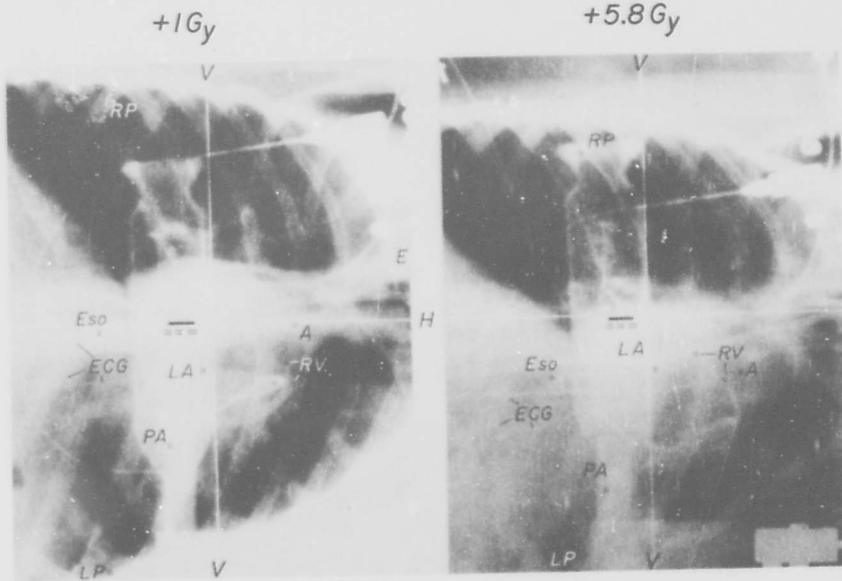


FIGURE 19

Posteroanterior roentgenograms of female chimpanzee F before and during exposure to 5.8G in the left lateral position. The solid and dashed lines near the midpoint of each roentgenogram indicate the position of the menisci in the bilateral thistle tubes used to determine the zero-reference level for all pressure recordings. V and H indicate the silhouettes of the steel wires used to mark the midpoint and the axis of rotation of the cockpit, respectively. The intersection of these wires also marks the central axis of the roentgen beam used to produce this roentgenogram. See legend for figure 1 for additional definitions of symbols.

Note caudal displacement of right (superior) dome of the diaphragm and increased radiolucency and area of the right lung, and opposite changes in left (dependent) hemithorax during exposure to +5.8Gy.

(♀ Chimpanzee 39 kg, Sernylan-Penobarbital Anesthesia)

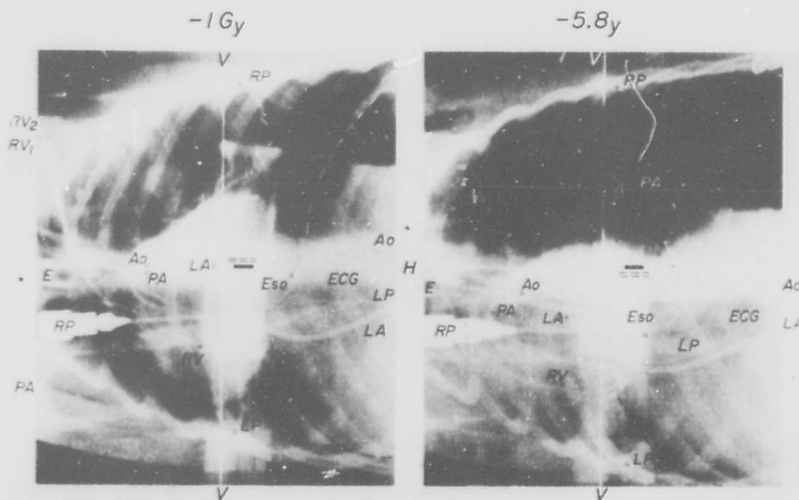


FIGURE 20

Effect of lateral acceleration (right side down) on the position of the thoracic contents and tips of the recording catheters in female chimpanzee F. The domes of the diaphragm have been indicated by dashed lines to facilitate visualization of the change in their position produced by exposure to -5.8Gy. (See legend for figure 19 for additional details.)

(♀ Chimpanzee 46 kg, Sernylan - Pentobarbital Anesthesia)

Time: 10:00pm

1:00am

3:00am

After 1.5 hours  
at +1Gy

After 1 (2.9Gy) and  
2 (5.8Gy) Exposures

15 minutes After Return  
to Supine Position

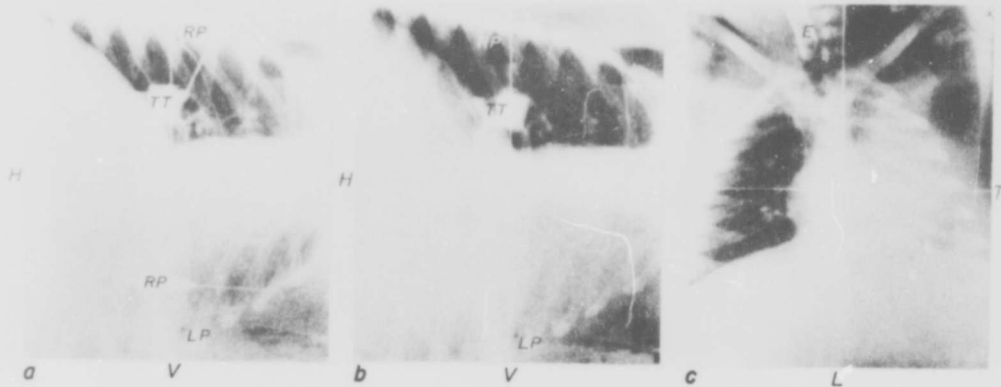


FIGURE 21

Posteroanterior roentgenograms of female chimpanzee C at 1G before and after 60-second exposures to 2.9 and 5.8 G in the left lateral (+G<sub>y</sub>) position. T and L mark the silhouettes of steel wires whose intersection falls on the central axis of the roentgen beam (see legend for figure 19 for additional definition of the symbols).

Note: (1) the increase in radiopacity of the dependent left lung after 3 hours at +1Gy and three 60-second exposures to +G<sub>y</sub> acceleration in this body position; (2) that in this animal, unlike most others, roentgen evidence of atelectasis of the left lung persisted after return to the supine position.

**DOCUMENT CONTROL DATA - R & D**

*(Security classification of title, body of abstract and indexing annotation must be entered when the overall report is classified)*

1. ORIGINATING ACTIVITY (Corporate author) Mayo Foundation 200 First Street, SW Rochester, Minnesota		2a. REPORT SECURITY CLASSIFICATION <b>Unclassified</b>	
		2b. GROUP	
3. REPORT TITLE <b>SCINTISCANNING SYSTEM FOR STUDY OF REGIONAL DISTRIBUTION OF BLOOD FLOW</b>			
4. DESCRIPTIVE NOTES (Type of report and inclusive dates) Final report January 1968 - September 1969			
5. AUTHOR(S) (First name, middle initial, last name) Earl H. Wood                      James F. Greenleaf                      Donald J. Sass Craig M. Coulam                      David Nathan William Dunnette                      Erik L. Ritman			
6. REPORT DATE February 1970		7a. TOTAL NO. OF PAGES 197	7b. NO. OF REFS 77
8a. CONTRACT OR GRANT NO. F41609-68-C-0022		8b. ORIGINATOR'S REPORT NUMBER(S) SAM-TR-70-6	
b. PROJECT NO.		9b. OTHER REPORT NO(S) (Any other numbers that may be assigned this report)	
c. Task No. 793003			
d.			
10. DISTRIBUTION STATEMENT  This document has been approved for public release and sale; its distribution is unlimited.			
11. SUPPLEMENTARY NOTES		12. SPONSORING MILITARY ACTIVITY USAF School of Aerospace Medicine Aerospace Medical Division (AFSC) Brooks Air Force Base, Texas	
13. ABSTRACT  The effect of changes in the direction and magnitude of the gravitational-inertial force environment on the regional distribution of impacted 35- $\mu$ diameter microspheres has been measured in the lungs of six anesthetized chimpanzees. These distributions were determined by two computer-controlled scintiscans at 780 sites covering the dorsal and ventral surfaces of the thorax at 1 G subsequent to four injections of differentially isotope-tagged microspheres into the right ventricular out-flow tract while at 1 and $\pm$ 5.8 Gy. Pulse-height analysis at each site allowed separation of count values for the isotopes, and, after correction for collimator distortion, these values were assumed to be proportional to the respective blood flows which were present below each site at the respective time of injections. Computer-generated 3-dimensional and contour map displays of the scintiscan and related physiologic data indicate that pulmonary blood flow tended to redistribute toward the mid-thoracic region during acceleration exposures concomitantly with large decreases in arterial oxygen saturation presumably from pulmonary shunting via the dependent regions of the lung. The decrease in blood flow to the superior regions of the lung coupled with the finding of no change or decreases in flow to the dependent regions of the lung suggests that selective increases in resistance to blood flow to the dependent, presumably anoxic, region of the lung occurred which were responsible for the reduction in level of physiologic shunt frequently found in these animals toward the end of the exposure to 5.8 Gy.			

14

KEY WORDS

LINK A

LINK B

LINK C

ROLE

WT

ROLE

WT

ROLE

WT

Bioinstrumentation  
Physiology  
Pulmonary blood flow  
‡ Gy acceleration  
Computer scanning of lungs  
Computer presentation of scan data  
Acceleration physiology